Arianna Guglielminotti

Effect on band gap of ligand-exchange in solution processed CZTS thin films, analyzed through PES study

July 2019

Master's thesis

Master's thesis

2019

Arianna Guglielminotti

NTNU
Norwegian University of
Science and Technology

NTNU
Norwegian University of
Science and Technology

NTNU
Norwegian University of Science and Technology

Effect on band gap of ligand-exchange in solution processed CZTS thin films, analyzed through PES study

Arianna Guglielminotti

Acknowledgements

As this arduous journey called "Master Thesis" is approaching to an end, I can't but look back at the hard moments I spent dealing with my own struggles and negative emotions, and be satisfied of myself and my achievements. However, I know I would not have been successful in what I believe turned out to be a success, without a long series of people that helped me along the way.

For the academic support, I have to thank my NTNU supervisor Prof. Justin Wells for his kindness and interest in my work. Thank you for being a good listener, for the motivational talks, and for all the great experiences that I lived by being part of your group. I am very grateful for the opportunity I had to spend time at the ASTRID2 synchrotron on my personal project, and I will never forget your magical additions to my thesis project.

I also want to thank my DTU supervisor Prof. Jens Wenzel Andreasen for accepting the position, and for being my reference with all the DTU bureaucracy from the other side of the North Sea.

There would be no thesis without the endless help of Dr. Rajesh Kumar Chellappan. You introduced me to the fascinating world of experimental physics by teaching me all the laboratory secrets, by providing all the support to my project, by taking me to beamtime, and by reminding me that new knowledge in science necessarily involves many failures.

To the founder of my interest in CZTS, Dr. Christian Rein, goes all my gratitude. We have been working together for almost two years, and under your guidance I met surface chemistry and possibly understood my future directions. Thank you for always been present and active in my project, and for your constant reliability.

A special thanks goes to the beam line scientist Zheshen Li. Thank you for the time spent in explaining the theory of resonance, for your support in the acquisition of the data, and for the help in understanding the results. My time in Aarhus has been a life-learning experience also because of you.

Last but definitively not least, goes the thanks to my friends and my family. To my friends in Denmark, whom I met just one year ago, but mean the world to me. Thanks for cheering me up in my loneliness, for bringing joy when we are together, and for minimizing the struggles of the thesis semester. To my boyfriend, the one and only that could stand and understand my life revelations along this past year, and whom promised with his affection to deal with my difficult state of mind for the years to come. I own you a big apology, but you will own me yours when the time for your thesis will come. And finally, thanks to my family, for a very-needed economical support, but mostly for believing in me even when I was about to stop doing it, for teaching me the values that I want to spread in the world, and for allowing me to take my time to understand what I want to be.

Abstract

In this work, Photoelectron Spectroscopy (PES) was employed to analyse elemental composition and energy band gap of Cu_2ZnSnS_4 (CZTS) stabilized nanoink deposited films, with the aim of understanding the behavior and effects of the ligand-nanoparticle (NP) interface. Samples were prepared with 1-dodecanethiol (S^{2-} anions), thiostannate complex ($Sn_2S_6^{\ 4-}$ anions) and oleylamine (C-chains) coatings. The results of X-ray photoemission (XPS) analysis were necessary in order to understand the contribution of ligands to the overall signal, and to detect possible secondary phases. XPS conclusion helped to determine the relative size of the ligands with respect to the electron mean free path, as well as the presence of Cu_3SnS_4 (CTS) phase at the outer surface of the NPs and the existence of consistent sulfoxide compounds in the deposited layer. Ultraviolet photoemission (UPS) and Inverse photoemission (IPES) provided insights to the energy band gap of the different films, showing the insulating behavior of the capping agents. All the samples underwent thermal treatment, in order to understand, by evaporation of the capping agents, the dipole-induced behavior of the presence of ligands at the NP surface. The presence of dipoles due to S^{2-} and $Sn_2S_6^{\ 4-}$ ligands is supposed to induce a shift of all NP energy states to higher binding energies. The main challenge encountered when performing PES on the drop-casted samples regarded high charging of the material, even if the substrate consisted of Si-doped wafers. Such response gave more credit to the hypothesis of the insulating effect of the ligands. A high-crystallinity CZTS sample was provided by the DTU Fotonik department, and used as benchmark for the analysis of the valence band (VB) of the material, as well as for the peak energies of CZTS core levels. Resonance photoemission (RPES) was performed over the crystalline sample at the beamline MATline at ASTRID2 synchrotron in Aarhus University. Results of the RPES analysis provided supporting information about the elemental contribution to the VB of the material: the energy states closer to the VB maximum seemed to be associated to Cu and S, as resonance was observed at photon energies crossing the Cu 3p and S 2p absorption edges.

Contents

1   Introduction

As the current global energy demand increases to the terawatt magnitude, renewable energy sources acquire more and more importance in order to limit the environmental impact of energy production. In this panorama, solar cells become one of the most attractive renewable energy technologies. As a matter of fact the amount of energy arriving on Earth from the sun is gigantic ($\approx 10\,000$ times the current energy consumption of the human species), and converting it efficiently is necessary both to fulfill the energy demand and to mitigate the production of CO_2 and the increasing temperature in the atmosphere [1].

Shockley and Queisser published a paper in 1961 [2], in which they introduce the now famous Shockley-Queisser limit curve showed in Figure 1 by the black line. They theorized the maximum theoretical power conversion efficiency of a single junction solar cell as a function of its bandgap, assuming AM 1.5 solar spectrum and unconcentrated sunlight. Figure 1 shows different solar cells technologies in their record efficiencies at February 2018.
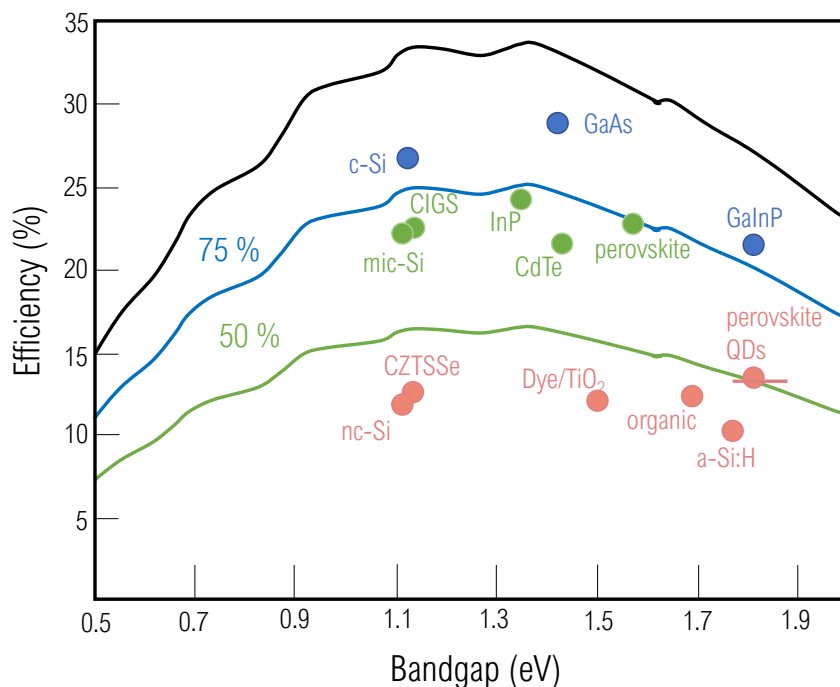
Figure 1: Theoretical Shockley-Queisser power conversion efficiency limit as a function of bandgap (black line). The blue line and the green line represent the 75 % and 50 % of the theoretical limit. The record efficiencies for different materials are plotted for the corresponding band gaps, revised February 2018. The colors of the dots, representing the different technologies, depend on the difference of their record efficiency to the theoretical maximum: blue - above 75 % of the S-Q limit, green - between 50 % and 75 %, red - below 50 %. Adapted from reference 3.

Although silicon based solar cells still make up for the majority of the market, thin film solar cells are under development as their characteristics demonstrate the potential to reduce production costs for both materials and fabrication processes, and improved efficiency. This class of photovoltaics can be formed by stacks of thin coatings made of different materials, on top of a substrate. The absorber layer can then be chosen from a series of materials that, compared to silicon, absorb light more strongly being *direct bandgap semiconductors* [4]. Technologies based on compounds such as CdTe and $CuIn_xGa_{1-x}Se_2$ (CIGS) have shown promising efficiency (22.1 % and 22.6 % respective record efficiency on the laboratory scale [4]), but the toxicity of Cd and scarcity of In, Ga and Te become important obstacles to mass production [5] [6]. Other thin film technologies that have seen an exponential interest are perovskites, but they show major issues regarding their stability. Kesterite photovoltaics utilizing Cu_2ZnSnS_4 (CZTS), $Cu_2ZnSnSe_4$ (CZTSe) and $Cu_2ZnSn(S,Se)_4$ (CZTSSe) have emerged as a promising alternative to CIGS, through the introduction of nontoxic and earth abundant elemental composition and their suitable optical properties for solar energy harvesting. The presence of Se should be taken in consideration (as it is fairly scarce) when projecting this technology to mass production, as well as the use of Cd in the n-type layer of the solar cell, generally composed of CdS. Non-toxic oxide buffer layers (Zn,Sn)O have been already substituted to CdS and showed improved efficiency due to the enhanced band alignment [7]. The record laboratory efficiency achieved for CZTS solar cells is 9.1% and for CZTSSe 12.6% [4].

Among all the techniques for deposition of CZTS, solution-processed deposition methods have high potential in reducing fabrication costs by high-throughput roll-to-roll manufacturing [8]. A major advantage of this technique is that different synthetic routes allow tunable composition of the nanoparticles (NPs) prior to the deposition step. CZTS nanocrystals (NCs)-based inks and molecular inks have been successfully utilized to fabricate solar cells with >8% efficiency, achieved however after annealing the films at high temperatures under a sulphur atmosphere [8]. To avoid the annealing step, surface ligand chemistry plays a vital role as deposition of NCs thin films with well-passivated surfaces is critical for an efficient extraction of photogenerated charge carriers. All nanomaterials are characterized by a large surface-to-volume ratio that makes their surfaces the dominant player in many physical and chemical processes. Surface ligands - molecules that bind to the surface - are an essential component to material synthesis, processing and application, as they form a "capping" layer that saturates dangling bonds, screens the particle from its environment, and controls nucleation and growth kinetics during synthesis [9]. Ligands can influence also the optical and electrical properties of the NCs. In recent years, effort has been put in exchanging long insulating native ligands with shorter organic and inorganic ligands to decrease the distance between NCs and effectively passivate the surface.

The interest of this thesis experiment lies in understanding the effects of different ligands on the band gap of the CZTS NPs thin film. Multiple samples were prepared and provided by

Christian Rein, Postdoctoral Researcher at DTU Energy, and analyzed through Photoemission Spectroscopy (PES) techniques. The samples differed in the ligands, while the NPs, later undergoing ligand-exchange operations, belonged to the same batch. All the samples were characterized by X-ray Photoemission (XPS) to measure elemental composition, and combined Ultraviolet Photoemission (UPS) and Inverse Photoemission (IPES) to calculated the band gap of the deposited material. The samples underwent thermal treatment of 200 °C for one hour, and the changes of behavior in the spectra before and after the treatment were addressed to the partial loss of ligands on the surface. Moreover, this thesis work contains also some further analysis on the structure of the valence band of CZTS, performed through Resonance Photoemission (RPES) at the Aarhus MatLine beamline on an highly crystalline sample, provided by the DTU Fotonik deparment. Results of this experiment increased knowledge about the elemental contribution to the valence band of the material, and provided a reference for the NPs results.

This thesis report is articulated in other six chapters. The first part of the report aims at providing the reader with background information on kesterite solar cells (Chapter 2), as well as basic theory on surface science and interface behavior of NPs (Chapter 3) and physics principles of PES techniques (Chapter 4). In the second part, experiment details on samples and facilities adopted will be presented (Chapter 5), and the results introduced and discussed (Chapter 6). A summary of the key discoveries and future outlook can be found in the conclusive Chapter 7.

2 Kesterite Solar Cell

From a crystallographic point of view, CZTS can be obtained by the zincblende structure of ZnS, by keeping the S anion in its positions and replacing Zn cations with Cu and Sn maintaining charge neutrality. The material belongs to the compound $A_2^{I}B^{II}C^{IV}X_4^{VI}$ family (considering A = Cu, B = Zn, C = Sn, X = S) [10]. The atoms in the structure are arranged in two possible existing phases, with similar formation energy: kesterite and stannite. Both the structures have a *ccp* array of anions with cations occupying one half of the tetrahedral voids [10]. However, the kesterite structure, represented in Figure 2, has been found to be the most favourable [4] [10]. The kesterite structure is characterized by a cell that is pseudocubic (2a = c). The Cu atoms are in the separate positions 2a (0,0,0) and 2c (0,1/2,1/4). The Zn, Sn and S atoms are in positions 2d (1/2,0,1/4),2b (1/2,1/2,0) and and 8g (0.7560, 0.7566, 0.8722). More details on the crystal structure of kesterite and stannite can be found in reference 11.
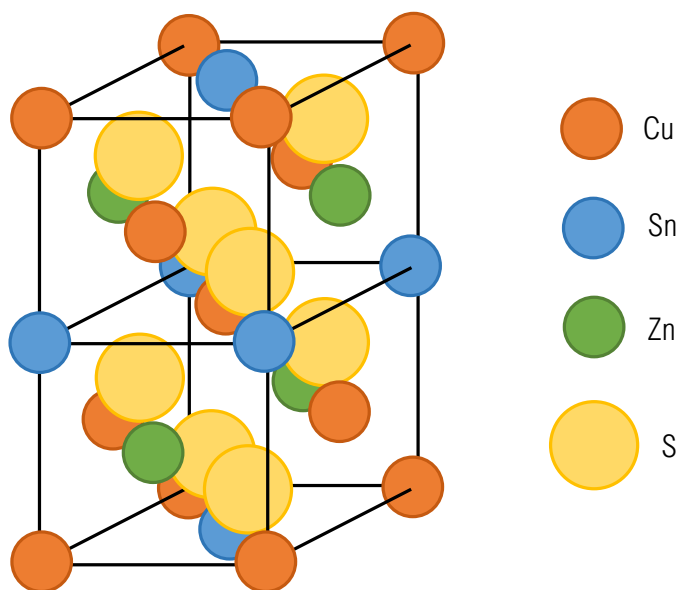
Figure 2: Unit cell of the kesterite type structure. Kesterite crystallizes in a pseudocubic structure (2a = c). The big yellow sphere represent S anions, while the smaller are the cations (Cu-orange, Zn-green, Sn-blue). Adapted from reference 11.

Even if the stoichiometric ratio of Cu, Zn, Sn and S elements is 2:1:1:4, most of the samples synthesized are non-stoichiometric. Research has been done in order to visualize the distribution of solar cell efficiencies depending on the Cu/(Zn + Sn) and Zn/Sn ratios. It was possible to notice that all the cells with efficiency higher than 8% had Cu/(Zn+Sn) and Zn/Sn ratios around 0.8 and 1.25 respectively [12]. For this reason, an empirical rule for the synthesis of CZTS is that the material needs to be Cu-poor and Zn-rich. Two main causes are addressed

for the non-stoichiometry of CZTS, meaning the easy coexistence of secondary phases and the high concentration of point defects and defect clusters. Their effect on band gap and efficiency will be further exploited in the Chapter 2.2. It is however of high importance to realize that due to the presence of mostly acceptor defects, this material is intrinsically p-type.

The band gap of real CZTS material has been measured to be 1.4-1.6 eV depending on the disorder in the structure. However, the theoretical analysis sees the band gap at 1.5 eV [4]. It has been shown through "first-principles" modelling that the valence band (VB) of CZTS consists primarily of antibonding states of hybridized Cu 3d and S 3p orbitals, whereas the conduction band (CB) consists of the antibonding states of hybridized Sn 5s and S 3p orbitals [13]. The Shockley-Queisser limit defines which is the maximum theoretical efficiency achievable for a single-junction solar cell with absorber material of a certain band gap, considering temperature of the cell and the illuminating spectrum. For a standard AM 1.5 solar spectrum, a semiconductor with band gap of 1.1-1.5 eV has a maximum theoretical efficiency of 32-35%. In theory, CZTS is a perfect candidate to be an absorber material for a solar cell. The highest efficiency so far reached for a thin-film CZTS(e) family solar cell is 12.6% by IBM using toxic hydrazine solution, with low S content S/(S+Se) $\approx$ 0.3 and bandgap of 1.13 eV [4] [14].

2.1   Device design and working principles

The development of CZTS solar cells started in Japan: until 2008 only a few research groups in the country and one in Stuttgart were investing effort in understanding the potentiality of this material [15]. Katagiri proposet to recreate the typical CIGS device architecture for CZTS solar cells. Figure 3 shows the CIGS structure after the absorber layer is substituted by CZTS. The solar cell is a p-n planar heterojunction: the "heterointerface" occurs at the interface between CZTS and CdS layers. Light carrying more than 1.5 eV is absorbed by the p-n junction, as the energy gap E_g of CZTS corresponds to this value. However, CdS has higher E_g, $\approx$ 2.4 eV, therefore photons carrying energy between 1.5 eV and 2.4 eV can be absorbed only by CZTS. Also ZnO and ZnO:Al contribute to the production of photoelectrons: the generation of carriers in these materials occurs at photon energies higher than 3.3 eV, value corresponding to their E_g [16].

The three n-type layers serve several purposes. The CdS layer forms an high crystallographic quality heterojunction with the absorber, facilitating carrier collection [16]. Moreover, it acts as diffusion barrier layer for Al, or any other element used as dopant in ZnO, and as a sputter damage protection (the standard technique used to deposit ZnO). The transparent conductive oxide (TCO) layer is typically formed by a thin layer of intrinsic ZnO followed by a thicker layer of Indium Tin Oxide (ITO) or Al-doped ZnO. The former is generally needed as shunt protection together with CdS, and for growth initiation of ZnO:Al. This last layer is the highly doped n-type material that allows the p-n junction formation and the carrier transport to the metal grid.
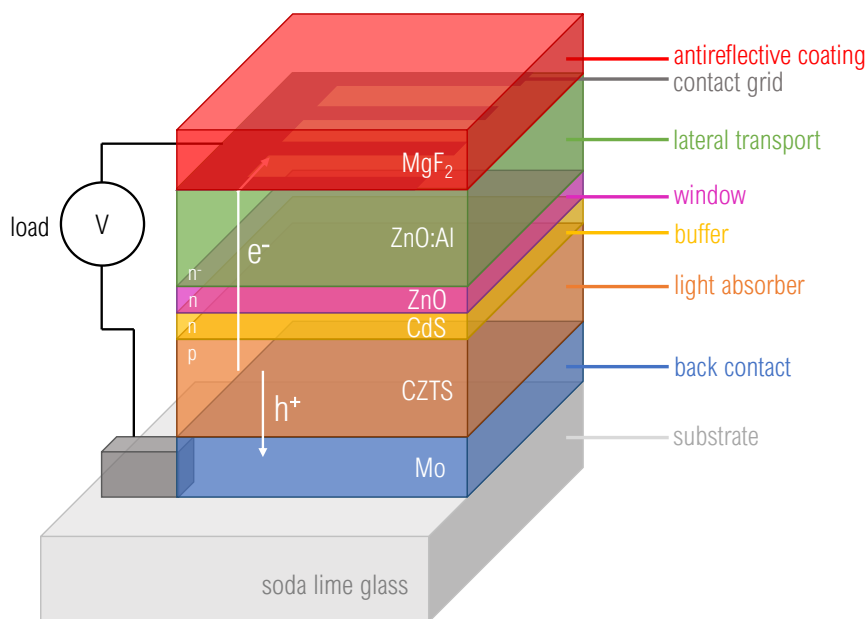
Figure 3: Structure of a tipical CZTS solar cell. The symbols e$^-$ and h$^+$ show the photogeneration of the electron-hole pair and their separation/transport to the respective metal contacts. The symbols n and p show the doping of the layers.

MgF$_2$ is typically deposited on high-performing devices as an anti-reflection coating [16]. When CZTS is annealed on top of Mo substrate, MoS$_2$ forms and gaseous S with high partial pressure must always be supplied during the annealing process to ensure that CZTS does not decompose.

Electrons and holes need to be collected at two separate contacts in the solar cells for a net current to flow into the external load. This process must initially work under short circuit conditions. The driving force behind charge separation and transport towards the respective contacts can be found in the electrochemical potential gradients of holes and electrons, i.e. in their quasi-Fermi levels. A quasi-Fermi level is a term used to describe the Fermi level in the case of electron and hole populations displaced from equilibrium. Such displacement can be caused by the application of an external voltage or by exposure to light, which alters the populations of electrons in the conduction band and valence band. For the electron-hole pairs generated within the depletion region of the p-n heterojunction (see Figure 4), separation is ensured by the built-in electrostatic potential gradient formed across the p-n junction when the junction is formed. The width of the depletion region depends in general on the thickness as well as the doping density and relative permittivity of CZTS, CdS, and ZnO. In state-of-the-art CZTS solar cells, the depletion region extends about 180-200 nm from the p-n junction into CZTS [4]. The short circuit current J_{sc} defines how well the solar cell is working under the

condition of no external load. To produce work and so electrical power, the photogenerated current must flow against an applied voltage that acts as a reducing agent over the built-in potential of the cell. As forward bias increases, the point when current is consumed instead of generated can be reached. This turning value of external load is called open circuit voltage V_{oc}. In general, the photogenerated current can be considered as the difference between the short circuit value and the diode current, or recombination current. Moreover, parasetic resistance causes further losses.
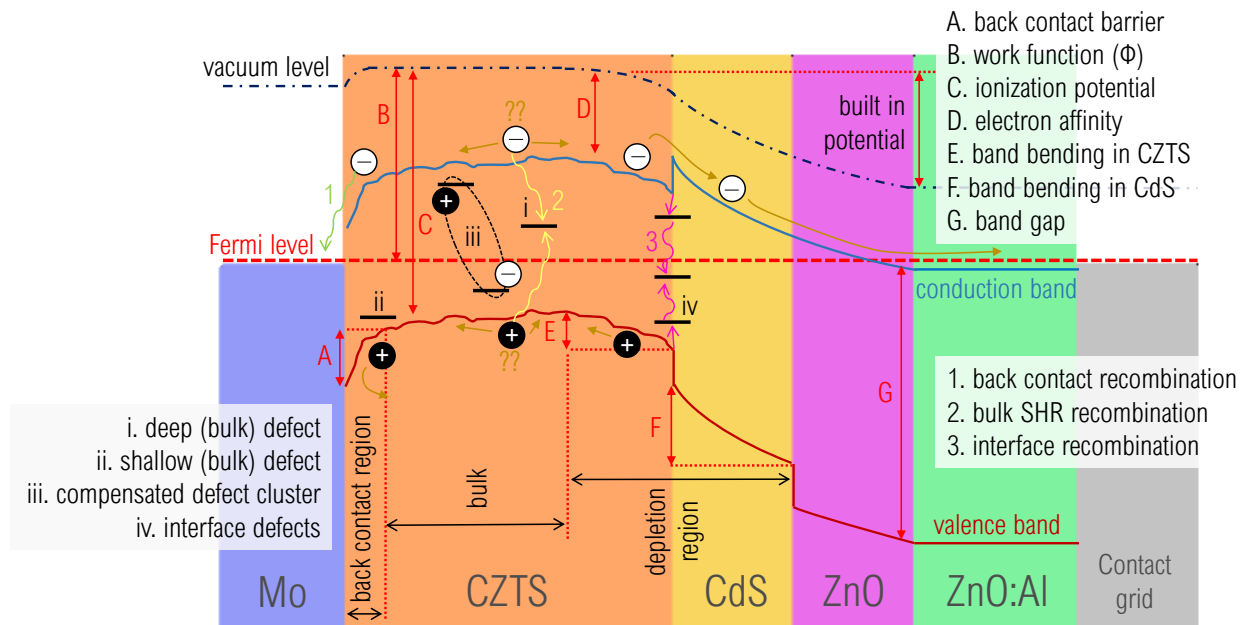
Figure 4: Illustrative representation of a band diagram of a CZTS solar cell. On the x-axis, the architecture of the cell is developed, while the y-axis represents energy. The different legends report defects, recombination mechanisms and definitions name of energy differences [4].

2.2   Non-idealities in the material

As already stated, the highest recorded efficiencies for CZTS solar cells were measured in non-stoichiometric ratios. It was shown that CZTS could exist as a non-stoichiometric phase when the overall stoichiometry (i.e., CZTS plus any other phases) was characterized by Cu/(Zn+Sn) = 0.79 and Zn/Sn = 1.19, which meant a 6% absolute deviation in Zn and Cu content from the stoichiometric point. However, non-stoichiometry results always in ZnS segregation. ZnS is the least harmful secondary phase, as it has large band gap. Lower band gap phases, such as Cu_xS, SnS, Cu_2SnS_3, are much more dangerous for the V_{oc} as they can trap free carriers due

to the potential well they form with the VB or CB of CZTS.

Point defects and defect clusters are other non-idealities that can have important effects on the performance of CZTS solar cells. Shallow defects are defined to be the ones lying within 0.2 eV from the VB or CB edges. The closer in energy the defect lies with respect to band edges, and the larger it's its volume density, the more free carriers it adds to the specific band and the more it tends to move the Fermi level and dope CZTS p-type or n-type. Therefore, shallow defect determine the doping density in CZTS, CdS, ZnO, ZnO:Al, and cause structural disorder in the kesterite structure of CTZS. Deep defects lie closer to the middle of the band gap and can cause Shockley-Read-Hall recombination in the CZTS bulk. These two types of defects may be isolated or form clusters consisting of a combination of acceptors and donors with net zero charge. Generally, isolated defects produce the effects previously described, while clusters can locally change the band edge positions in the material, modifying its properties [12]. Figure 4 shows also the energy position of the defects in the band gap of CZTS. The intrisic p-type behavior of stoichiometric and non-stoichiometric CZTS is given by the point defects Cu_{Zn} and V_{Cu} respectively. The first has ionization level deeper than the vacancy but in stoichiometric samples it is present with higher density, producing high hole population and obstruct n-type doping. Under Cu-poor Zn-rich kesterites, V_{Cu} becomes the dominant point defect and contributes to the p-type conductivity [12].

Grain boundaries (GBs) in kesterite absorbers exhibit benign electronic properties in Cu-poor and Zn-rich CZTS and CZTSSe solar cells [6]: GBs seem to act as electron flow channels rather than dominant recombination centers, due to higher positive surface potentials at the GBs compared to the bulk of the grains, and charge separation is then enhanced. This effect might result from the thermodinamically favourable formation of the $[V_{Cu}+Zn_{Cu}]$ defect clusters in Cu-poor Zn-rich conditions, that decreases both the valence and conduction band edge energies relative to the kesterite bulk. This could lead to the potential barrier that repels holes from GBs and attracts electrons [17].

2.3   Production Methods

This section is based on reference [18], which offers a good overview of thin film deposition methods, and their relevance to solar cell applications.

The first thin films of CZTS were prepared by Ito and Nakazawa in 1988 by an *atom beam sputtering method*. Sputter deposition involves ejecting material from a "target" that is a source onto a "substrate": sputtered atoms ejected from the target can ballistically fly from the target in straight lines and impact energetically on the substrates. *Spray pyrolysis* is potentially a low-cost method suitable for large areas in which precursor solutions are sprayed at a heated substrate, with following solvent evaporation. Various metallorganic compounds or metal salts

dissolved in aqueous or organic solvents can be used as precursor solution in spray pyrolysis process. Generally, thin film deposited by pyrolysis method have shown contamination by impurities such as Cu_xS, ZnS, $CuSnS_3$. *Electron beam evaporation* method is a vacuum deposition process. An electron beam, produced by heating a tungsten filament in the electron gun, is directed toward a target material. The kinetic energy of the electrons is then transferred to the material in the form of thermal energy that makes the target to evaporate. The e-beam deposition method is really efficient for the control of stoichiometry in alloy films and its usage has been investigated for the growth of CZTS with following sulphurization. *Photo-chemical deposition* has been employed to produce CZTS thin films. With this technique, the substrate is exposed to one or more volatile precursors, which react thanks to illumination on the substrate surface to produce the desired deposit. Sulfides of Cu, Zn and Sn were formed only in the regions irradiated with deep UV light. Examples of film deposition by pulsed laser deposition and sputtering methods have also been attempted and recalled in the review. *Chemical vapour deposition* (CVD) is a well-known method for the deposition of high quality thin films for various applications (bio-medical applications, electronic materials for lasers, displays, sensors, batteries and solar cells), but its application for the deposition of CZTS has been reported only recently, probably due to the difficulties in finding the suitable precursor for the deposition of this complicated ternary system.

Non-vacuum techniques should be preferred to large scale vacuum techniques for their potential lower production cost. However, the cost of the process depends on many factors, as yield, efficiency, energy consumption, raw material cost, environmental friendliness and safety. *Electrochemical deposition* has certain advantages in terms of low-cost, and its potential for large area deposition has already been proven for deposition of CIGS and CdTe absorber layers. CZTS films were made from metallic layers, Cu, Zn and Sn, electrochemically deposited using a conventional 3-electrode cell with a platinum counter electrode and Ag/AgCl reference electrode, then annealed in sulfur atmosphere to form CZTS films at 550 °C. Other methods include *sol-gel* and *soft-solution* methods. In the latter, a substrate is covered with a solution of precursor of dispersed nanoparticles, and the film is obtained after subsequent thermal or chemical treatment. Generally, solution methods include spray coating, spin coating, and drop-casting. For the sake of this project, solution methods will be used to produce the analyzed samples. Further details on the interaction between nanoparticles and the solution environment will be given in the next chapter.

3 Surface Science of Nanoparticles

The surface of a bulk solid is characterized by a small percentage of atoms compared to the much larger amount of atoms present in the bulk volume. For this reason, the broken chemical bonds present at the interface with the exterior contribute to a minimal extent to material properties. However, the surface-to-volume ratio scales inversely with linear dimension. This results in the role of surface becoming more dominant as size shrinks. At nanoscale, surfaces can significantly alter properties and generate completely new effects. Applying traditional surface science to nanoscale can give basic understanding of the matter, although the small size complicates the picture. Thanks to surface science it is known that large crystals can lower their energy by moving surface atoms away from lattice sites (process known as surface reconstruction), dangling bonds introduce new electronic states, and foreign molecules (surfactants or adsorbates) can alter the energy and reactivity of a crystal surface. There are also some useful analogies that help in the study of nanoparticles (NPs) properties. For example, the chemical bond between NP surface atom and surfactant molecule resembles the behavior of metal ion and ligand in coordination complexes. Ligands around NPs form a "capping" layer that can be rationally designed to tune the properties of functional nanomaterials. Surface ligands saturate dangling bonds, screen the particle from its environment and control synthesis kinetics. Ligands also influence optical and electronic properties of NPs, and provide steric or electrostatic stabilization required for synthesis, processing and specific applications. Ligand exchange introduces the possibility of extending the versatility of NP materials, as it allows the replacement of synthesis optimized ligands with application-targeted species. Such applications can include sensors, LEDs, lasers, biomedical research and solar cells [9].

3.1 Colloidal nanocrystal synthesis

Colloidal nanocrystals (NCs) have an inorganic core that is stabilized by a layer of surface surfactants. From the point of view of the synthesis, colloidal inorganic NCs exhibit preparation strategies similar in many ways to those employed for artificial organic polymers. For synthetic polymers, preparative methods at disposal allow to define the mean number of monomer units in a polymer and the variance of this number, and to build complex topologies joining or branching of simpler macromolecules. A wide number of methods have been proposed to tailor the synthesis of NCs with well defined structures, like coprecipitation in aqueous phase, hydrothermal/solvothermal synthesis and surfactant-controlled growth in a hot organic solvent [19]. Reference 18 provides an overview on different synthetic routes used for the production of CZTS NPs.

A synthesis system for colloidal NCs consists of three components: precursors, organic surfactants and solvents. The process starts with heating to a sufficiently high temperature the reaction medium, so that precursors chemically transform into active species (monomers). The

monomers form the NCs initial "seed" in a process called nucleation: the precursors react to form a supersaturation of monomers followed by a burst of NCs nuclei. Their following growth happens by incorporation of additional monomers still present in the reaction medium. Choosing an appropriate temperature for the synthesis is decisive in determining the optimal conditions for NC growth: the temperature has to be hot enough to allow rearrangment of atoms and annealing within a growing NC over the course of synthesis. However, the nano-scale brings some benefits due to scaling laws of properties of solids in the nanometre regime: small crystals need a lower melting temperature, since the liquid phase has lower surface energy than a solid with facets, edges and corners. The effects can be significant, reducing the melting temperature up to half for a NC of 2-3 nm in diameter with respect to the corresponding bulk solid [19].

Growth is greatly affected by the presence of surfactant molecules in the reaction medium. It has been seen that a large reduction in melting temperature increases in the range of inorganic NCs that can be grown at temperatures where common organic molecules are stable, which is around 200-400 °C. Organic surfactant molecules in the growing medium are chosen for their propensity to adhere to a growing crystal. The energy with which the surfactant molecule adhere to the surface of a growing NC is an extremely important parameter influencing crystal growth. The adhesion energy needs to be such that it allows dynamic solvation at the growth temperature: the surfactant needs to be able to exchange on and off the growing crystal so that regions of the NC surface are transiently accessible for growth, yet entire crystals are on average monolayer-proteted to block aggregation [19].

Another feature of modern synthesis methods is the ability to produce NCs with a relatively narrow size distribution. To better understand the concepts involved here, it is important to introduce the dependence of the growth rate on the NC radius (Figure 5). Very small crystals are unstable owing to their large fraction of surface atoms: this is explained by the dependence of surface energy on size, and the growth rate appears to be negative. Larger crystals are stable and grow. The zero-crossing point occurs at the critical size, where crystal do not grow nor shrink. This point depends on the monomer concentration, with larger critical size favoured by low monomer concentration. The peak in growth rate arises because increasing the radius of large crystals requires the incorporation of many more atoms than does increasing the radius of smaller crystals. These considerations explain why a slow growth rate produces equilibrated and nearly round crystals but also very broad size distributions, due to the concomitant shrinking of small crystals while large ones grow. There is a way to recover a narrow size distribution also in case of low monomer concentration. This approach is called "size-distribution focusing", and it is based on the fact that small crystals grow more rapidly than larger ones if monomers concentrations are sufficiently high. If, considering a case of slow growth as previously described, the monomer concentration is abruptly increased by a secondary injection of precursor, the critical size will shift to a smaller value, as it depends only on the concentration. If this shift

is large enough, all the NC nuclei will have size larger than the critical size. Therefore, the distribution will spontaneously narrow, or "focus" [19].
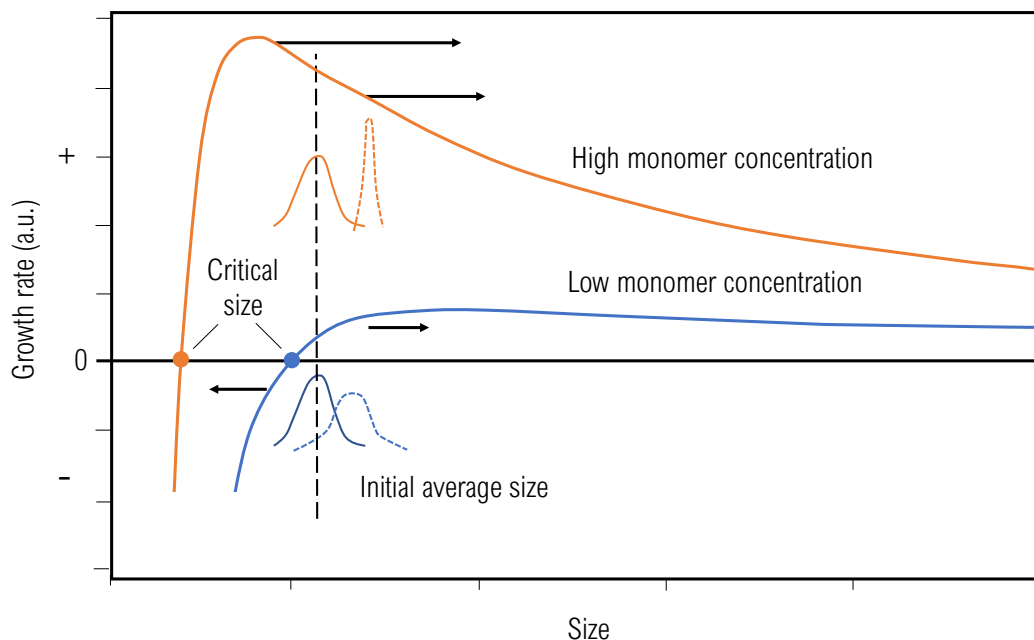

Figure 5: Schematic representation of the dependency of growth rate on size of the nanocrystals. A critical size exists at any given monomer concentration. When the concentration is high, the critical size is small so that all the particles grow. In such a case, smaller particles grow faster than larger ones and the size distribution appears nearly monodispersed. If the monomer concentration is lower, small nanocrystals are depleted as larger ones grow and the size distribution broadens. Figure based on reference 19.

3.2   Structure of the NP-ligand interface

In general, synthesis of CZTS NPs is most commonly carried out in the organic, non-polar solvent oleylamine (OLA). Similar solvents bear long-chain carbon ligands as stabilizers, and are therefore hydrophobic. The NPs ink is then prepared with organic solvents, that are generally expensive and toxic. Moreover, when CZTS films are produced the stabilizers are left behind as hydrocarbon impurities, acting as an insulating barrier that negatively affects the efficiency [20]. Solutions to such problem could be found in multiple approaches such as increase NP size (minimizing surface/volume ratio) or synthesizing through solution-based methods as hot-injection and solvothermal CZTS NPs ligand-free so that they can be dispersed in environmentally friendly polar solvents. In recent years has become of higher interest the study of ligand exchange to efficiently passivate the surface and to result in surface-binding species better suited to the end application of the NPs [8]. Ligand exchange reactions extend the versatility of NC materials by allowing replacement of ligands optimized for synthesis with

application-targeted species including organic or inorganic ions, clusters and polymers.

3.2.1   Bonding at the NP-ligand interface

The NPs are typically synthesized in a solution containing surface ligands with an anchoring headgroup tethered to the NP surface and a hydrocarbon tail directed away from it (Figure 6 (a)). The shape that the inorganic core assumes tries to minimize the surface energy and facet-specific energy of broken bonds, and typically NPs display a polyhedral core [9]. For example, Au and PbS NCs ofen adopt a cuboctahedral shape terminated by (111) and (100) planes (Figure 6 (b)). The capping layer around the NP gathers as a self-assembled monolayer. The interaction between organic/inorganic interfaces in NPs can be understood by considering extended Au (111) and (100) surfaces, covered by *n*-alkanethiolate pattern (Figure 6 (c)): between sulfur and gold atoms a strong interaction ($\backsim$ 2 eV) drives the free surfactants molecule to bind to the metal surface, while a weaker van der Waals interaction between hydrocarbon tails ($\backsim$ 0.07 eV per CH_2 group) induces dense packing in the organic overlayer. For flat surfaces, surfactants molecules arrange in a crystalline order over the underlying substrate, with sulfur typically occupying the three-fold sites and alkyl tails tilted of 30° from the surface normal. NC surfaces however don't behave like extended surfaces, and their vertex and edge sites provide extra volume for the carbon chains. This results in a higher capping-layer coverage, due to the relaxing competition for space between alkyl tails. Moreover, open space in the NC capping layer allows penetration of solvent molecules or ligand chains of neighbouring NCs.

3.2.2   Colloidal stabilization

Some functionalities of the surface ligands have been already expressed in Chapter 3.1. In addition, surface ligands allow control over the aggregation of nanocrystals: when exposed to a good solvent for a given type of surface ligand, NCs disperse in solution. There are two different mechanism of colloidal stabilization, steric and electrostatic, that provide complementary approaches to the stabilization of NC dispersions in polar or non-polar solvents (Figure 7 (a)).

Sterically stabilized NPs are, for example, NPs coated with a layer of hydrocarbon chains. A good solvent implies a negative free energy of chain-solvent mixing, so that hydrocarbon chains repel one another without overlapping the ligand coronas and stabilizing the dispersion. Typical good solvents for hydrocarbon-capped NPs are nonpolar liquids (hexane, toluene, chloroform), while non-solvents are polar (ethanol, acetone, acetonitrile). Colloidal NPs can also be stabilized electrostatically through absorption of charged species to their surface: the NP surface charge is balanced by oppositely charged ions located in a diffuse region around the particle. Good solvents for electrostatically stabilized NPs are generally polar solvents with high dielectric constant ϵ (for example formamide, $\epsilon \approx 110$). Figure 7 (b) shows the dependence of the interaction potential U on the interparticle distance r for good and non-solvent: in general, U
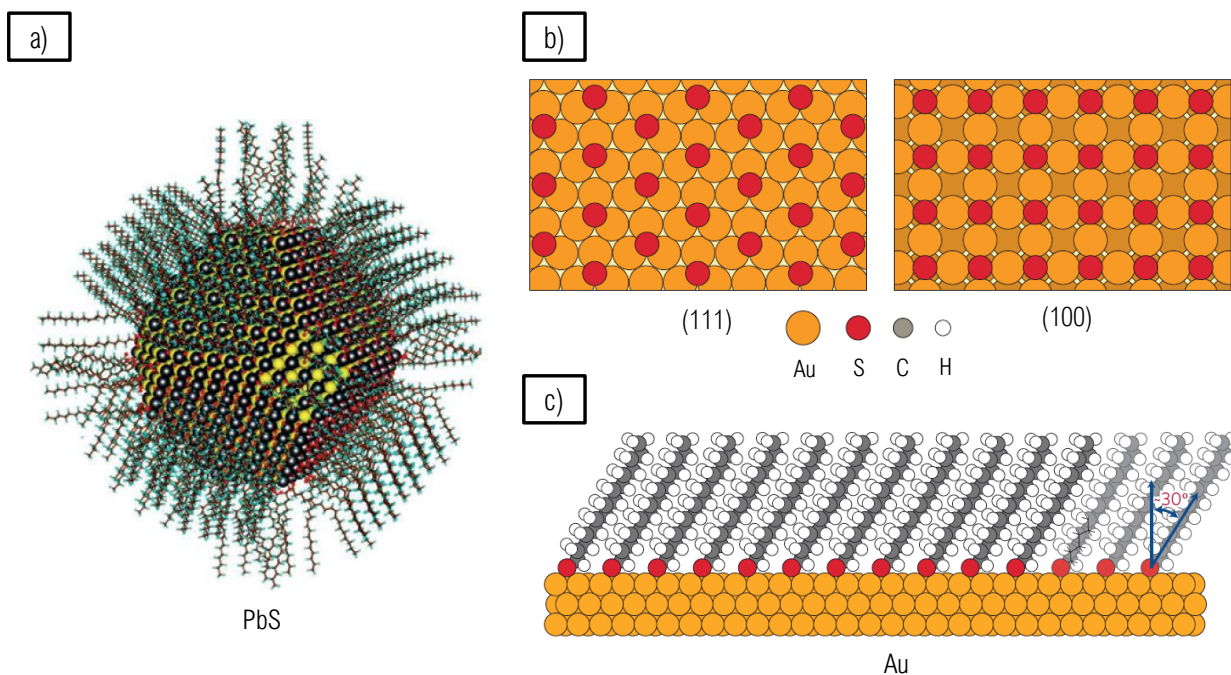
Figure 6: (a) Calculated atomic structure of a PbS 5-nm NC capped in oleic acid; (b) Binding pattern of sulfur headgroups on Au (111) and (100) surfaces; (c) Illustration of the capping monolayer of hexadecanethiol molecules adsorbed to Au(111) surface: hydrocarbon chains are fully extended and tilted with respect to the surface normal. Adapted from reference 9.

is purely repulsive for NPs in a good solvent, whereas in a non-solvent attractive interaction becomes dominand at an intermediate distance of neighbouring NPs.

3.2.3   Metal-ligand interactions

The interaction between NP core and ligand headgroup can be explained using the classification of covalent bonds. Such classification has been adapted to NCs from metal coordination complexes [21]. Three classes of interaction metal-ligands can be defined depending on two paramenters: number of electrons involved, and the identity of donor and acceptor groups. A classification of ligand binding motifs is showd in the case of CdSe NPs in Figure 8. L-type ligands are neutral 2-electron donors with a lone electron pair that datively coordinates surface metal atoms. Examples are found in amines (RNH_2), phosphines (R_3P) and phospine oxides (R_3PO). X-type ligands can be neutral radicals binding neutral surface sites (each with an unpaired electron), or more commonly monovalent ions binding oppositely charged sites at the NC surface. The last typology are the Z-type ligands: these ligands act as two-electron acceptors.
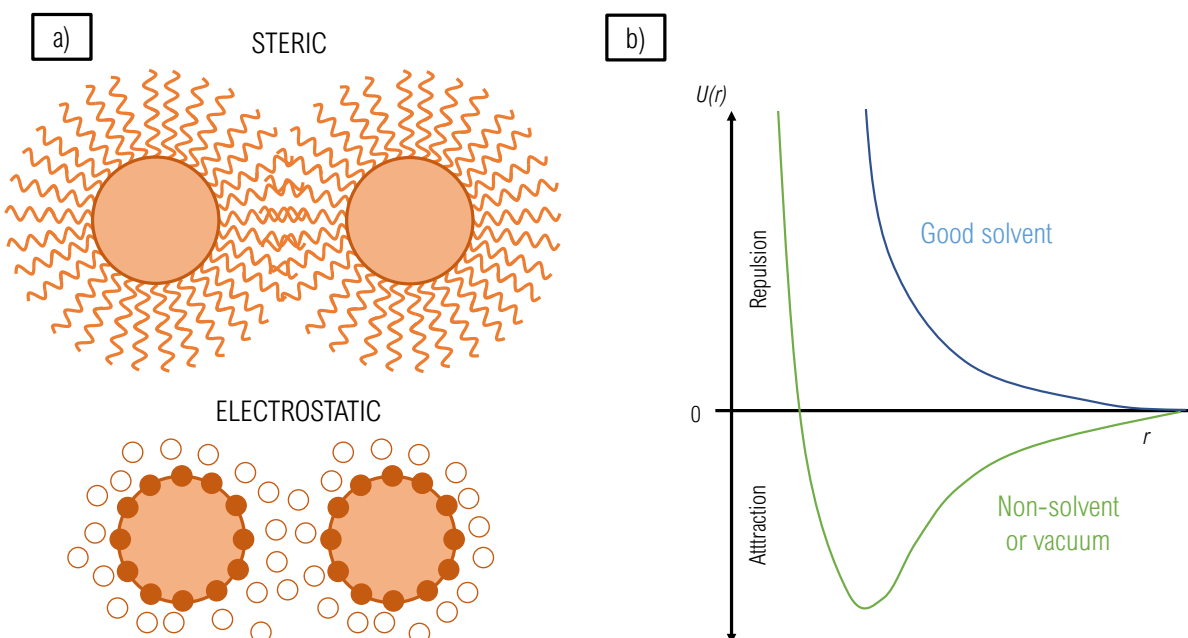
Figure 7: (a) Illustration of an interacting pair of NPs in case of sterical stabilization (hydrocarbon surface ligands) and electrostatic stabilization (ionic surface ligands); (b) Interaction potential U dependency of interparticle distance r in case of good and non-solvents. A good solvent shows pure repulsion between the NPs, while attractive forces are established at an intermediate distance in the case of a non-solvent. Adapted from reference 9.

3.3   Ligand exchange reactions

Surface ligands with L- or X- type headgroups and hydrocarbon tails allow very good control over nucleation and growth of NPs. However, such ligands might need to be replaced with other surface-binding species better suited for the end application. It is necessary that a bound ligand desorbs from the NC before a new one may enter from solution to attach to the surface. In case of nonpolar solvents, all species involved in the reaction should be electrically neutral, meaning that a direct exchange between X- and L-type is highly unfavourable in such environments due to neutrality disturbance. L-type ligands would rapidly adsorb and desorb from the NP surface at room temperature, while X-type ligands remain tightly bound because of the electrostatic penalty for charging induced by self-desorption of X-type ligands. The use of polar solvents lifts the requirement for neutrally NPs surfaces, allowing additional ligand exchange pathways.

Different types of ligands have been found as convenient replacement of insulating organic ligands. For example, many molecular metal chalcogenide complexes (MCCs) can enable strong electronic coupling in NC solids [22]. The MCC ligands contain main group or transition metals bound to the NC surface through chalcogenide bridges. Many MCCs can be synthesized by
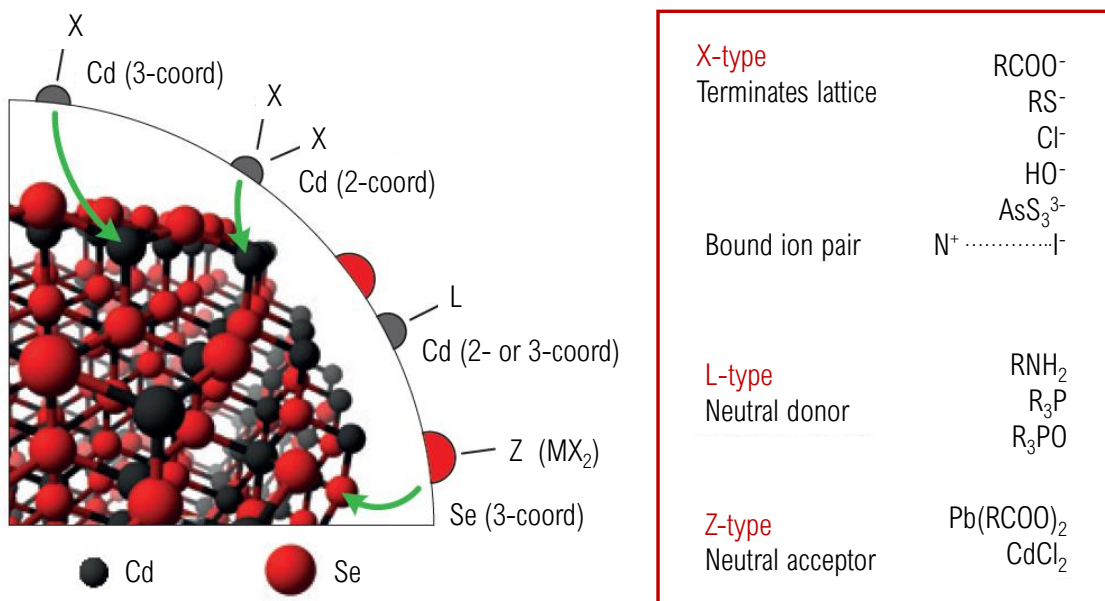
Figure 8: Possible metal-ligand bonds at the surface of CdSe NPs. Anionic X-type ligands bind to surface cations to restore charge neutrality. Neutral L-type electron donor ligands with lone pair datively coordinates at surface metal atoms. Neutral Z-type electron acceptor ligands bind to electron-rich undercoordinated Se atoms. Adapted from reference 9.

dissolution of bulk main group or transition metal chacogenides in hydrazine. Excess chalcogen is usually added to form soluble anionic species such as thiostannate ligand $Sn_2S_6^{4-}$ with hydrazinium ($N_2H_5^+$) as the counter ion. MCCs can be converted into semiconducting phases by gentle heat treatments, generating inorganic nanocrystal solids. For example, $Sn_2S_6^{4-}$ neutralized by volatile hydrazinium counterions decomposes at 180 °C: $(N_2H_5)_4Sn_2S_6 \rightarrow SnS_2 + 4N_2H_4$ = $2H_2S$. If nonvolatile or carbon-containing impurities are not present, SnS_2 phase crystallizes into pure electronic-grade semiconductor [22]. The presence of foreign metal ions in a close proximity to the NP surface in the case of MCC ligands is considered to have possible effects on the chemical and physical properties of the NPs. For example, metal ions from MCC ligands can participate in redox processes (as the case of $Sn_2S_6^{4-}$ ligands, that can switch between Sn^{IV} and Sn^{II} oxidation states). This complications could be avoided by introducing metal-free inorganic ligands, such as chalcogenides and hydrochalcogenides (S^{2-}, HS^-, Se^{2-}, HSe^-, Te^{2-}, and HTe^-), mixed chalcogenides (TeS_3^{2-}), as well as OH^- and NH_2^- [23].

The ligand-exchange process is performed in solution-phase, and it consents to prepare inks composed of smaller inorganic ligand-capped NPs in a single step. The method is shown in Figure 9: native ligand-capped CZTS NPs are dispersed in chloroform and then mixed with

ammonium sulfide in formamide (FA), followed by stirring of the mixture, resulting in the transformation of S^{2-}-capped CZTS NPs to the FA phase.
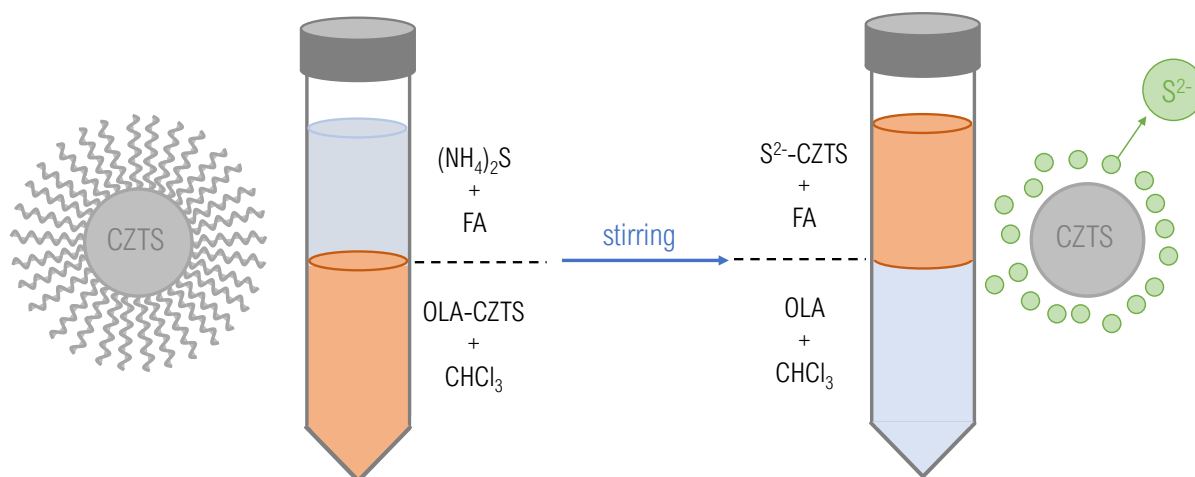
Figure 9: Scheme showing the process of solution-phase ligand exchange. Native-ligand capped CZTS NPs undergo ligand exchange when the chloroform mixture they are dispersed in is mixed with ammonium sulfide in formamide (FA). After stirring, the NPs result covered in S^{2-} ions. Adapted from reference 8.

3.4   Surface ligands and nanocrystal electronic structure

Optical, electrical, magnetic and catalytic properties of NPs can be directly influenced and tailored by surface ligands. Such effects can be explained, for example, by considering semiconductor quantum dots (QDs). QD films allow bandgap tuning through the quantum size effect, as valence and conduction bands are split into discrete, quantum-confined states. However, the broken bonds at the surface of the QD contribute with a set of electronic states lying between highest occupied and lowest unoccupied quantum-confined orbitals of the QD (Figure 10 (a)). This imperfect passivation of the surface promotes non-radiative recombination of charge carriers that can be detrimental for the performance of devices based on such QDs: such states behave as traps for electrons and holes [9] [24]. By bonding to the NP surface atom, the ligand generally passivates the surface forming a new set of molecular orbitals with bonding (σ) and antibonding (σ^*) character: the strong covalent bond between surface atom and ligand shifts the energy of σ- and σ^*- orbitals outside the bandgap, removing possible trap states.
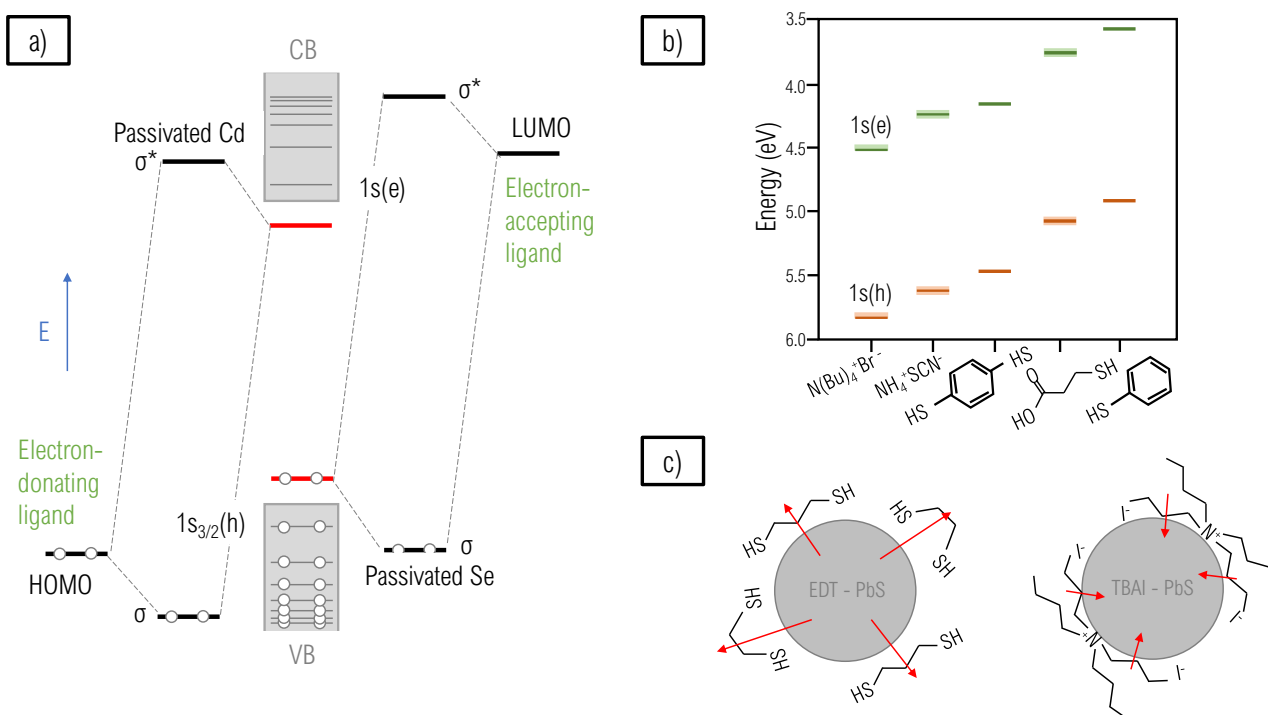
Figure 10: (a) Simplified molecular orbital diagram of a CdSe QD showing that the energies of Cd and Se surface states (red levels) are pushed away from the bandgap in presence of ligan binding. Adapted from 9; (b) Surface ligands influence the energy of the highest occupied and lowest unoccupied states of PbS quantum dots, for the following ligands: bromide, thiocyanate, benzenedithiol, 3-mercaptopropionic acid and benzenethiol. Adapted from 25: VB maximum was measured by UPS, while the CB minimum was determined combining UPS results, optical absorption spectrum results and the Coulombic stabilization energy of the confined electron and hole theorized by Brus; (c) Surface-bound molecules shift QD energy level(leading to p- or n-type behaviour) by inducing variable surface dipoles. Tetrabutylammonium iodide (TBAI) treated Pb NPs show n-type behaviour, while ethanedithiol (EDT) renders PbS p-type. Adapted from 26.

The absolute energy of QD electronic states can also be affected by the presence of ligands. In Figure 10 (b), the 1s(h) (HOMO) and 1s(e) (LUMO) states of PbS QDs, measured with UPS, are shown [25]. Then capped with different ligands, both HOMO and LUMO shift, and the observed variation is large enough to be compared to the energy bandgap itself. This effect is caused by electrostatic forces generating at the interface between ligand and QD surface (Figure 10 (c)). When a surface dipole is established at the surface of the QD, the electric field potential shifts all energy levels up, if the dipole points toward the NP center, or down in the opposite case. This electronic reconstruction results in an overall n- or p-type behavior of the NPs when integrated in optoelectronic devices [26].

3.5   Characterization of the NP surface

Experimental study of NPs surfaces becomes very challenging, due to the nanometre dimensions and heterogeneity of the surfaces. No technique that provides atomic-resolution reconstruction is now available for the study of the NC capping layer. However, different experimental methods can be applied to obtain complementary information about the capping layer structure, the NP-ligand bonding, and interaction between ligand molecules and surrounding environment [27] [28]. The mayor questions about the interface that can be answered by spectroscopic, scattering, imaging and computational techniques can be divided in the following components: (i) what is the composition and structure of the ligand molecules?; (ii) how is the chemical bonds between ligands and NP surface?; (iii) and what are the effective properties of the whole capping layer, such as geometry at the interface, effective thickness, density and dielectric constant [28]?

Reference 9 offers a summary of useful techniques. Vibrational spectroscopy has found its utility in characterizing the structure of ligand molecules. The width and position of infrared resonances, obtained with **Fourier transform infrared spectroscopy** (FTIR), can be used to investigate chain conformations and molecular order of the capping layer. **Raman spectroscopy** is particularly useful for characterizing inorganic ligands with heavy atoms vibrating at low frequencies. **Small-angle X-ray scattering** (SAXS) has been used to study the effective thickness of the NP capping layer. **Trasmission electron microscopy** (TEM) allows real-space imaging of NPs and, in some cases, their surface ligands, and finds its advantage in the ability to examine NPs at a single-particle level. Computational techniques, like **Density functional theory** (DFT), can partially compensate for difficulties associated with experimental probing of NP surfaces. DFT is used to model electronic interactions between different NPs facets and ligands. **X-ray Photoelectron Spectroscopy** can be used to measure the chemical environment at the interface between NP and ligand. **Ultraviolet Photoelectron Spectroscopy** has been already introduced before as useful technique in the study of the valence band of QDs, while **Inverse Photoelectron Spectroscopy** can provide helpful information for the understanding of the conduction band. For the purpose of this thesis, photoelectron spectroscopy (PES) has been applied to the study of CZTS NPs, and in the following chapter some theory about PES will be given.

4 Photoelectron Spectroscopy (PES)

This section is based on references 29, 30 and 31.

4.1 Basic principles

Spectroscopy techniques play a vital role in the understanding of the internal structure of materials. Their powerful usefulness stands in the ability to record responses of different interactions between specific radiation and matter. The techniques can be classified depending on the type or frequency of the incident radiation used or the nature of the interaction of the radiation with matter. In the latter case, some examples could be absorption spectroscopy, when the absorption spectrum of a material is studied, or emission spectroscopy, when the emitted radiation or particles from a material are the main interest. Here photoelectron spectroscopy (PES) and Auger electron spectroscopy come to hand when emitted radiation is composed of electrons.

In a general photoelectron spectroscopy system, the sample is illuminated by a radiation of suitable energy which ejects photoelectrons, then guided by electron optics into an electron energy analyzer which sorts electrons by means of their energy. Figure 11 (a) shows schematically the typical PES set up.

The ejection of photoelectrons is made possible by a phenomenon called the *photoelectric effect*, discovered by Hertz in 1887: when a material is illuminated with a light source with suitable frequency, electrons from occupied energy levels are ejected with some kinetic energy. In PES, the illuminating radiation carries comparable energy to the one required to remove electrons from energy states of the material.

By studying the kinetic energy of the emitted electron, it is possible to obtain information about the energy levels from which it has been extracted. Depending on the occupied orbital from which it is ejected, the electron will posses a specific threshold frequency, ν_0, that defines its binding energy, E_B. When an incoming radiation with frequency ν greater than ν_0 hits the material, photoelectrons are ejected with kinetic energy E_{kin} given by *Einstein's equation*:

$$E_{kin} = h\nu - h\nu_0 - \phi = h\nu - E_B - \phi \tag{1}$$

where ϕ is the work function of the material. However, the analyser possesses a different work function ϕ_A, that is generally different from the one of the sample material. Equation 1 can be modified taking in consideration this difference: when a conductive connection between the sample and the analyser is provided, their Fermi levels align, resulting in a difference in measured kinetic energy $E_{kin,A}$ with respect to E_{kin} by the difference in work functions. Equation 1 can
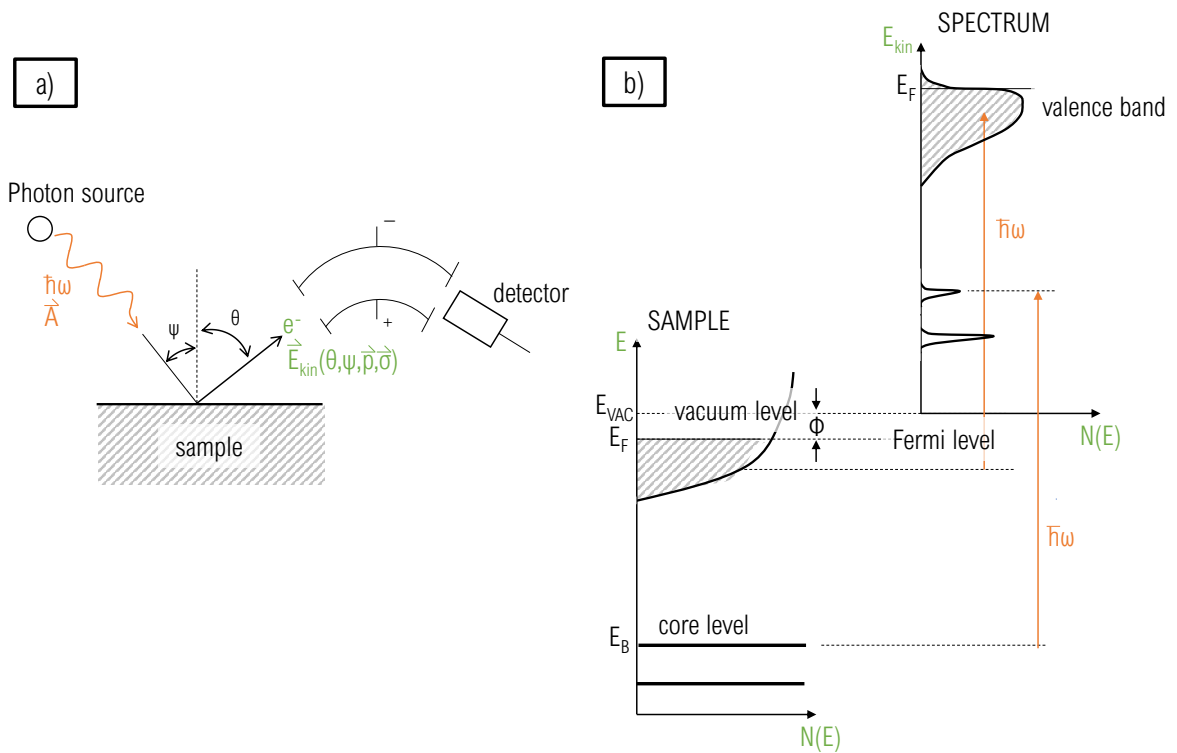
Figure 11: (a) Schematic PES set up: excited electrons are analyzed with respect to their kinetic energy E_{kin} and their momentum p. The directions of $\vec{p}$ are obtained from θ and ψ, which are the polar and azimuth angles under with the electron leaves the surface; (b) Relation between the energy levels in a solid and the electron energy distribution produced by photon of energy $h\nu$. The abscissa for the photoelectron spectrum ($E_{kin} = 0$) corresponds to the vacuum level. Solids are characterized by core levels and valence band, and PES provides information on the energy distribution in a material. In a metal, E_F is found at the top of the valence band and has work function ϕ of separation from the vacuum level. Figure based on reference 31.

then be rewritten:

$$E_B = h\nu - E_{kin,A} - \phi_A \tag{2}$$

The principle of PES is shown in Figure 11 (b), where the relationship between the energy levels of a solid and the electron energy distribution produced by photoemission is showed.

The attractiveness of PES resides in the fact that the properties of the photoelectrons basically reflect the electronic eigen states of the investigated system. Depending on the energy levels that want to be studied in the material, one can distinguish between **Ultraviolet Photoelectron Spectroscopy (UPS)**, mainly for the (angle resolved) investigation of valence band states (ARPES), and **X-ray Photoelectron Spectroscopy (XPS)**, which provides information on the core-level states at higher binding energies. Two different types of excitation sources are available under laboratory conditions and allow the distinction of the previous techniques, namely UV line spectra of discharge lamps for energies in the range of approximately 10–50 eV,

generally with noble gases like helium (He I$_\alpha$: 21.23 eV, He II$_\alpha$: 40.82 eV), and the characteristic lines from the X-ray source, for which the most commonly used anode materials are aluminum (Al-K$_{\alpha1,2}$: 1486.6 eV) and magnesium (Mg-K$_{\alpha1,2}$: 1253.6 eV) [31]. Other materials can of course be used in anodes, like in the case of the system used in laboratory for this thesis, where the XPS setup has yttrium and magnesium anodes.

4.2   Three-Step Model and Mean Free Path

The photoemission process is generally described through the so called *three-step model*: first the photoelectron is ejected from the orbital thanks to the photoelectric effect, then it travels through the solid up to the surface, possibly losing some energy due to inelastic scattering, and finally it is emitted into vacuum (Figure 12).
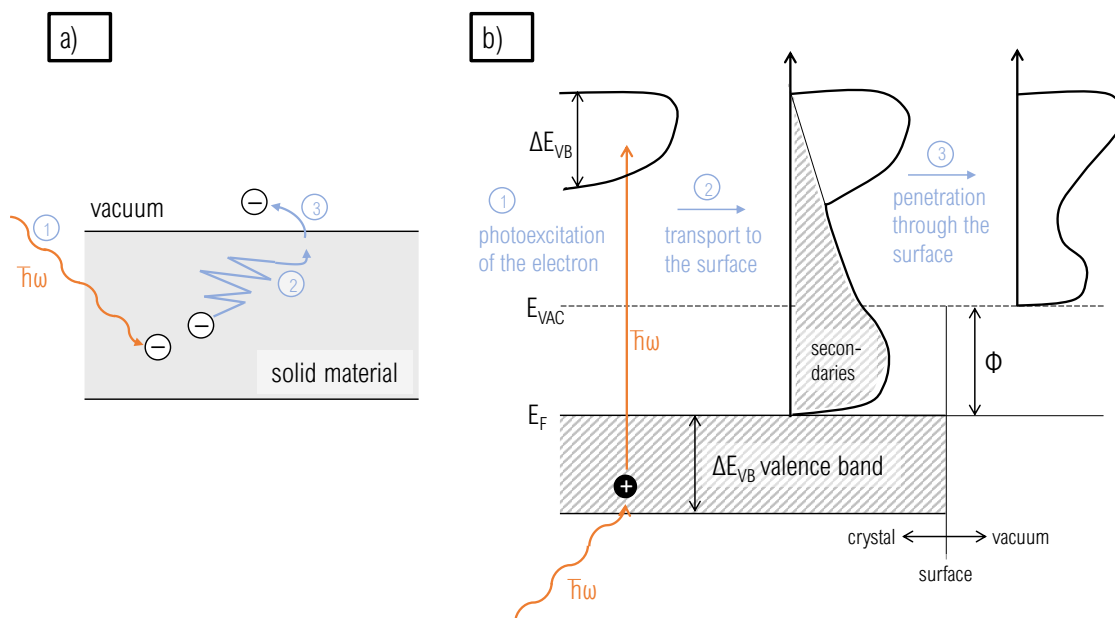
Figure 12: (a) Three-step model for photoemission process; (b) (1) photoexcitation of electron, (2) transport of electron towards the surface with concomitant production of secondaries, (3) penetration through the surface barrier and escape into vacuum.

To be able to reach the detector, the electron needs to travel through the sample without losing much of its energy due to inelastic collisions and finally overcome the energy barrier at the surface. For this reason, the electrons possessing kinetic energy to reach the detector are divided in primary electrons, which suffer no inelastic losses, and secondary electrons, that underwent multiple scatterings. For PES purposes, primary electrons are of key interest to analyze the electronic structure of the material. The intensity of the primary electrons having

certain energy E_{kin}, $I_p(E_{kin}, h\nu)$, can be obtained in terms of three functions that represent the probabilities of each step of the three-step model: the *photoexcited electron distribution* $P(E_{kin}, h\nu)$, the *transmission function* $T(E_{kin}, h\nu)$, and the *escape function* $D(E_{kin})$.

$$I_p(E_{kin}, h\nu) = P(E_{kin}, h\nu) \times T(E_{kin}, h\nu) \times D(E_{kin}) \tag{3}$$

$P(E_{kin}, h\nu)$ is related to the probability of exciting the electron from low-energy occupied states to unoccupied high-energy vacant states. Giving $\lambda_e(E_{kin})$ to be the electron inelastic mean-free path and $\lambda_{ph}(h\nu)$ the attenuation length of photons, the *transmission function* $T(E_{kin}, h\nu)$ representing the inelastic scattering probability is given by:

$$T(E_{kin}, h\nu) = \frac{\lambda_e(E_{kin})/\lambda_{ph}(h\nu)}{1 + \lambda_e(E_{kin})/\lambda_{ph}(h\nu)} \tag{4}$$

$T(E_{kin}, h\nu)$ can also be expressed by the *absorption coefficient* $\alpha(h\nu)$, considering that $\alpha(h\nu)$ equals the inverse of $\lambda_{ph}(h\nu)$. As $\lambda_e(E_{kin})$ in solids is very short for a wide range of E_{kin}, PES is a rather surface sensitive technique. The purpose of PES is to detect primary electrons to obtain information about the material structure, but some photoelectrons during their way to the surface might experience electron-electron, electron-phonon or electron-impurity interactions, which the first is the main cause of energy loss. Generally, $\lambda_e(E_{kin})$ shows the minimum value at energy corresponding to interband transition. The parameter $\lambda_e(E_{kin})$ should then depend on the material itself, but it has been demonstrated that for most materials it follows a "universal curve", depicted in Figure 13, where the minimum happens in the range of 20-100 eV with values often close to 2-5 Å, and as the energy of electrons increase the value is still below 50 Å. For energies below the minimum, the value of $\lambda_e(E_{kin})$ increases as well. With so small values of inelastic free path, it is possible to probe only a few atomic layers and for this reason PES is a very surface sensitive technique and ultra-high vacuum is necessary (to avoid further collisions of the emitted electrons with gas molecules in the chamber, and keep the sample clean from additional impurities). Moreover, as the intensity of the detected photoelectrons decreases exponentially by $z/\lambda \cos\theta$, where z is the depth in the sample and θ the angle emission, one can define the information depth (ID), identified with the specimen thickness from which a specified percentage (generally 95% or 99%) of the detected signal originates. It is important to know what is the extension of the ID in order to probe homogeneous samples over depths of up to at least the ID, otherwise alternative analytical strategy should be considered [32].

After the electrons reach the surface without undergoing any energy loss, they still need to overcome the potential energy barrier $E_F + \phi$. Assuming that the excited photoelectrons move like plane waves, one can define the condition of the *escape cone* perpendicular to the surface of the material, from which the electrons are able to escape to vacuum. An *opening angle* θ
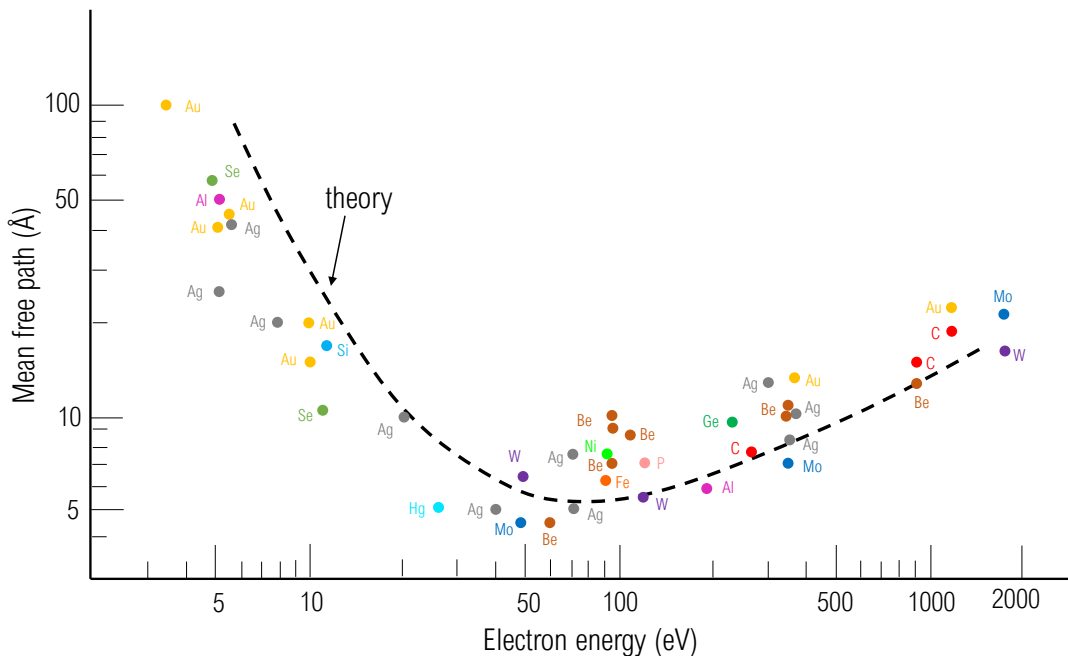
Figure 13: Electron mean free path as a function of electron energy for various elements, adapted from reference 33.

relative to the normal to the surface can be obtained from the following equation:

$$\cos\theta = \Big(\frac{\phi + E_F}{E_{kin}}\Big)^{1/2} \tag{5}$$

Electrons approaching the surface with energy smaller than $E_F + \phi$ will not escape the surface. The *escape function* of electrons having energy greater than $E_F + \phi$ will then depend on the angle θ: when perpendicular to the surface, electrons will have the highest chance to escape, and the least when parallel.

$$D(E_{kin}) = \begin{cases} \frac{1}{2}[1 - \cos\theta] & \text{for} \quad E_{kin} > E_F + \phi \\ 0 & \text{otherwise} \end{cases} \tag{6}$$

4.3   X-ray Photoelectron Spectroscopy (XPS)

The spectrum shown previously in Figure 11 (b) does not represent truthfully how a real PES spectrum looks like. In addition to photoemission peaks, there are different processes happening at the same moment that produce different features. It is important when analysing an XPS spectrum to recognize all the peaks and by which specific process they are caused.

The first of all these effects is the background. A broad signal is created by electrons that are inelastically scattered before reaching the analyzer. This phenomenon generates an increasing intensity in the background as scanning for higher binding energies (and so lower kinetic energy) of the photoemitted electron.

Of more interest are secondary features visible relative to the background or in general some specific characteristics of the XPS peaks:

1. **Auger peaks** - When a photon carries high energy, a different emission process can occur, and an Auger electron can be detected. These electrons are produced when the energy released by the relaxation of an higher shell to a vacancy in a lower one, is given to another electron that leaves the atom with a kinetic energy equal to the difference in energy of the two shells. The kinetic energy of the electrons are independent on the energy of the incoming probe as they depend only on the orbit configuration of the atom, and give as well information on the composition of the sample. Figure 14 illustrates the Auger process compared to direct photoemission;
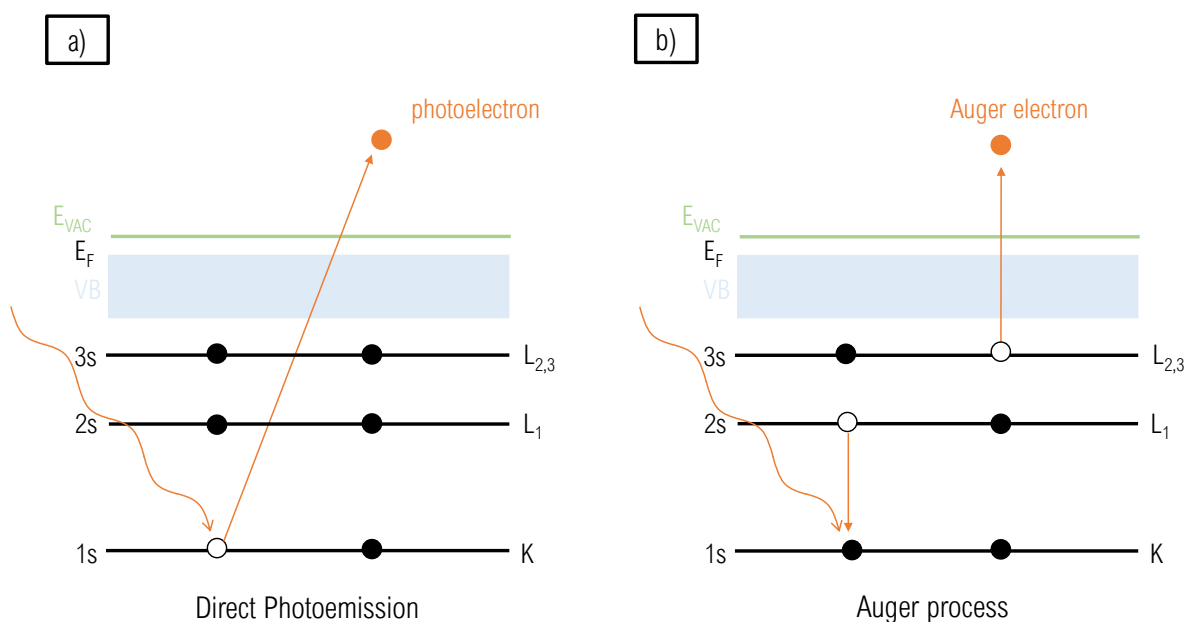
Figure 14: Schematic diagram of the emission process of (a) a photoelectron compared to (b) an Auger electron. Auger electrons are produced when a vacancy created by a photon in a core level gets filled by and electron from an higher shell. The energy difference between the two shells is given in kinetic energy to an outer shell electron that is then emitted. The kinetic energy of the Auger electron is then independent from the incoming photon energy.

2. **Chemical shifts** - XPS is a powerful tool because it does not only provide information about the element composition of the sample, but also about the configuration of the chemical bonds in which the atoms occur. This effect can be recognized through what are called "chemical shifts", as they result in a shift in binding energy depending on the bond. The main contributor to this effect is the change in electrostatic screening of core orbitals. Explained with the difference between the binding energy of the 1s level in lithium Li as pure metal and the same metal but in oxide form (Figure 15): when considering pure Li, the conduction electrons of the higher levels (2s) of Li atoms screen the nucleus and the binding energy for the 1s results lower than in the case of the oxide, where the electrons from the 2s are used to create the bond with oxygen, and the positive charge of the nucleus attracts more strongly the close 1s electrons. The spectrum for Li1s will show then two separated peaks for Li metal and Li oxide;
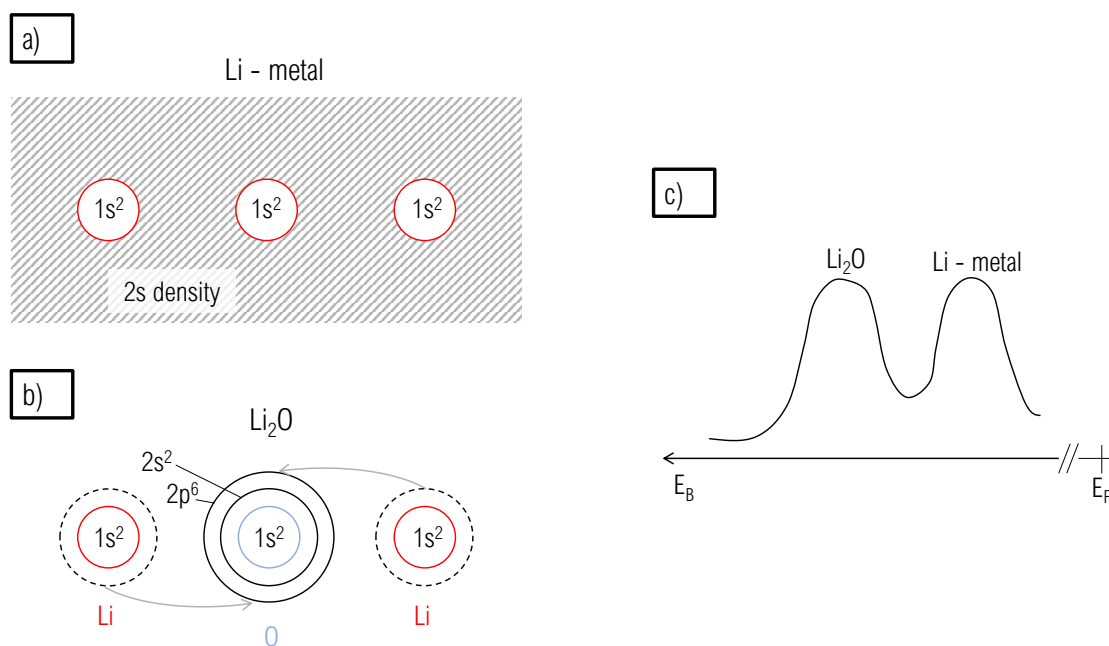
Figure 15: (a) Li - metal: 2s electrons form a band, and their wave function is therefore only partly at the site of a particular atom; (b) Li_2O: each Li atom donates its 2s electron totally to the 2p chell of O such that a closed $2p^6$ configuration is obtained. Li 2s electron has no part of its wavefunction near the Li atom. the 1s electron of Li therefore feels a stronger Coulomb interaction with the Li nucleus than in the case of Li-metal, where the $1s^2$ shell is screened by the 2s valence band; (c) PES spectrum representing the chemical shift of Li 1s in case of Li-metal and Li_2O.

3. **Spin-orbit splitting** - Due to spin-orbit coupling, shifts in atomic energy levels arise and this feature is detected in XPS. For each shell, the total angular momentum, given

by $j = |l \pm s|$, where l is the orbital angular momentum and s the spin, can take two different values. In XPS spectrum, this results in two peaks called "doublet pair". The ratio between the intensities of the two peaks are given by

$$r = \frac{2(l+s)+1}{2(l-s)+1} \tag{7}$$

meaning that for orbitals p, the intensities would appear in ratio 2:1, and in orbitals d in 3:2.

4. **Plasmon and satellite peaks** - Satellite peaks can be detected in case of a non perfectly monochromated incoming probe. This causes a shift of energy with respect to the main spectral line. Plasmon peaks arise from the loss of energy due to plasmon excitation: plasmons can be "intrisic", when the photohole deexcites, or "extrinsic", when plasmons are excited along the path of the photoelectron from bulk to surface of solid.

4.4   Inverse Photoelectron Spectroscopy (IPES)

PES techniques have the effective potential to analyze the structure of occupied states of a material. **Inverse Photoemission Spectroscopy (IPES)** can be considered as a complementary technique to UPS in order to determine the band gap of a specimen. In fact, in IPES monochromatic electrons are impinged onto the solid and accommodated in the relatively high energy part of the unoccupied electronic states. When these electrons relax to the lower energy part of the unoccupied states, they emit photons. The energy of the incoming electron E_i and and the energy level at which it relaxes to E_f, differ then of the amount carried by the emitted photon:

$$E_i = E_f + h\nu \tag{8}$$

The binding energy E_B of the electron can then be identified by the difference in energy between E_f and the Fermi energy E_F.

The term "inverse" derives from the fact that in normal PES the mechanism sees a photon-in and electron-out while for IPES the process is reversed. IPES can be measured in a wide energy range. There are two different detection methods for the emitted photons. The first method, called **isochromat spectroscopy** (BIS - Bremsstrahlung Isochromate Spectroscopy), is set with constant detected photon energy $h\nu$ while scanning the excitation electron energy. The second method, **spectrograph mode** or IPES, obtains the spectrum of emitted photons at a defined incident electron energy. For the sake of this experiment, only isochromat spectroscopy will be considered, even if the analysis will be referred to as IPES. However, the difference between the two methods is shown in Figure 16.

The yield of IPES is generally really low compared to PES and it can be expressed through
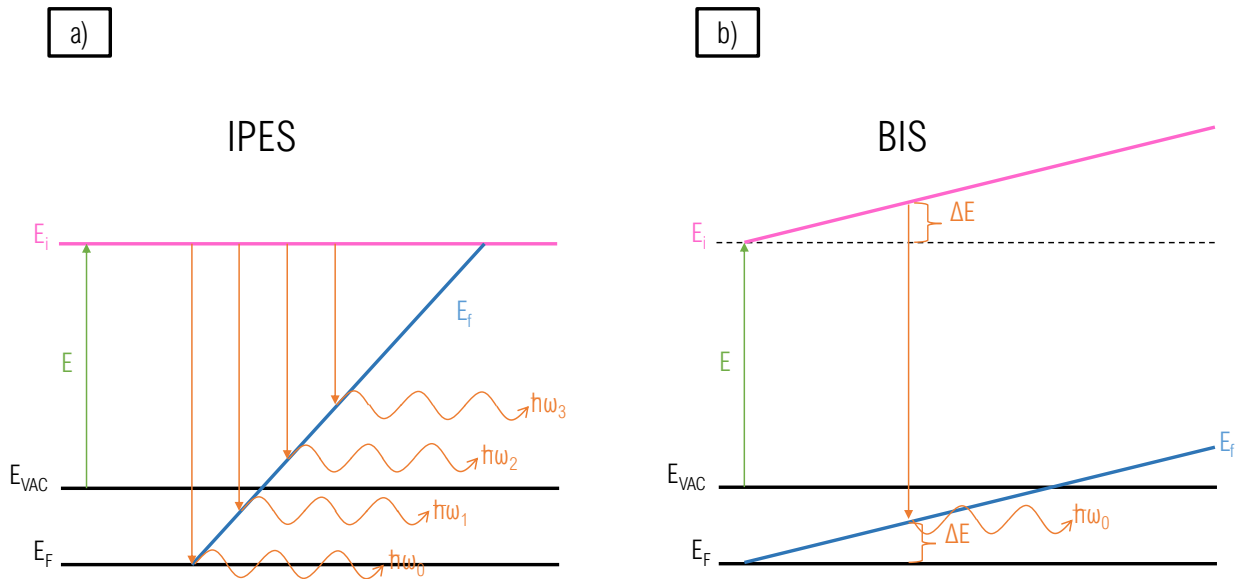
Figure 16: Illustration of the difference between the (a) IPES and (b) BIS methods: in IPES the spectrum is recorded by keeping the energy of the incident electrons constant at the value E_i, while in BIS mode the energy of the detected photons is set and the excitation electron energy scanned over a range.

R, the ratio of the inverse photoemission cross-section to the photoemission cross-section. R is inversely related to the ratio of the square of the wavelength of the emitted particle and the photon:

$$R = |\frac{\lambda_e}{\lambda_{ph}}|^2 \tag{9}$$

In the UV energy range characteristic of inverse photoemission, the ratio R in Equation 9 typically has a value of 1×10^{-5}. It is precisely for this reason and for its limited resolution (0.3 eV at best) that the development of the technique as a viable spectroscopy has so lagged behind the development of PES [31] [34] .

4.5   Resonance Photoelectron Spectroscopy (RPES)

Resonance Photoemission Spectroscopy (RPES) is a technique that finds its usefulness in the investigation of VB features in solids. In RPES photoemission is produced with a photon of an energy $h\nu$ very close to the absorption threshold of a core level. The direct PE of the VB electron can interfere with Auger core-valence-valence (CVV) decay electron that are emitted in a Super Koster-Kronig Auger process. In the CVV Super Koster-Kronig Auger process a two hole state

is produces in the VB. Figure 17 shows the difference between direct photoemission and Super Koster-Kronig Auger process. Considering the case of metallic Ni, the direct photoemission process occurs from the valence electrons: a photon excites an electron from the 3d band and bring it to the vacuum with kinetic energy E_{kin}, $3p^6 3d^9 + h\nu \rightarrow 3p^6 3d^8 + e^- [E_{kin}]$. In the recombination process, a photon first promotes a 3p electron to be excited to the VB of Ni (3d level), then the extra electron decades back from 3d to 3p states, emitting another VB electron with E_{kin}, $3p^6 3d^9 + h\nu \rightarrow 3p^5 3d^{10} \rightarrow 3p^6 3d^9 + e^- [E_{kin}]$. The Super Koster-Kronig Auger process therefore overlaps with the direct photoemission for photon energies equal (or in the range) of a core level transition. The effect of this overlapping is an increase in the signal, as more electrons are excited to the same kinetic energy but by different processed.
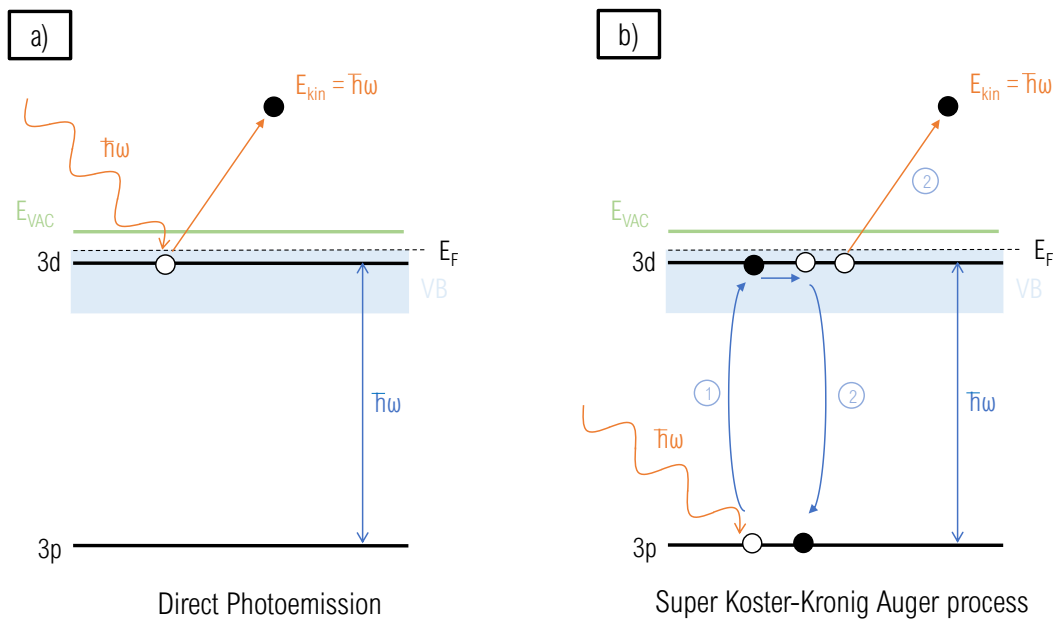
Figure 17: (a) Direct and (b) resonant photoemission processes at photon energy $h\nu$ equal to an admitted level transition of the material. In the direct PE, and electron is emitted from the VB of the material to vacuum. The resonance process articulates in 2 steps: (1), an electron is excited from the Ni3p into the Ni3d state, while later (2) it decades back to Ni3p by emitting a Ni3d electron. Both processes lead to the emission of a 3d electron and have same initial and final state.

RPES is a powerful technique as it enables the discrimination of active and inactive orbital contribution to the VB of materials by exciting specific level transitions. RPES can also be used to characterize intermediate band gap materials, by probing the orbital character of the dopant species [35].

4.6   X-ray sources

The quality of an X-ray beam is determined by several aspects of the X-ray source that produces it. First of all there is the number of photons emitted per second, and next the collimation of the beam. This describes how much the beam is spread out and diverges as it propagates. Third, it is important to define how large the source area is: the smaller this area is, the smaller the X-ray beam can be focused to obtain a correspondingly small image size. Last, there is the spectral distribution of the X-ray source: some sources produce smooth spectra, others have peaks at certain photon energies. When making comparison between sources is then important to define the range of photon energies that contribute to the measured intensity. The photon energy range is chosen by convection to be 0.1 % of the relative energy bandwidth (BW) [36]. All these aspects can be combined into a single quantity, called the **brilliance** B:

$$B = \frac{photons/s}{(mrad^2)(mm^2 \times sourcearea)(0.1\%BW)} \tag{10}$$

The peak brilliance of X-ray sources has grown tremendously since the discovery of X-rays in 1895, and this evolution is shown in Figure 18.

Figure 18: Schematic diagram showing the evolution in relative peak brilliance of X-ray sources compared to the first X-ray tube in 1895. Adapted from reference 37.
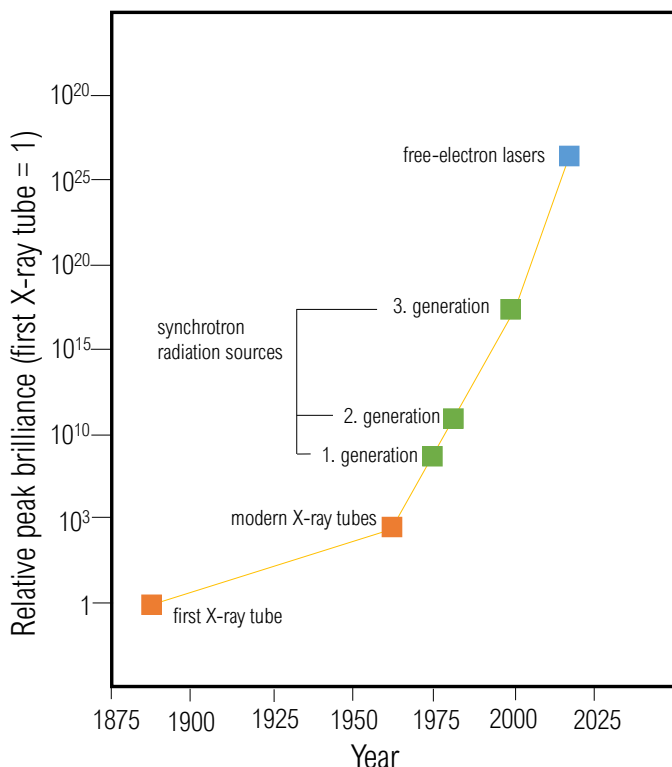
Since the synchrotron radiation was first detected in 1947 at Cornell, three generations have been defined. The first generation synchrotron-radiation is termed "parasitic" as X-rays pro-

duced as byproduct of particle-physics experiments were used. A second generation of X-ray sources was established in the early 1970s, while after the appearance in the early 1990s of the undulators, a much more brilliant third generation of sources established. A new generation of X-ray sources is now on the rise: the X-ray free-electron lasers (FELs) [37].

4.6.1   X-ray Tube

The X-ray tubes that are used in laboratories are result of only marginal technical improvements compared to the first tube invented by W.D. Coolidge in 1912. Coolidge from General Electric Research Laboratories in New York developed a device where electrons were produced by a glowing filament and subsequently accelerated towards a water-cooled metal anode (Figure 19 (a)). High voltage and current could be independently varied, and the limitation of intensity was only determined by the cooling efficiency. The X-rays emitted from electron impinging on a metal anode generate a spectrum, characterized by two components. One, known as *bremsstrahlung radiation*, represents the continuous part due to decelerated electrons in the metal: such continuum has a peak corresponding to the high voltage applied to the tube. Superimposed to the bremsstrahlung radiation there is a sharp line spectrum generated by fluorescence: when an electron collides with a metal atom, an atomic electron from an inner shell can be removed and a vacancy created. An electron from an outer shell relaxes into the vacancy producing a characteristic X-ray with energy equal to the difference in energy of the two shells (Figure 19 (b) and (c)).

Major drawbacks of X-ray tubes are the generation of satellite peaks and the untunability of the lines. Satellite lines at slightly shifted energies to the main peak originate from simultaneously ionised shells in the atom. When a vacancy in an inner shell, for example a K-shell, is filled by an electron from an L-shell, a new vacancy is generated in the L-shell and the the total energy of the shell is shifted. The impossibility of tuning of the X-ray source derives from the fact that the energy of the produced X-rays depends on the anode material and can not be independently chosen. Synchrotron sources do not have these drawbacks, and have a brilliance which is enormously higher than that of standard laboratory sources.

4.6.2   Synchrotron radiation

This section is based on references 38.

Synchrotron radiation facilities are characterized by their ability to produce highly parallel and narrow beams of x-rays with high intensity. A schematic illustration of a synchrotron source is shown in Figure 20.
A synchrotron consists of five main components. These are:

1. The **electron source**, generating electrons normally by thermionic emission from a hot
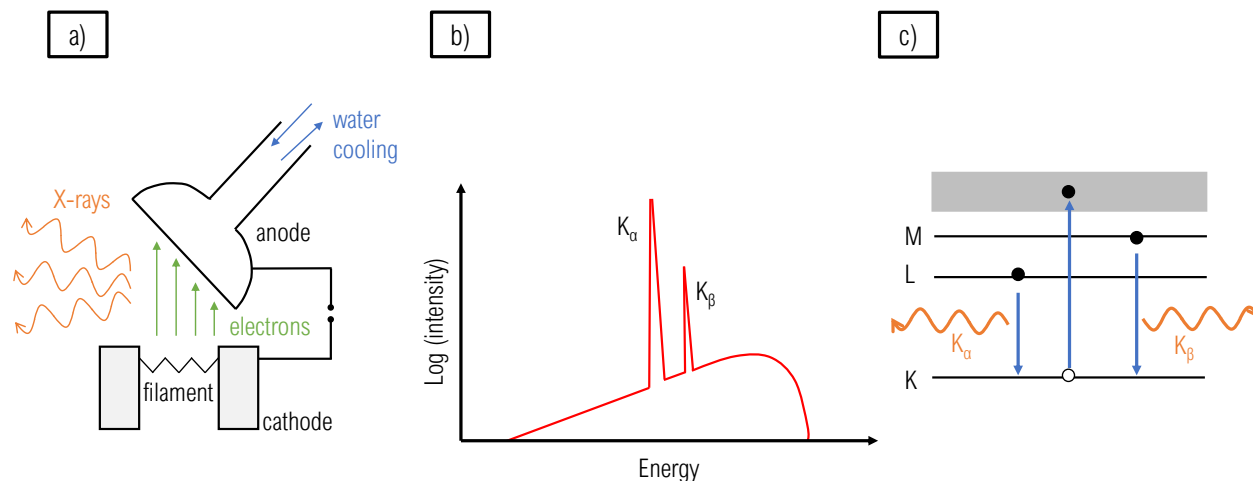
Figure 19: (a) Schematic diagram of Coolidge X-ray tube Adapted from reference: a filament is heated and emits electrons, that accelerate towards a metal anode thanks to an applied high-voltage, and characteristic X-rays are produced; (b) Typical spectrum of an X-ray tube, showing continuum background, given by bremsstrahlung radiation, and discrete spectral lines; (c) Illustration of the generation of spectral lines: X-rays are generated during the relaxations of electrons of outer shells to lower-energy shell vacancies. K_{α} transition originates grom transition between L and K shells, while K_{β} between M and K. Adapted from reference 36.

    filament. Such electrons are accelerated using a particle accelerator to about 100 MeV. In Figure 20, a linear accelerator (LINAC) is proposed as particle accelerator. Electrons are constantly lost in the machine due to collision with residual gas particles in the storage ring, therefore a regular supply is required;

2. the **booster ring**, where electrons coming from the LINAC are further accelerated and periodically injected into the storage ring to maintain a specified ring current. The supply generally is performed when the current drops to 1 - 1/e ≈ 70 % of the initial current;

3. The **storage ring**, where electrons are contained and maintained in a closed path by using an array of magnets. The magnets are generally of three types: dipole or *bending magnets* cause the electrons to change their path and follow a closed path; *quadrupole magnets* are used to focus the electron beam to compensate for Coulomb repulsion between the electrons; *sextupole magnets* correct for chromatic aberrations that arise from the focusing of the quadrupoles. The ring is structured so that bending magnets are placed in arc sections, while in straight sections insertion devices generate the most intense synchrotron
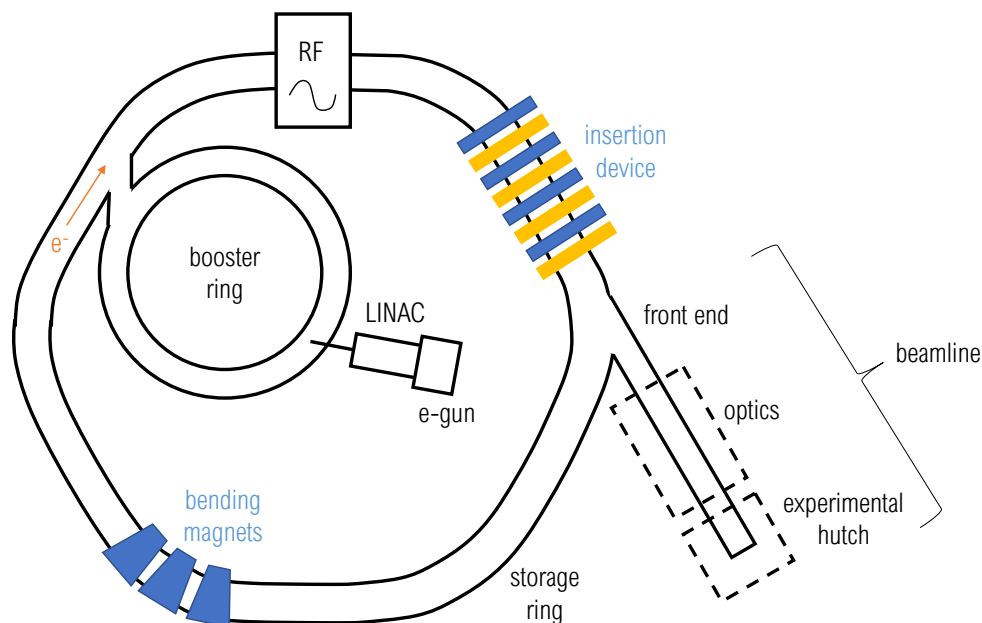
Figure 20: Schematic representation of the most important components of a synchrotron source. Electrons are emitted by a source (for example a filament in a e-gun) and accelerated by a linear accelerator (LINAC) into an evacuated booster ring. After being further accelerated in this ring, the electrons pass into the storage ring, where they maintain a closed trajectory thanks to bending magnets at arc sections. Insertion devices (wigglers, undulators, and bending magnets) generate X-rays tangential to the ring, forming the beamlines. A radio frequency source replenishes the energy lost by the electrons after emitting radiation. Adapted from reference 38.

    radiation;

4. The **radio frequency supply** (RF), that replenish the loss of energy that electrons lose in the storage ring due to collision and radiation emission;

5. The **beamlines**, that can be found along the axes of insertion devices and tangentially to bending magnets. The first section of a beamline is called 'front end' and has different functions: it isolated the beam and storage vacuums; it monitors the position of the photon beam; it defines the angular acceptance of the synchrotron radiation thanks to apertures. The beam is normally focused and/or monochromated in the optics hutch, before it enters the experimental hutch.

Insertion device radiation

As previously stated, synchrotrons are characterized by the use of insertion devices (IDs),

placed in the straight sections between the bending-magnet arc segments. For example, the synchrotron operated in this thesis, ASTRID2, is provided of multipole wiggler to produce a usable energy range from 20 eV to 700 eV. Such design results in a very small emittance of 12 nm and a beam size of less than 200×25 microns in the straight sections.

The brilliance and fluxes produced by IDs are significantly higher than bending magnets. The working principle of IDs is that electrons are forced to oscillate on a plane during their path in the ring. Such oscillations are caused by a set of magnets, generating magnetic fields that point alternatively up and down (see Figure 21).
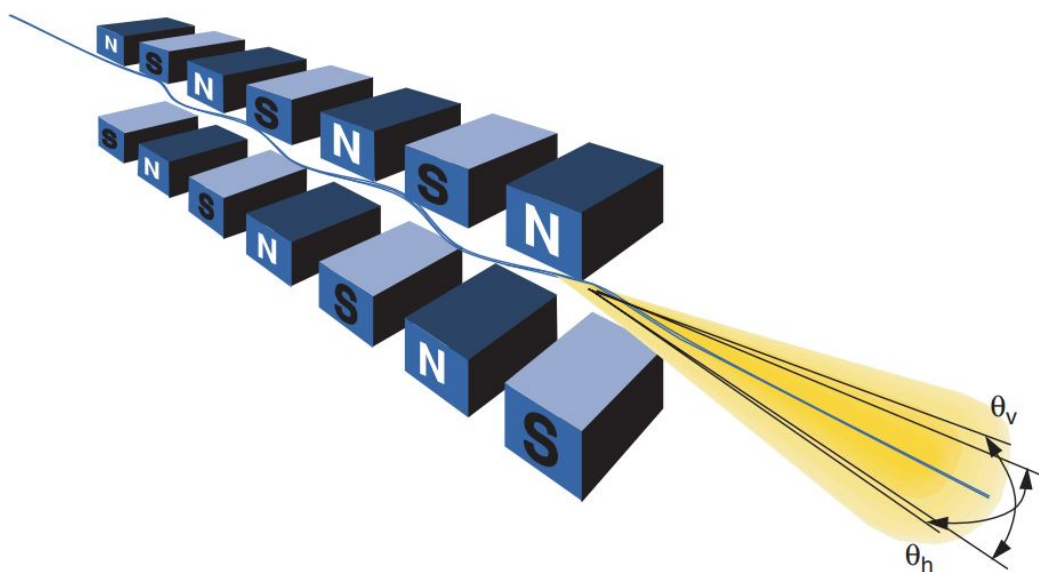
Figure 21: A schematic diagram of an insertion device. The angular spread in radiation is given in the horizontal and vertical plane by θ_h and θ_v, respectively. Adapted from 38.

IDs can be distinguished in two types depending on the degree to which the electrons are forced to deviate from a straight path, wigglers and undulators. To describe the difference between these two typologies, some basic theory about synchrotron radiation from relativistic electrons moving along a circular arc must be given. Electromagnetic radiation emitted by acceleration of a charged particle travelling at velocities that are small compared to the speed of light is isotropic, while in relativistic regime the generated beam of light radiates in the same direction as the electron motion. The features of the radiation can be described by two parameters: the angular frequency ω_0 (that is, the number of radians turned by the electrons per second), and on the kinetic energy of the electrons in the storage ring ϵ, given by the dimensionless parameter known as the Lorentz factor:

$$\gamma = \frac{\epsilon}{mc^2} \tag{11}$$

The natural opening angle of the narrow radiation cone in the plane perpendicular to the

storage ring is θ, that is proportional to $1/\gamma$. For typical ring energies of 1–8 GeV, is equal to 0.5–0.06 milliradians (mrad), respectively (1 mrad is approximately equal to 0.057 °) [38]. The parameter γ helps to define the difference between ID types. For angular excursions larger than the natural opening angle γ^{-1}, the radiation cones from each "wiggle" do not overlap and therefore the intensities are added and the ID is referred to as a wiggler. When excursions are instead in the order of γ^{-1}, the ID is referred to as an undulator. In this case, the radiation cones overlap and interfere with one another. The field amplitudes are added vectorially, which means that the phase difference from each contribution is included).

5   Experiment

5.1   Sample Preparation

Different NP-samples have been provided by Dr. Christian Rein from DTU. Details on the synthesis of the NPs can be found in reference 39. The NPs were produced using a novel approach to synthesis at room-temperature, so that it could be applied to direct roll-to-roll(R2R)-synthesis. Synthesis of CZTS NPs is often performed at a minimum of 200 °C, to activate monomer precursors and to avoid the formation of secondary phases. Moreover, CZTS NPs can be further improved with annealing under sulfur atmosphere at around 550 °C. These temperatures are however not compatible with R2R substrates, as they melt at temperatures above 120 °C. The NPs produced resulted with narrow size distribution and average size around 6 nm, with copper-poor and Zn-rich compositions (Cu/(Zn + Sn) = 0.8 and Zn/Sn = 1.2 - 1.3). The method allowed also to avoid binary phases formation, such as SnS and Cu_xS. However, the presence of cubic ZnS or Cu_2SnS_3 could not be excluded, due to the similarity of their XRD patterns to that of CZTS-phase. Bandgap for the NPs was derived from UV-Vis reflectance curves for different reaction times. The bandgap was determined to be $\approx$ 1.73-1.83 eV for reaction times between 5 and 25 minutes.

The synthetized NPs were used in ligand exchange reactions to obtain inks with which form different absorber layers by drop casting on Si-doped substrates. Technical details, provided by C.R., of the three samples studied in this thesis, can be found in Table 1. Through Raman spectroscopy, it was possible to find that OLA functionalization promoted the formation of Cu_xS, while thiostannate $(NH_4)_2Sn_2S_6$ samples showed the presence of SnS_2 grains. The 1-dodecanethiol sample resulted in no evident presence of secondary phases.

Table 1: Information about the solution processed samples.

Sample name	Original name	Ligands	Possible Secondary Phases
A	055_WB	1-dodecanethiol	-
B	055_WC	thiostannate complex	SnS_2 grains
C	055_WE	OLA	Cu_xS and OLA

The crystalline sample used to perform RPES analysis, was instead provided by the PhD candidate Mungunshagai Gansukh of the Department of DTU Fotonik. The absorber layer was deposited by sputtering deposition under sulphur atmosphere on a Mo- coated glass substrate. The sample did not undergo any post-annealing treatment.

5.2   Vacuum System

This section is based on selected fragments of reference 40.

Figure 22 shows the simplified system set up present in the laboratory and used for the photoemission analysis. Main components of the system are three chambers: load lock, preparation chamber and main chamber. The first is used to insert the samples and can be quickly vented and pumped down to a medium/high vacuum (up to 1×10^{-8} mbar). The load lock and the preparation chamber can both host thermal evaporators for sample preparations, but none of this equipment was used in this thesis. IPES measurement were performed in the preparation chamber, where also thermal annealing was executed. All the other experiments were conducted in the main chamber, where the highest vacuum is reached (up to 1×10^{-10} mbar).

For PES experiments ultra-high vacuum is required. In order to obtain such conditions in the chambers, a pumping system needs to be developed. **Rotary vane pumps**, or more commonly called roughing pumps, are necessary to establish vacuum at the order of 1×10^{-3} mbar. This type of pumps operate by repeatedly enclosing a gas volume from the chamber and pumping it out through an exhaust outlet. In the current system, one rotary pump is employed for load lock and preparation chamber while another serves the main chamber only. A third rotary pump is connected the helium lamp to perform UPS. Vacuum up to 1×10^{-10} mbar can be obtained by means of **turbomolecular pumps**. This type of pumps can only operate in molecular flow regime, where gas molecule have higher probability of colliding with chamber walls rather than other gas molecules. Molecular flow regime establishes at pressures lower than 1×10^{-3}, while for higher values the gas atoms collide mostly with each other in a typical laminar flow regime. Turbomolecular pumps can not perform in laminar flow and need therefore to be backed up by a roughing pump. Turbomolecular pumps use a quickly rotating turbine with blades that forces gas atoms through a specific direction due to momentum transfer. In system is provided by three turbomolecular pumps, supported by the previously mentioned rotary pumps. **Ion pumps** can be additional to the system. This kind of pumps capture the molecules and do not exhaust the gas. The working principle is that by applying a strong electric field, gas atoms are ionized and accelerated towards electrodes where they are captured. Two ion pumps are present in the system, in the preparation and main chamber. One last type of pump is present in the system, the **titanium sublimation pump**. This pump is placed at the bottom of the main chamber. A titanium filament is excited so that titanium ions are emitted in the chamber. Titanium is a very reactive element and forms solid compounds with different gas atoms, that then collide with the pump's walls, decreasing the pressure of the chamber.

5.2.1   X-ray Photoelectron Spectroscopy (XPS)

XPS in this system is performed using an XR-50 gun from *SPECS* and has two anodes: Mg $K_\alpha 1/2$ and Y $L_\alpha 1$ with photon energies, respectively, of 1253.6 eV and 1922.6 eV. For the purposes of the experiment, only the magnesium anode was used. It is important to state that this source is not monochromated, and it can result in satellite lines due to most importantly Mg $K_\alpha 3$ shifted of 8.4 eV from main line. The working principle of the gun is really simple: high

Figure 22: Schematic diagram of vacuum system in the laboratory used for photoemission analysis. The diagram shows the chambers composing the laboratory system ans the pumps that operate on each section of the line. The most important chambers are the preparation chamber, where thermal annealing and IPES is performed, and the main chamber, where XPS and UPS spectra are measured.

voltage is applied between the cathode/filament and the anode, electrons are emitted from the first and travel towards the anode, colliding at high speed and emitting photons [41].

To perform XPS the gun must be manually moved close to the sample and the titanium sublimation pump turned off. An initial scan over a wide range of binding energy (from 0 to 1200 eV) was recorded, in order to determine the elemental composition of the sample and the presence of contaminants. For wide scans, the pass energy that electrons are required to have in order to pass through the hemispherical electron energy analyzer (HEEA) is kept higher (around 50 eV) as this also sets the energy resolution of the measurements. For narrow scans, the pass energy was lowered to 20 eV to improve resolution. Narrow scans were taken for each element at the core level showing higher intensity on the widescan (specifically S 2p, Sn 3d, Cu 2p and Zn 2p, and 1s for both C and O) in order to perform a quantitative analysis. XPS peak fitting procedure is explained in section 5.3.

It is important to mention that the sample needs to be grounded. In case the sample isn't properly connected to ground, there is the possibility of charging effects: in such a case, the

spectrum could shift at higher binding energies (this is valid also for the other PES techniques). Before the analysis of the samples mentioned in the first part of Chapter 5, other samples were prepared with the same NPs and ligands of Sample A and B, but on a glass substrate coated with Mo. Such samples showed extreme charging effects: for XPS core levels the shifts were around + 30 eV.

5.2.2 Ultraviolet Photoelectron Spectroscopy (UPS)

UPS was performed with a UVS 10/35 UV discharge lamp from *SPECS*. Helium gas is let in in a quartz capillary, where the discharge is ignited: the generated plasma emits UV light at characteristic wavelengths of helium, whose most important are the HeI_α (21.22 eV) and $HeII_\alpha$ (40.82 eV) lines. To connect the UV lamp to the main chamber on a windowless path, there is an evacuating system of two stages differential pumping composed of a rotary and turbo pump. The emitted lines can be selected by adjusting the gas pressure in the discharge capillary. HeI_α line originates from unionized He atoms and the $HeII_\alpha$ from singly ionized ones. When the pressure is lower, electrons from the plasma have longer mean free path and can be therefore accelerated at higher speeds, ionising more gas atoms. For this reason, the $HeII_\alpha$ fraction increases as pressure lowers. For the experiment, only HeI_α line was used. The spectrum was obtained by running a series of scans ranging over the energies 0 - 12 eV.

5.2.3 Inverse Photoelectron Spectroscopy (IPES)

IPES in isochromat mode was performed with a *PSP Vacuum Technology*. The source is designed to produce an electron beam from a heated barium oxide BaO cathode, which emits at approximately 1100 K to 1200 K. The source has a low energy spread of approx 0.25 eV (FWHM) in the range 5 to 50 eV beam energy [42]. The IPES detector is a bandpass detector designed to detect photons of approximately 9.5 ± 0.5 eV energy. The detector includes a SrF_2 window prior to a Ta cone coated with NaCl. Behind the Ta cone, an electron multiplier is placed. The SrF_2 window acts as a low pass filter as it only allows low energy photons to pass through (below 10 eV). Such photons will produce photoelectrons from the surface of the Ta: only the high energy photons will produce photoelectrons (the coating then acts as a high pass filter). The electron multiplier, or channeltron, amplifies electrons produced on the photocatode [42].

5.3 Data Analysis

5.3.1 XPS spectrum peak fitting

Peak fitting is an significant part of XPS data analysis. Chemical shifts already provide indispensable knowledge about the elemental composition of the sample, but only by fitting the spectrum it is possible to calculate the relative abundance of the elements and of the phases in

which they are present.

The energy distribution spectrum in PES is characterized by spectral functions, which take in account all the possible excitation processes happening in the sample of interest. In most of the cases, these spectral functions can be represented by a set of peaks. Typically, peak shapes are modelled mathematically by a convolution of independent Lorentzian and Gaussian functions, giving the so-called Voigt profile [43]. The Lorentzian contribution is due to the limited lifetime of the core hole state, while the Gaussian broadening is mostly due to line shape of the exciting X rays from and X-ray spectromter, and may also be related to thermal excitation processes. Chemical, structural and electronic (by dopants) inhomogeneities in the surrounding of the emitting atoms often also contribute to the Gaussian broadening [44].

The mathematical generation of a Voigt profile is generally time consuming, therefore approximations have been employed in XPS spectra fitting. A comparative study has shown the potentiality of product and sum of Gaussian and Lorentzian functions as an alternative to the convolution, where it was found that the sum function is superior to the product, particularly in low-noise spectra [44]. For the sake of this thesis project, the intensity profile I of the XPS spectrum has been approximated by the sum of Gaussian and Lorenzian functions (whose mixing ratio is defined by M_h), as shown in Equation 12:

$$I(x, h, \mu, \sigma, M_h) = M_h \frac{h}{\sigma\sqrt{2\pi}} \exp[-\frac{1}{2}(\frac{x-\mu}{\sigma})^2] + (1 - M_h)\frac{h}{\pi}\frac{\frac{1}{2}\sigma}{(x-\mu)^2 + (\frac{1}{2}\sigma)^2} \tag{12}$$

In Equation 12, Guassian and Lorentzian are expressed in their normalized form, meaning that the integral of Equation 13 and 14 equals 1, multiplied by the factor h. The parameters μ and σ refer to the center of the symmetric functions and the width respectively.

$$G(x, h, \mu, \sigma) = \frac{h}{\sigma\sqrt{2\pi}} \exp[-\frac{1}{2}(\frac{x-\mu}{\sigma})^2] \tag{13}$$

$$L(x, h, \mu, \sigma) = \frac{h}{\pi}\frac{\frac{1}{2}\sigma}{(x-\mu)^2 + (\frac{1}{2}\sigma)^2} \tag{14}$$

$$\int_{-\infty}^{+\infty} L(x)dx = h \tag{15}$$

The shape of a photoelectron line carries a great quantity of information but unfortunately, such lines are superimposed on a rather high and strongly structured background. It becomes necessary to remove the assumed contribution due to inelastic scattering from the spectrum to obtain a background-free line shape. The background main contribution can be attributed to energy loss processes, distinguished between extrinsic (occurring away from the emitting atomic center, through the response of the loosely bound electrons to the probing electron itself) and intrinsic (occurring in the close vicinity of the emitting atomic center, through the

response of the core hole of the photoemission process) [45]. The first method putting the background into relation with the measured spectra was suggested by Shirley (details about theory and practical applications can be found in reference 46). Several background determination techniques have been developed for handling XPS spectra and became popular for being very easy to implement: this type of technique does not require any preliminary knowledge of the peak shape and the correction can be carried our before the fitting procedure. However, this approach causes systematic errors in the following spectrum determination. In this thesis, a different approach described in reference 47 has been considered: this method allows to fit the background simultaneously with the photopeaks, to get a more accurate peak area and position determination. In details, the background has been modelled by the sum of linear functions and error functions. The error functions have been defined so that each center of symmetry corresponds to the center of one Voigt function. The parameters a and b in Equation 16 define the amplitude and the slope at $x = \mu$ of the error function respectively.

$$f(x, \mu, a, b) = a\frac{\exp((x - \mu)b)}{1 + \exp((x - \mu)b)} \tag{16}$$

The analysis of XPS spectra is performed comparing experimentally recorded spectral intensity distribution with a theoretical model curve. The set of peak model parameters $\vec{p}$ (h, μ, σ, M_h, a, b, and slope coefficient of the linear function), are determined iteratively by a non-linear parameter estimation routine, with the goal of minimizing the reduced chi-square χ^{2*} parameter, defined in the Marquardt-Levenberg algorithm [44] as

$$\chi^{2*}(\vec{p}) = \frac{1}{N - P}\sum_{i=1}^{N}\frac{[M(i) - S(i, \vec{p})]^2}{M(i)} \tag{17}$$

where $M(i)$ represents the measured spectrum recorded at N energy values corresponding to channel i, $S(i, \vec{p})$ the model curve and P the independent parameters of the model function. The normalized residuals $R(i)$ are included in the presentation of the data together with the optimized model curve $S(i, \vec{p})$, as it will be possible to see in Chapter 6:

$$R(i) = \frac{S(i, \vec{p}) - M(i)}{\sqrt{M(i)}} \tag{18}$$

For the purpose of this work, the fitting model has been created using the software Excel.

5.3.2   Elemental Ratio

From the XPS fitting, the ratio of elements present in the sample can be calculated and differentiated between the different phases in which the element is present. The measured data are given in number of photoelectrons detected, "counts", over scanned binding energy E_B. The counts are a direct measure related to the intensity of the signal, and have been normalized over the number of scan performed to collect the spectrum. Assuming an homogeneous volume

from which the signal generates, the number of photoelectrons I_i produced by the core levels of the element i can be described by the following equation:

$$I_i \propto q_i \sigma_i \tag{19}$$

where q_i is the quantity of the specific element i and σ_i the photoionization cross-section of the element i at the energy of the X-ray source. Values for the cross-sections σ for the detected elements can be found in reference 48, "Atomic Calculation of Photoionization Cross-Sections and Asymmetry Parameters", while peak positions for typical compounds can be found in 49 and 50.

5.4 Resonance Spectroscopy (RPES)

5.4.1 ASTRID2 and MATline

The RPES experiments on a CZTS crystalline sample were carried out at the ASTRID2 synchrothron at ISA, Aarhus University, using the MATline beamline.

The storage ring ASTRID2 with a circumference of 45.7 m and it is placed next to ASTRID, the older synchrothron, that is used as booster for the newer facility. ASTRID2 has a hexagonal structure with 4 straight sections for magnetic insertion devices. There are currently four beamlines from insertion devices on ASTRID2 together with three beamlines from bending magnets. ASTRID2 operates at 580 MeV and is optimised for photon energies from the visible to around 1 keV. ASTRID is used as an injector for ASTRID2, accelerating 100 MeV electron beams from the microtron pre-injector, to 580 MeV, to allow full energy top-up of ASTRID2. The system generates the radiation thanks to a multipole wiggler. For further details on ASTRID2, its parameters and its structure, it is suggested to follow reference 51.

The MATline is specifically used for material science and surface physics purposes, as it is characterized by an UHV environment to perform surface science techniques. The main components of the line systems are a Scienta electron energy analyser and a SX-700 monochromator [52]. Such monochromator system operates plane grating optics and allows to perform experiments with photon energies ranging from 40 eV to 700 eV.

5.4.2 Beamtime data analysis

For the purposes of the experiment, on the crystalline sample was also performed XPS to control composition and impurities of the sample. The sample was mounted on a tantalum conductive sample holder, placed in vertical position. Therefore, two tantalum wires clipped the sample on the sides to keep it in position during the measurements. For the widescan, the photon energy was set at 620 eV, pass energy at 60 eV, and the binding energy scanned from 0 to 570

eV. Narrow scans were also performed at pass energy of 20 eV. The detected core levels were recorded at different photon energies: as the monochromator crystal can be aligned so that only a specific energy of the sychrothron radiation can be selected as probe, for each element the photon energy at which the cross section for the specific core level resulted the highest was taken to perform the narrow scan. The detected core levels resulted to be O 1s, Sn 3d, C 1s, S 2p, Cu 3p and Zn 3p. All data sets were normalized by number of scans and by beam current: due to the necessity of topping up the current in the ring, the beam current oscillates and its value can be recorded simultaneously with the emitted electrons count. The beam current value was around 181 ± 2 mA in all the measurements. For the fitting of the spectra, the procedure explained in Chapter 5.3 has been followed.

The collection of RPES measurements was the main activity at the MATline. Before the analysis, the sample was sputtered with Ar at 500 eV for 10 minutes, followed by no annealing. In order to visualize the resonance behavior in the VB region, the VB (from -1 to 12 eV) was collected for photon energies ranging from 40 to 200 eV, with a step of 0.5 eV. The data have been normalized to take in consideration the variation of photon flux as photon energy increases, following this procedure:
- Given i the photon energy and j the binding energy E_B in a VB scan, the measurement at a specific E_B j for a specific photon energy i is defined $M(i,j)$;
- Per each photon energy j, all the counts in a VB scan were added in a unique number, defined $S(j)$:

$$S(j) = \sum_{i=-1}^{i=12} M(i,j) \tag{20}$$

-Each $M_{(i,j)}$ is then divided by the corresponding $S(j)$.

By using this method for the normalization, for every VB scan the total sum of the intensities adds up to 1. This method was used in order to remove the effect of the photon flux and increased signal with increase of photon energy. The normalized data were plotted in a 2D image and 3D diagram to visualize resonance effects.

6   Results and Discussion

In this section, the main experimental results will be presented and discussed. The results regarding the crystalline sample will be presented first, as its characteristics can be used as reference for the solution processed thin films. These last ones will be compared in their electronic structure and composition further in the chapter.

6.1   Crystalline sample - RPES analysis

The crystalline sample was prepared with the goal of analysing the VB of CZTS and using it as a benchmark for the experiments on the dropcasted samples. Nevertheless, prior composition characterization was performed, and here reported. It is important to notice that the glass substrate made the analysis extremely challenging, due to charging effects. The glass insulates the absorber layer from the tantalum sample holder. Good results have been obtained supposedly thanks to the front clipping tantalum wires. For next experiments, it is suggested to prepare CZTS crystalline absorber layer on conductive substrates.
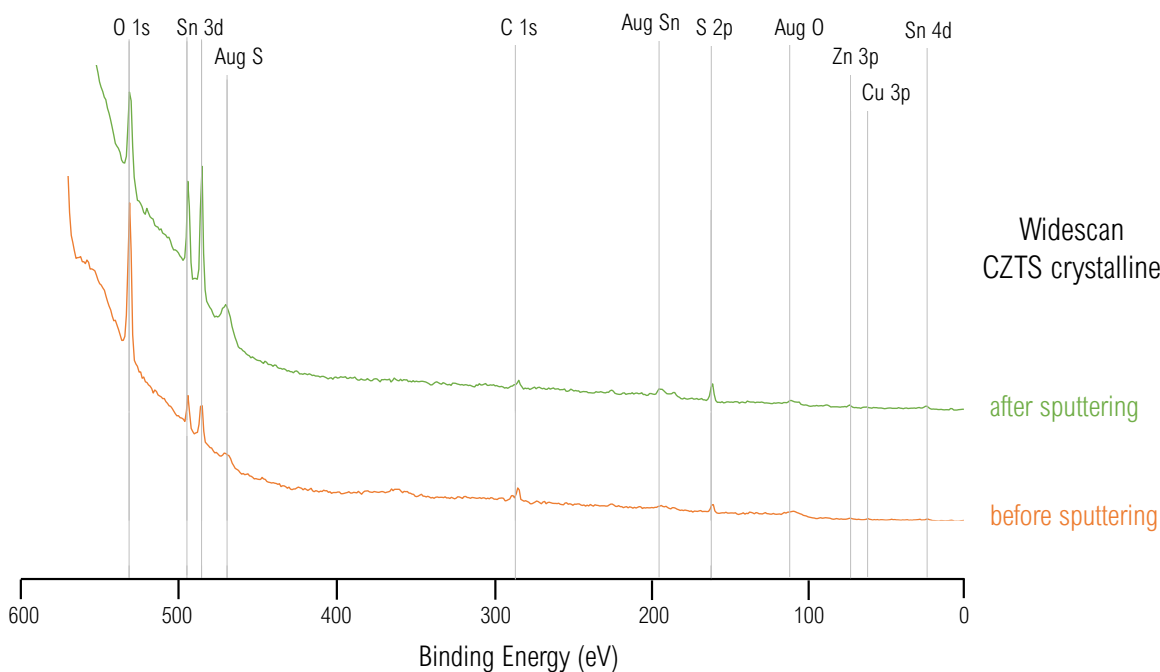
6.1.1   Elemental composition

Figure 23: XPS widescan measured on the CZTS crystalline sample, before and after the sputtering procedure for the removal of the surface impurities. The spectra have been shifted upwards for clarity.

Figure 23 shows the XPS widescan of the crystalline sample, before and after the sputtering

procedure, performed to remove surface contaminants. A decrease in the intensity of the O 1s and C 1s peaks is clearly visible, together with an increase in the signal for Sn 3d and S 2p. The core levels for S, Cu and Zn are highlighted on the widescan, but are however very small compared to the high intensity ones like O 1s and Sn 3d.

Narrow XPS scans of the O 1s, Sn 3d, C 1s, S 2p, Zn 3p, and Cu 3p core levels were performed. The fitting analysis has shown very high percentage of oxygen and carbon on the crystal surface, compared to the quantity recorded for the CZTS elements, suggesting that the sputtering process was not very effective. Longer sputtering times are suggested for future work on similar samples. The high-resolution XPS spectra after background subtraction for S, Sn, Cu and Zn are shown in Figure 24. The Sn $3d^{5/2}$, Zn 3p, and Cu 3p peaks can be easily fitted by a single Voigt function, therefore associated to the kesterite phase. The S 2p profile appears peculiar, with the contribution of at least 3 phases. Comparing the peak energies to literature [50] [53] [54], the main peak (species A) can be attributed to the CZTS phase, while the two smaller peaks at around 166.7 and 169.2 eV seem to be related to sulfoxide and sulfate phases respectively. It is important to remind that selenium might be present on the sample as impurity. Such statement derives from analysis on the RPES data that will be shown later on. Selenium contamination in the analysis chamber has been confirmed by the MATline staff, as produced in previously performed experiments. Selenium signal might have not been detected due to the overlap of Se 3p core level with S 2p. Moreover, Se might have been also present as an impurity in the crystal structure from the synthesis process: Se could easily substitute S atoms in the CZTS structure, forming the sulfur-selenium alloy CZTSSe. In such a case however, a chemical shift in the core levels of Cu, Zn and Sn should also be visible. Table 2 shows an overview of the fitting results over the crystalline CZTS sample. Sulfur coming from the CZTS phase emerges as the most present element at the surface of the sample. High percentage of Sn is also detected. In contrast with the optimal Cu/(Zn+Sn) = 0.8 and Zn/Sn = 1.25 for bulk crystalline CZTS samples (see Chapter 2), on the surface of this sample the same ratios give values Cu/(Zn+Sn) = 0.49 ± 0.01 and Zn/Sn = 0.14 ± 0.01. It seems important to recall that the sample underwent sputtering procedure. Such practice might have altered the surface conformation of the sample, allowing different crystalline layers to be detected without maintaining the true elemental composition ratio. Therefore, it is not easy to determine the reason for the high presence of Sn at the surface compared to Cu or Zn. Very interesting are also the highly abundance of sulfoxide and sulfate phases on the surface. It is not known whether such phases were present before the sputtering procedure, or if they formed on the surface after sputtering and post-annealing processes. Sulphur evaporation could have occurred at the post-annealing temperature (200 °C), and the atoms reacted with oxygen and carbon impurities at the surface.
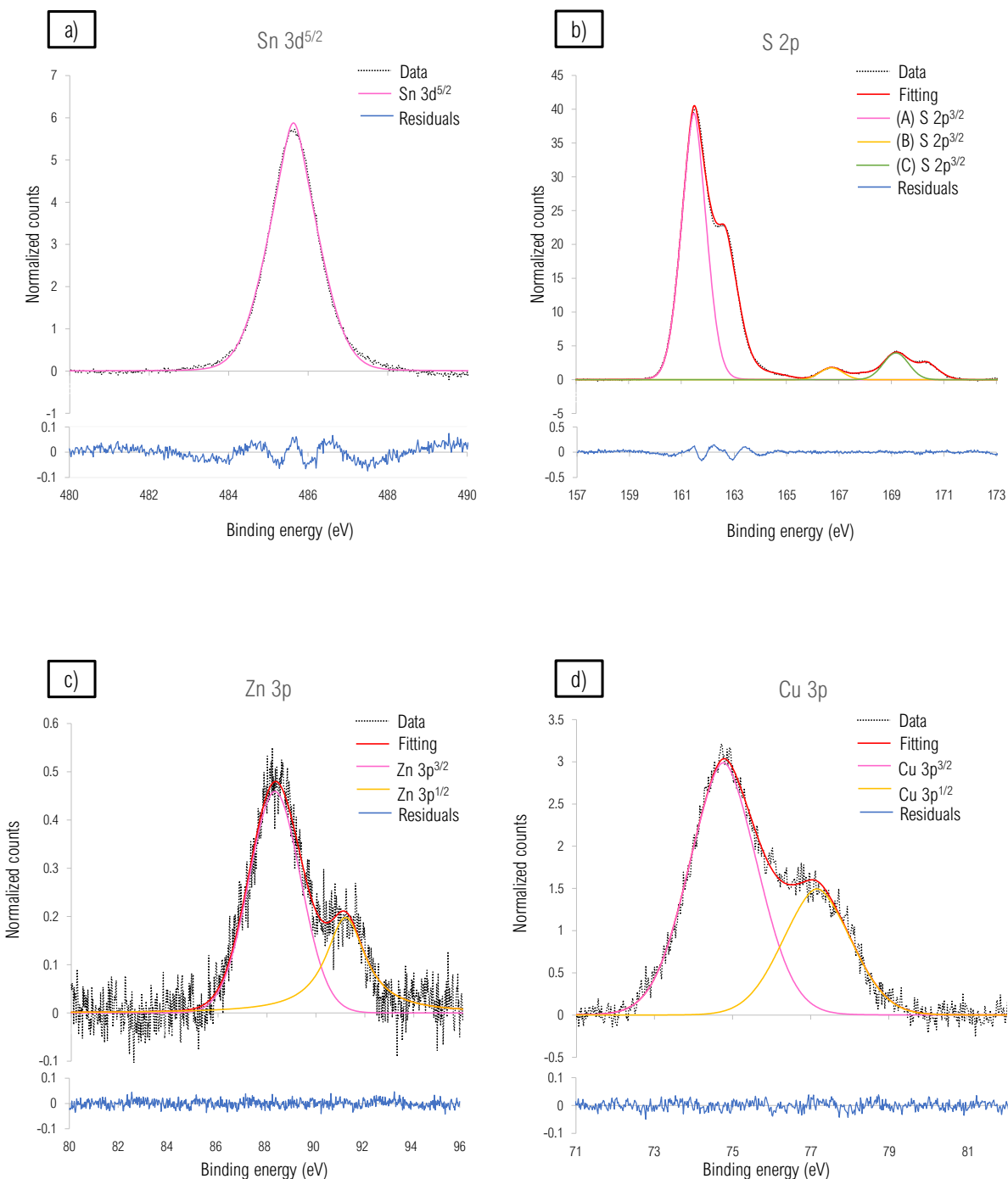
Figure 24: Narrow XPS scans in the case of crystalline CZTS, for the core levels a) Sn $3d^{5/2}$, b) S 2p, c) Zn 3p and d) Cu 3p. The raw data (black lines) are compared with the fitting curve (red lines). For each core level, the different contributions to the fitting model are shown. Sn, Zn and Cu spectra can be described by one species contribution. The S 2p spectrum shows the presence of 3 chemical bonds: species A at around 161.5 is considered to be relative to the CZTS phase, species B relative to sulfoxide species, and species C to sulfate phase. Residuals for Sn and S show an imprecise fit of the peaks: this might arise from a possible asymmetry of the peak or a wrong estimation of the Lorentzian to Gaussian ratio in the Voigt profile.

Table 2: Overview of the fitting results of the detected phases for the crystalline CZTS sample. The error on the peak energies resulted to be < 0.01 eV for all the peaks, and < 0.03 % on the relative abundance values.

Element	Phase	Orbital	Energy (eV)	Relative abundance (%)
Sn	CZTS	$3d^{5/2}$	485.6	10.6
		$3d^{3/2}$	494.2	
S	CZTS	$2p^{3/2}$	161.5	70.3
		$2p^{1/2}$	162.7	
	sulfoxide	$2p^{3/2}$	166.7	8.2
		$2p^{1/2}$	167.9	
	sulfate	$2p^{3/2}$	169.2	3.4
		$2p^{1/2}$	170.4	
Zn	CZTS	$3p^{3/2}$	88.3	1.5
		$3p^{1/2}$	91.2	
Cu	CZTS	$3p^{3/2}$	74.7	6.0
		$3p^{1/2}$	77.2	

6.1.2 RPES results

Figure 25 (a) shows the 2D representation of the RPES analysis results. The intensity of the detected signal (maximum intensity - yellow, minimum intensity - black) is plotted as a function of photon energy, recorded for values ranging from 40 to 200 eV, and binding energy, scanned from -1 to 12 eV. Figure 25 (b) displays schematically the key features obtainable from the RPES 2D plot.

The features have been numbered from 1 to 7, and will be further exploited:

1. The black line represent the VB maximum dependency with photon energy. A closer look to the feature is shown in Figure 26. It is possible to notice how this value shifts toward smaller energies, finding its maximum in correspondence of the resonance feature attributed to the transition from S 2p to a not-fully-occupied outer hybridized orbital (red line). For energies below 162 eV, the VB maximum shifts from around 2.5 eV (photon energy = 40 eV) to 1.2 eV (photon energy around 162 eV). At VB maximum line assumes a vertical edge for photon energies above 162 eV: this feature implies the contribution to the S 2p transition on the VB maximum, as for photon energies below 162 eV the transition is not able to happen. There is however another shoulder in the VB maximum line, approximately happening in correspondence of the photon energy that allows the excitation of Cu 3p electron (see Number 2).

2. This first high-intensity peak at binding energy around 2.7 eV is attributed to the transition of Cu 3p electrons to an hybridized valence orbital. Considering pure Cu, its electronic configuration, $4s^1 3d^{10}$, is described by having a fully occupied 3d state, and
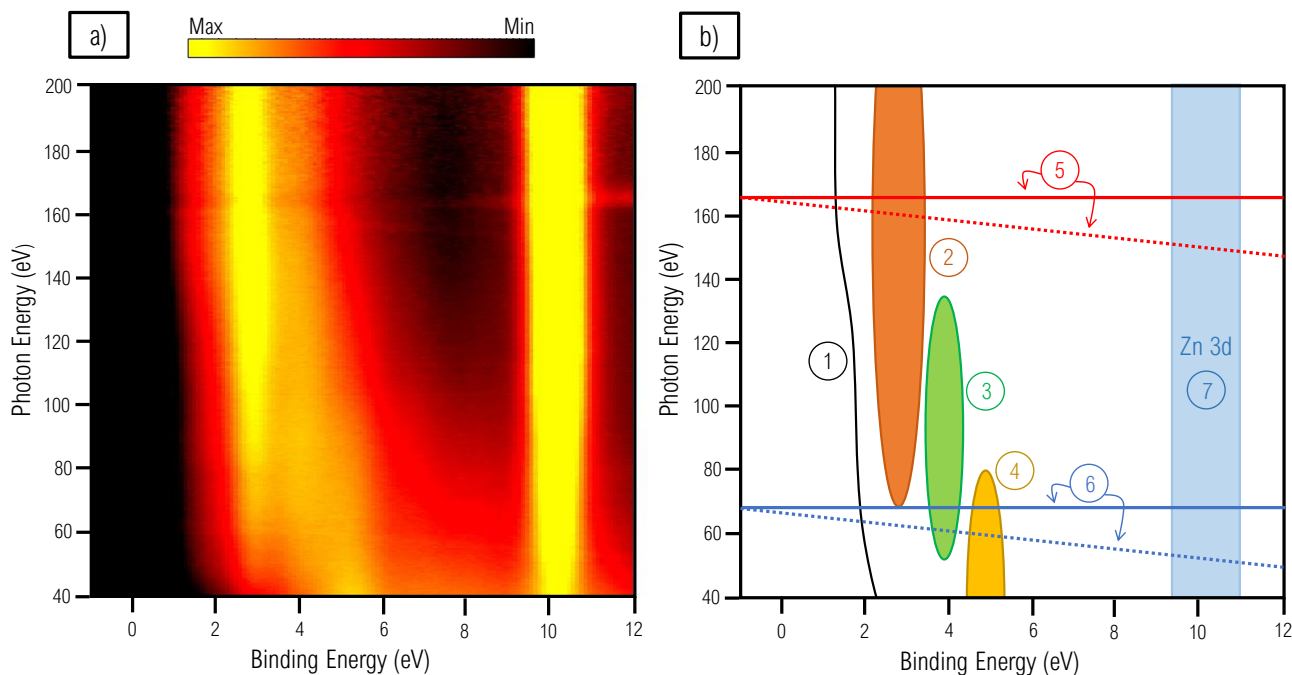
Figure 25: (a) 2D plot of RPES results on a CZTS crystalline sample. The intensity (max - yellow, min - black) is given as function of photon and binding energy (eV); (b) schematic representation of key features present in the RPES 2D plot: 1) VB maximum, 2) resonance due to transition Cu 3p → 4s, 3) unknown resonance, probably given by Se impurity present in the vacuum chamber, 4) supposedly, this resonance peak corresponds to transition to the O 2p orbital, 5) the bold line corresponds to a data-normalization effect due to the resonance of the transition from the S 2p orbital, while the dashed line results from resonance from second order radiation, 6) same effects considered in the previous feature, but due to resonance from transition Cu 3p → 4s (this effect is not very visible from this figure, but its presence was determined at higher magnification), 7) Zn 3d core level.

half filled 4s orbital. RPES analysis on transition metals have shown the impossibility of the transition of 3p electrons of copper to 3d orbital, due to the complete filling of the latter [55], while 3p to 4s transition should be allowed at energy around 73 eV. However, in the case of a composite material like CZTS, it is believed that the valence band of the material is formed by the unoccupied orbitals of Cu hybridized with the S 3p level [13]. The energy of the transition from Cu 3p to the hybridized orbital can therefore change from 73 eV. From the experiment, such transition seems to be allowed for energies above 64 eV (blue line).

3. In the 2D plot it is possible to see other two less intense peaks at binding energy around 4.1 eV (**3**) and 5.3 eV (**4**). The first starts to appear for energies slightly above 50 eV. The origin of this feature is unknown. From the XPS widescan spectrum, no other transition metal impurities that could be responsible for such peak were detected. One possible
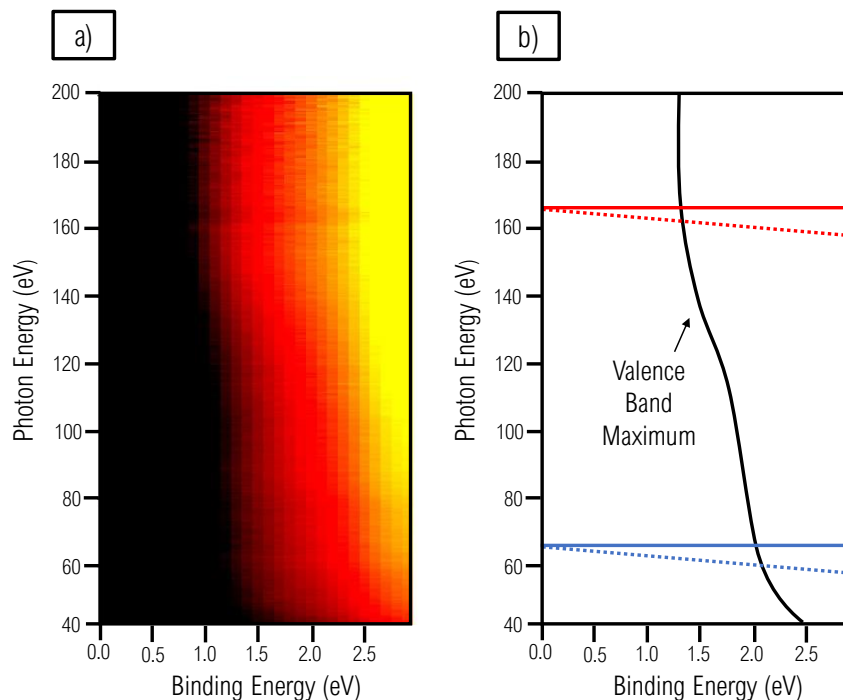
Figure 26: (a) 2D plot of RPES results on a CZTS crystalline sample - close look at the VB maximum edge; (b) Schematic representation of the key features of the 2D plot: the VB maximum line shows two elbow at resonance energies corresponding for the transition from the Cu 3p shell (blue line) and from the S 2p shell (red line). The dashed lines highlight RPES effects due to second order light in the synchrotron radiation.

cause of the feature could be addressed to the selenium contamination, as the Se 3d orbital corresponds to energies around 53 eV.

4. The feature **4** was attributed to O 2p valence states. It is not possible to define from which photon energy the feature develops (due to technical limits of the beamline), as from the data it is only possible to see its decay. However, it seems reasonable to associate the feature to the O 2s to 2p transition (O 2p core level corresponds to energies around 22 eV for different transition metal oxides). Such feature confirmed the presence of oxygen in the crystal structure. To help the visualization of how the peaks **2**, **3** and **4** appear and fade out at different energies, the normalized VB spectra for photon energies 40 eV, 70 eV, 100 eV and 180 eV are compared in Figure 27.

5. The bold red line in feature **5** can be addressed as an artifact resulting from the normalization of the RPES data, explained in Chapter 5.4.2. Such normalization was necessary in order to cancel out the effect of the increasing photon flux, causing the recorded signal to monotonically increase. In correspondence of feature **5** in the RPES data plot, it is possible to see a shrinkage at the Cu peak and an enlargement at the Zn peak. The reason
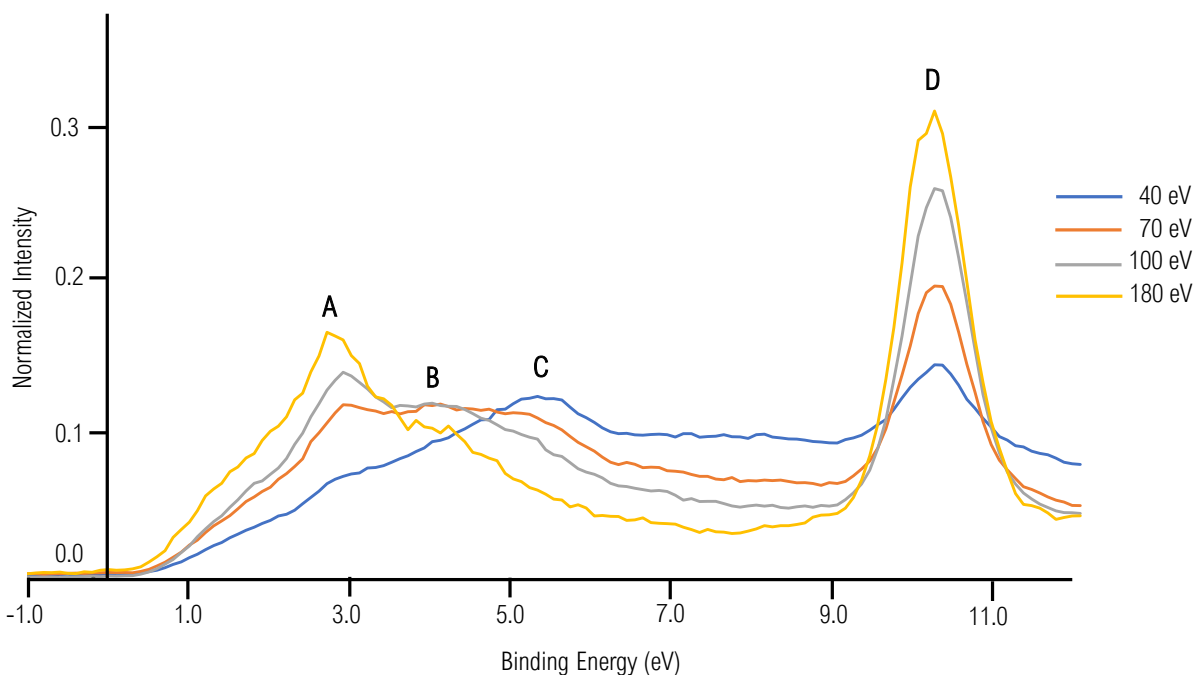
Figure 27: Comparison of normalized VB spectra recorded for the photon energy 40, 70, 100 and 180 eV. Four peaks are highlighted by the letters A-D. Peak A is considered to be result of the electrons excited from the Cu 3p level: Such peak is absent in VB spectra recorded at photon energies below the transition energy (around 64 eV), while becomes more dominant as photon energy increases. Peak B is supposed to be result of Se contamination. Its contribution in the VB spectrum is visible starting from energies slightly above 50 eV, but as photon energy increases, peak A becomes dominant. Peak C is caused by excited electron from O 2s orbital to O 2p. As photon energy increases, the cross section of O 2p monotonically decreases and the peak fades out. Peak D corresponds to Zn 3d core level: the cross section of Zn 3d in the photon energy range 40-200 eV does not change consistently as it is maintained in the order of 1×10^1, and the relative increase of the peak is due to the normalization method.

why this effect is generated can be visualized with the aid of Figure 28. The normalization forces the area under the recorded spectrum for each photon energy to be equal to 1. Therefore, in the case of an abrupt increase in the Zn signal, the normalization drags the lower-intensity features to even smaller values to compensate for the high-intensity peak. The dashed red line indicates a series of small additional peaks considered to generate from second order synchrotron radiation. It is well known that monochromators often allow the passage of higher-order radiation, meaning that if the selected photon energy equals $h\nu$, radiation with energy $2h\nu$ will also be present but with much lower intensity. Figure 29 shows the effect of second-order radiation on an XPS spectra. When the photons carry energy $h\nu$ just at the core level energy S 2p (around 162 eV - blue line), the excitation is allowed. The electrons excited from the first-order beam will have energy $E_{kin} = h\nu - E_B(\text{S 2p}) = 162 - 162 = 0$ eV. In the XPS spectra it is possible to see the S 2p

core level at binding energy 162 eV (purposely out of proportion in Figure 29). Moreover, a second-order radiation with energy $2h\nu = 320$ eV excites electrons from the S 2p core level. Such electrons will be ejected with $E_{kin} = 2h\nu - E_B(\text{S 2p}) = 324 - 162 = 162$ eV. However, the analyzer records only the kinetic energy and does not possess any information on the actual energy of the incoming photon. The analysis system only knows the photon energy requested to the monochromator, so the second-order peak appears at the Fermi level, as $E_B = h\nu - E_{kin} = 162 - 162 = 0$ eV. In Figure 29, the green line represents the case of $h\nu = 142$ eV. When the photon energy is below the transition energy, no S 2p electrons are excited by the first order light (S 2p peak missing). However, the second-order radiation has enough energy to allow the excitation, as $2h\nu = 284$ eV. The electrons will be emitted with $E_{kin} = 2h\nu - E_B(\text{S 2p}) = 284 - 162 = 122$ eV, and recorded on the spectrum at binding energy corresponding to $E_B = h\nu - E_{kin} = 142 - 122 = 20$ eV. The second-order generated peak shifts of 1 eV towards the Fermi level as photon energy is increased of 1 eV, coinciding with E_f when $h\nu$ equals the core level energy. This explanation justifies the appearance of the feature identified by the dashed red line: the line was found to have slope of about -1, expected for second-order light excitation.
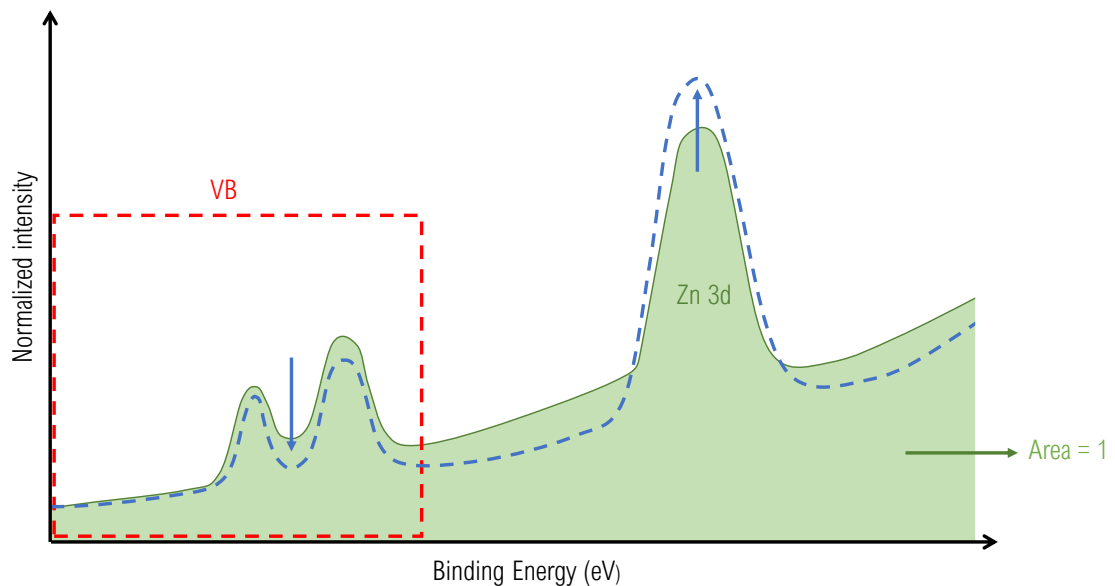

Figure 28: Effect due to data normalization. In order to limit the effects of increasing photon flux and therefore higher recorded signal, a normalization over the RPES data was performed such that the area underneath the spectrum was forced to be 1. However, in the case of an abrupt increase in the higher-intensity features, like the peak Zn 3d, smaller features would be further decreased for compensation.
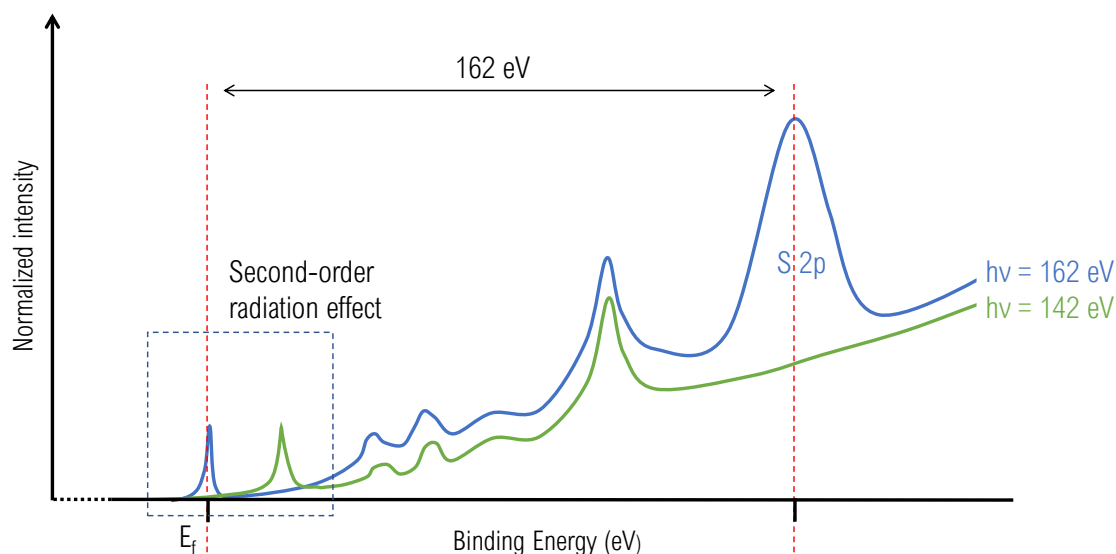
Figure 29: Schematic representation of the appearance on the XPS spectra of second-order radiation light generated effects. When the photon energy of the incoming radiation $h\nu$ equals the energy at which the S 2p electrons are excited (blue line), the second-order light with energy $2h\nu = 324$ eV excites S 2p electrons to $E_{kin} = 162$ eV, which are detected at the Fermi level ($E_B = h\nu - E_{kin} = 162 - 162 = 0$ eV). When the photon energy is below the S 2p transition (green line), such excitation is not allowed (peak disappears), but the second-order light has enough energy to excite some electrons from the S 2p core level. In the case of $h\nu = 142$ eV, the second-order light excited electrons will have $E_{kin} = 284 - 162 = 122$ eV and detected at $E_B = h\nu - E_{kin} = 142 - 122 = 20$ eV.

6. The feature **6** on the RPES data plot can be described in the same way as the feature **5**, but it is result of the excitation of electrons from the Cu 3p core level.

7. The most intense peak in the RPES data plot is defined by the feature **7**, and represents the Zn 3d core level.

In conclusion, the RPES analysis helped in the understanding of the different contributions at the edge of the VB. The states at the VB seem to be related to the transitions from Cu 3p and S 2p. Such deduction can be justified by the appearance of a bright peak at around 2.7 eV, that develops when the sample is excited with photon energies around the Cu 3p transition, and by the VB maximum moving from 2.5 eV to 1.2 eV in correspondence with the S 2p transition at 162 eV. The VB maximum line presents two "elbows", occurring at the Cu 3p and S 2p transition energies: supposedly, when exciting the sample with photon energies between 73 and 162 eV, Cu is responsible for the VB maximum state, while for photon energies above 162

eV, S excites to new energy states closer to the Fermi level. The resonant behavior of Cu 3p and S 2p transitions is also accompanied by the presence of smaller additional peaks due to resonance from second order radiation. Such peaks generate a visible feature on the RPES 2D plot, highlighted by dashed lines in Figure 25. Such lines appear with a slope of -1 in the photon energy vs. binding energy plot, justified by the theoretical behavior of the second-order excitation.

6.2   Solution processed samples - PES analysis

The solution processed samples were studied to understand the ligands dependency over the band gap of the CZTS absorber layer. From previous experiments conducted by Dr Christian Rein, several ligands resulted to effectively coordinate with CZTS NPs in different solution environments. Interest of this thesis project was understanding and comparing the coordination effects on the NPs bandgap of three ligands: oleylamine (OLA), characterized by long carbon chains and generally referred as "native ligand" as used in synthesis procedures, used in sample C, was confronted with the performance of 1-dodecanethiol (S^{2-}) and thiostannate complex ($Sn_2S_6{}^{4-}$) in samples A and B respectively. For such analysis, the samples composition was investigated through XPS, and the results can be found in Chapter 6.2.1. XPS results were not only effective in providing information on the composition, but also in giving a relative scale of the surface ligands to the electron mean free path. The VB and CB were estimated through combined UPS and IPES results. Thermal treatment was applied to the samples in order to test the effects of ligands evaporation on the band gap. The results of the study on the energy band gap of the three sample can be found in Chapter 6.2.2.

6.2.1   Elemental composition

Out of all the drop-casted samples, sample A (S^{2-} ligands) is the only one that was analyzed at the MATline, while the study on sample B ($Sn_2S_6{}^{4-}$ ligands) and sample C (OLA-capped) was performed at the facilities of NTNU. The obtained results over the composition will be reported separately for each sample.

Sample A - S^{2-} ligands
The widescans for before and after the thermal treatment are shown in Figure 30. Some features that can be observed include the presence of silicon signal from the substrate, implicating the poor coverage of the wafer by the NPs film, and the reduction of C signal opposed to the increase of O, Sn and Cu signal after the thermal treatment. The increase of O signal can indicate O as a structural element and not as an impurity like C. Moreover, no signal from Zn is detected, neither before nor after the annealing process.
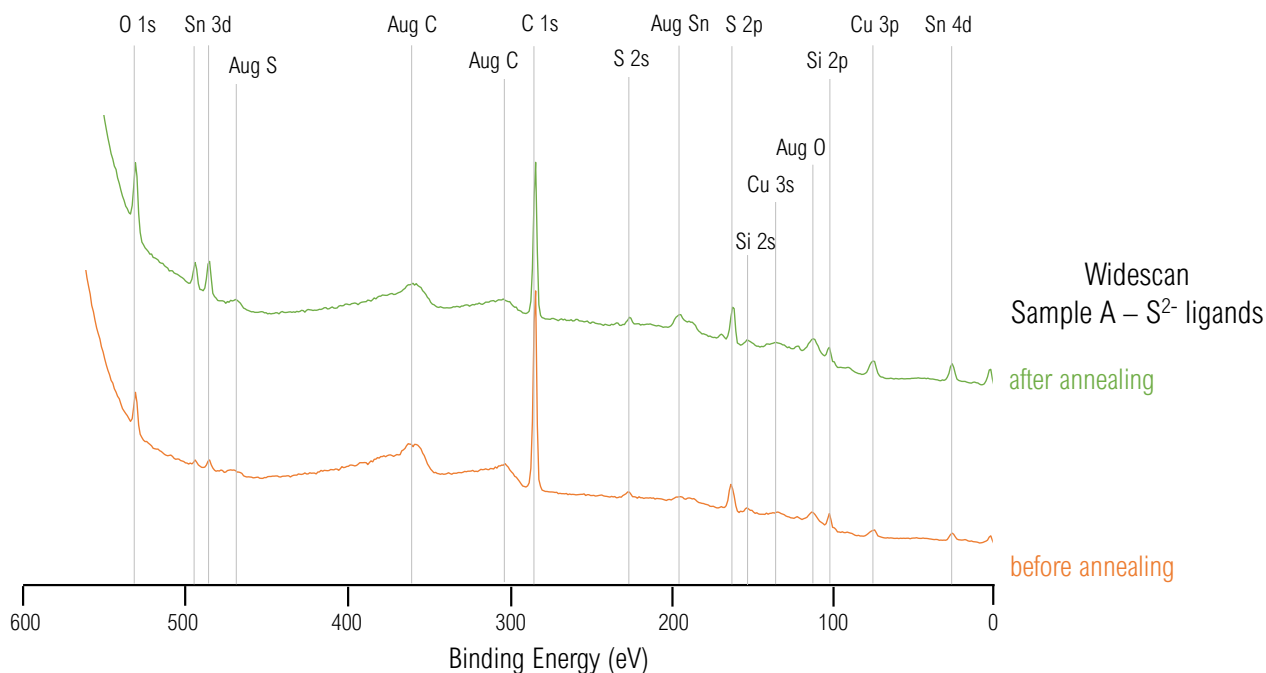
Figure 30: XPS widescan measured on the CZTS drop-casted sample A (S^{2-} ligands), before and after the annealing treatment. The spectra have been shifted upwards for clarity.

Table 3: Overview of the fitting results of the detected phases for the drop-casted sample A (S^{2-} ligands).The error on the peak energies resulted to be < 0.01 eV for all the peaks, and < 0.005 % on the relative abundance values.

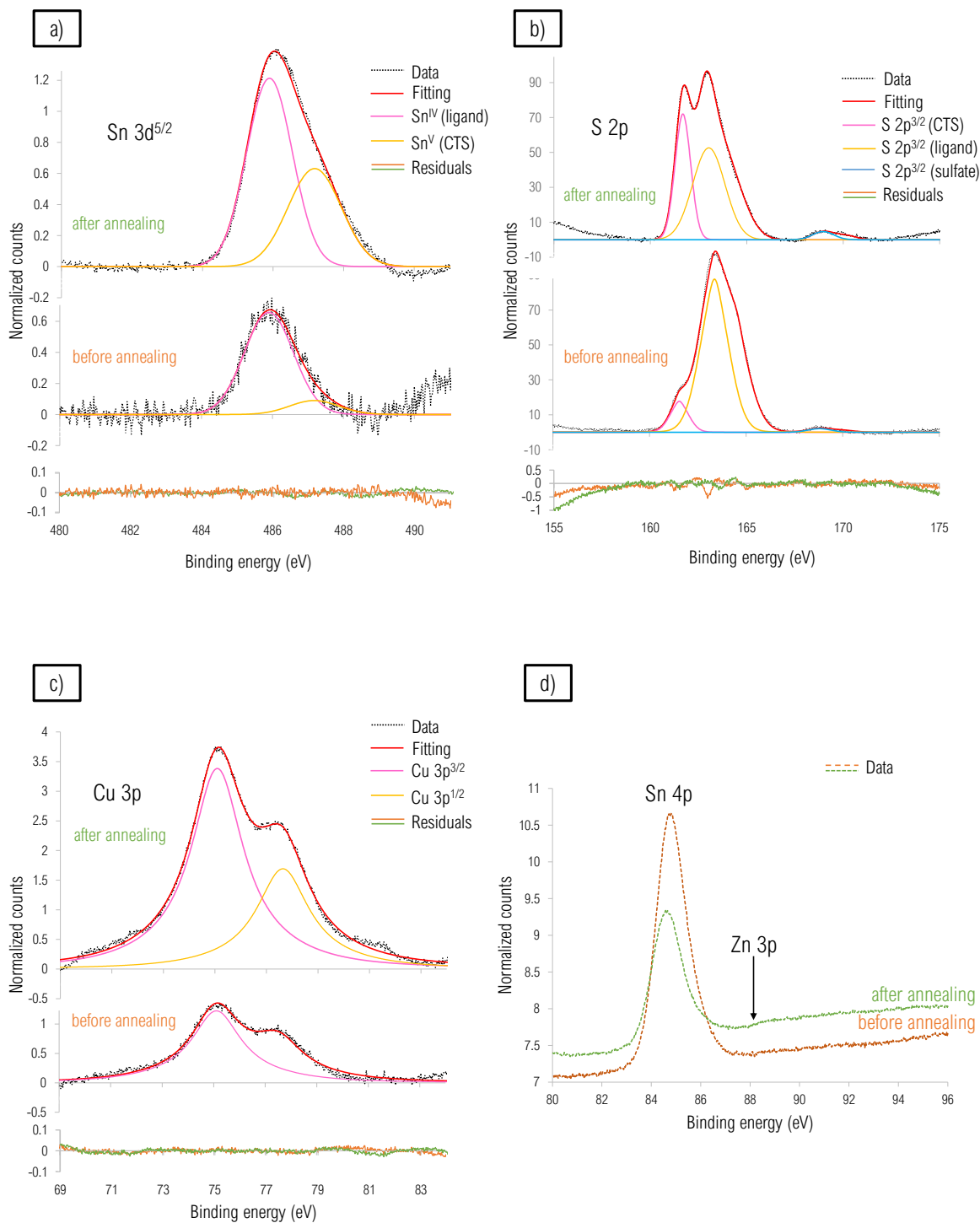| Element	Phase	Orbital	Energy (eV)	Relative abundance (%)	
				before annealing	after annealing
Sn	IV (ligands-bond)	$3d^{5/2}$	485.9	0.03	0.06
		$3d^{3/2}$	494.5		
	V (CTS)	$3d^{5/2}$	487.2	0.01	0.04
		$3d^{3/2}$	495.8		
S	CTS	$2p^{3/2}$	161.6	11.3	38.53
		$2p^{1/2}$	162.8		
	ligands	$2p^{3/2}$	166.4	86.7	57.68
		$2p^{1/2}$	167.6		
	sulfate	$2p^{3/2}$	168.8	1.67	3.36
		$2p^{1/2}$	170.0		
Cu	CTS	$3p^{3/2}$	75.1	0.11	0.33
		$3p^{1/2}$	77.5		

Figure 31: Narrow XPS scans for the solution processed Sample A (S^{2-} ligands), for the core levels a) Sn $3d^{5/2}$, b) S 2p, e) Cu 3p and d) Zn 3p. The raw data (black lines) are compared with the fitting curve (red lines), and the before- and after-annealing conditions are confronted. For each core level, the different contributions to the fitting model are shown.

Figure 31 shows the high-resolution XPS spectra after background subtraction for the Sn $3d^{5/2}$, S 2p, Cu 3p and Zn 3p core levels, and Table 3 the overview on the fitting results. The XPS results before and after the thermal treatment wanted to be confronted as well. One first consideration can be made on the absence of Zn signal. Such result might arise from two consequences: first, Zn has very high affinity with the ligands that completely passivate Zn-sites and so cover Zn from being detected, or second, Zn is actually absent from the NP surface, that is therefore characterized by CTS (Cu_3SnS_4) phase. This second cause is supposed to be the most probable, considering also the asymmetry on the Sn 3d peak. In the case of Sn 3d, the higher binding energy peak might be given by a compound where Sn is present with a 5+ oxidation state, like Cu_3SnS_4. In such compound, both Cu and S are present with the same oxidation state as CZTS, therefore their peaks do not shift dramatically from the CZTS reference positions. As Cu is represented by the presence of one species only, it is presumed that the entire NPs is constituted of CTS. The lower energy peak in the Sn 3d spectrum is instead considered arising from the 4+ oxidation state of Sn atoms bonding to sulfur-ligands. The fact that the relative abundance of the two different Sn species changes with the annealing, can confirm the hypothesis just exposed: the CTS phase increases in signal after thermal treatment due to evaporation of surface ligands. Another consideration that can be made on the XPS results is the very low signal of Sn and Cu compared to S. Most of S detected is considered to come from the S^{2-} ligands. The first peak at around 161.6 eV can be reconnected to the CTS phase. The second peak, at higher binding energies, might come from the ligands. The electrons carried by the S^{2-} ligands must be donated to a surface uncoordinated site to passivate it, leaving the 2p electrons less shielded by the outer orbitals. Also, the S^{2-} anions form a strong covalent bond with the surface sites [9]. The second peak is confirmed to belong to S^{2-} ligands also by the complete change of spectra of S 2p core level after the annealing step: ligands evaporate and more CTS phase is detected. It is reasonable that S is the most detected element also in the CTS phase, as the S^{2-} ligands do not coordinate with the S atoms on the surface of the NP, but with the positive charged metal sites [23]. It is not possible to say whether the surface ligands coordinate better with Cu or with Sn sites, as the percentage of these elements on the surface of the NP might differ from the bulk. A serious amount of S in sulfate state is present at the surface, and its relative abundance increases with annealing. One last examination wants to explain the reasons why in the Zn 3p spectrum the signal from the Sn 4p peak seems to decrease with the annealing step. Such result might arise from charging of the sample. The acquisition system adds up all the counts for all the scans performed on the same kinetic energy window. To obtain a better spectra, the number of scans after the annealing was increased of more than 10 scans. In case of charging of the sample, the number of detected electrons decreases with scans. However, when normalizing, the total count sum has been divided for the total number of scans. The result of normalization would justify the decrease in the normalized peak intensity in the after-annealing case.

Sample B - Sn_2S_6 $^{4-}$ ligands

The analysis of sample B (Sn_2S_6 $^{4-}$ ligands) was performed at NTNU, probing the material with a Mg-anode gun at energy 1253.6 eV. In contrast to sample A, which was annealed in the same position of the XPS experiment, sample B had to be moved to another chamber for the thermal treatment. It was not possible to probe the same exact area before and after the annealing step to evaluate any change in composition. Therefore, XPS results will be given only for the sample before undergoing annealing.
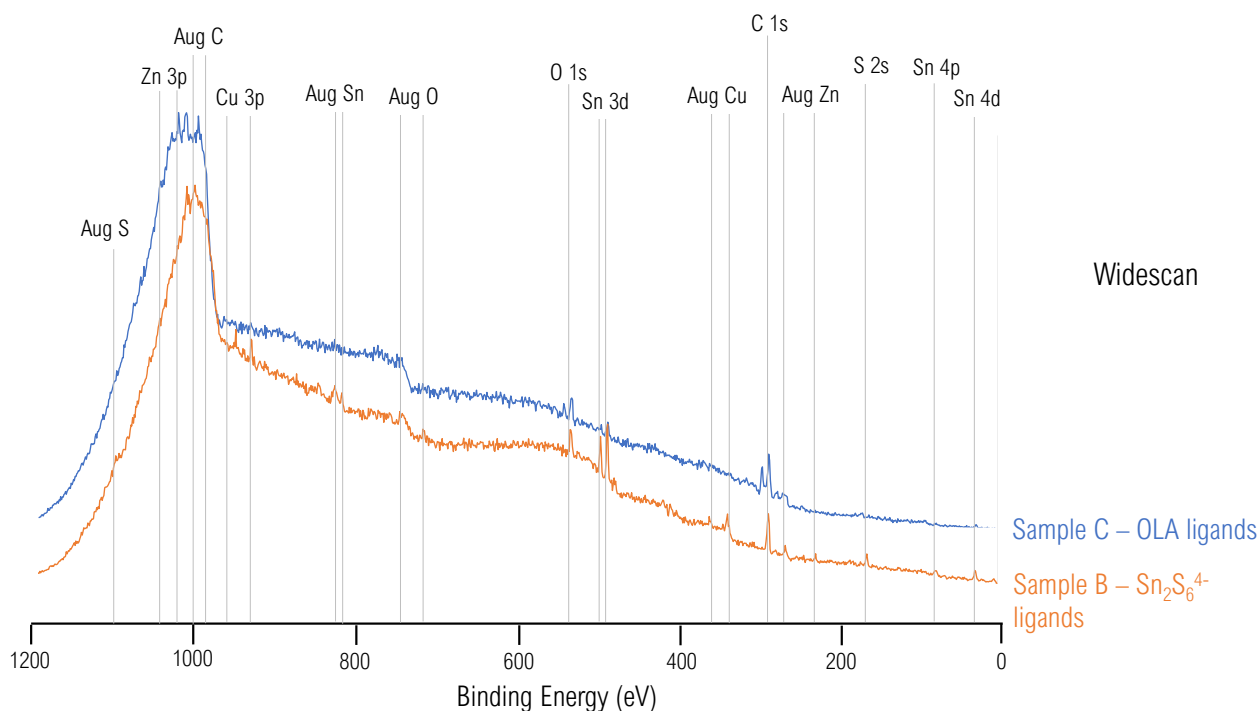

Figure 32: XPS widescan measured on the CZTS drop-casted sample B (Sn_2S_6 $^{4-}$ ligands) and sample C (OLA-capping), before the annealing treatment. The spectra have been shifted upwards for clarity. Important feature to show is the abruptly decreasing background at binding energies above 1000 eV, due to charging of the sample. The charging is considered to be an effect of the insulating behavior of the ligands.

The widescans before thermal treatment for sample B and C is shown in Figure 32. The main feature that wants to be discussed is the decreasing background after $E_B = 1000$ eV. This effect might result from poor alignment between the position of sample in the chamber and the electron lenses system, or by charging of the material. It is believe that the ligands might insulate the different NPs from each other, so that charges accumulate and generate an electrical field that blocks low kinetic energy electrons from leaving the sample. Such event might also determine alteration of the real data: the signal from Zn 2p is produced at low kinetic energies ($E_B \approx 1020$ eV), and might not be fully detected due to insulating behavior of the ligands. It

is also possible to see that Si signal is not detected, meaning a nice coverage of the substrate.

The narrow scans results are shown in Figure 33 and Table 4. Interesting outcomes include:
- the shift of all the peaks of around +1 eV with respect to sample A, symptom of charging of the sample;
- the visibility of Zn, probably due to the mean free path of the emitted electrons and shorter ligand molecules;
- the broader peaks with respect to the ones obtained with the synchrotron radiation;
- the lower percentage of S and Sn than expected.
Since NPs are covered in Sn_2S_6 $^{4-}$ ligands, it was assumed that higher values of relative abundance of Sn and S would be measured, and that both spectra would be described by the presence of different chemical bonds. However, Sn $3d^{5/2}$ can be described by CZTS species only, and S 2p spectrum shows CZTS and sulfate peaks. The detection of only CZTS phase in Sn and S confirms the ability of the Mg gun photons to probe deeper in the sample. Moreover, the ligand size can be assumed to be smaller than the mean free path. High presence of oxygen is detected as well, supposedly from the sulfate phase. Although the NPs have been confirmed previously to be Cu-poor Zn-rich, higher percentage of Cu results from XPS to be present at the surface, giving credit to the hypothesis that the outer surface is made of CTS phase and Zn is present in the bulk. No other secondary phase was detected, as for example SnS_2 grains.

Table 4: Overview of the fitting results of the detected phases for the drop-casted sample B (Sn_2S_6 $^{4-}$ ligands).The error on the peak energies resulted to be < 0.01 eV for all the peaks, and < 0.03 % on the relative abundance values.

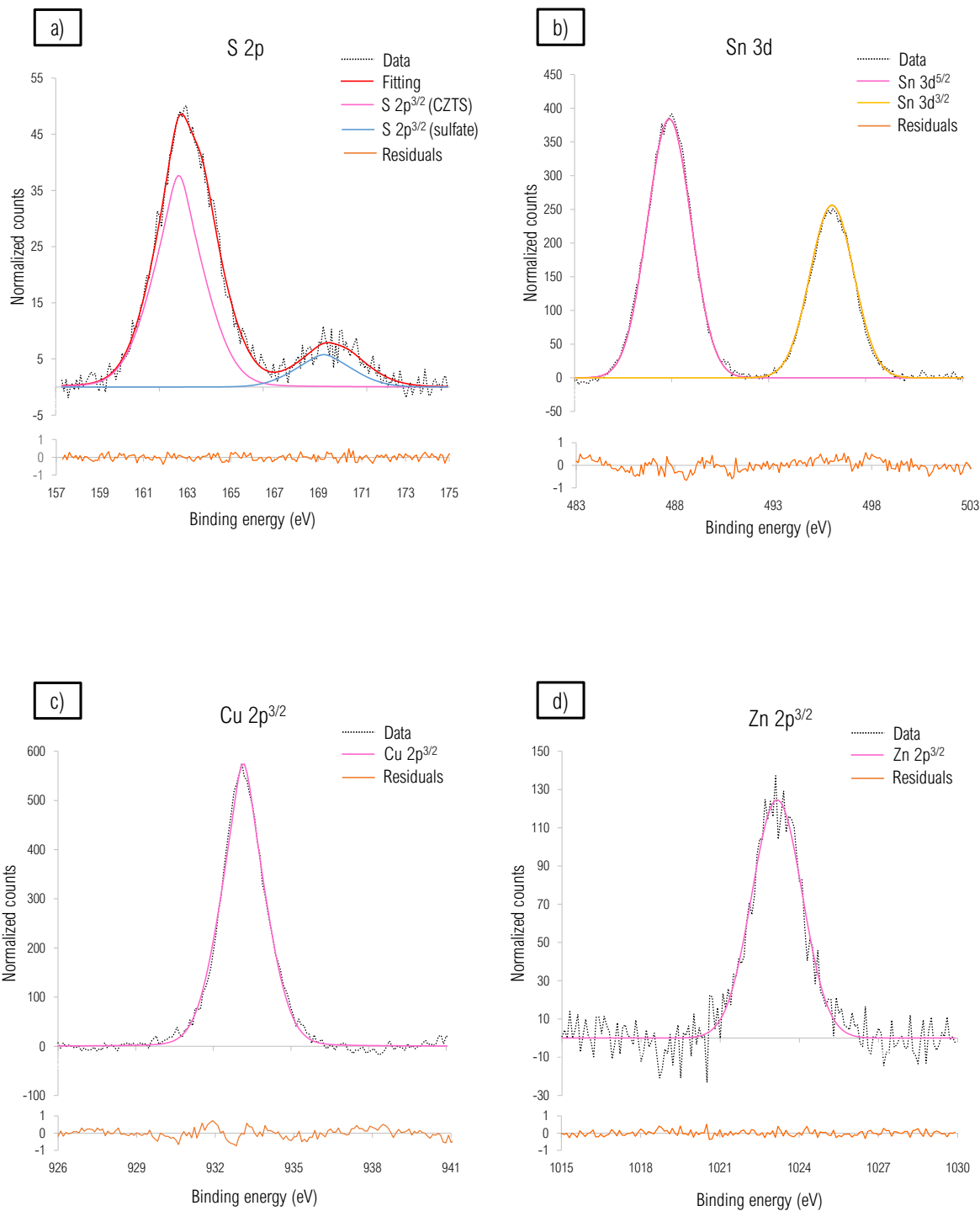| Element	Phase	Orbital	Energy (eV)	Relative abundance (%)
S	CZTS	$2p^{3/2}$	162.9	31.53
		$2p^{1/2}$	164.1	
	sulfate	$2p^{3/2}$	169.9	5.30
		$2p^{1/2}$	171.1	
Sn	CZTS	$3d^{5/2}$	487.9	23.43
		$3d^{3/2}$	496.3	
Cu	CZTS	$2p^{3/2}$	933.2	32.59
Zn	CZTS	$2p^{3/2}$	1023.0	7.15

Figure 33: Narrow XPS scans for the solution processed Sample B (Sn_2S_6 $^{4-}$ ligands), for the core levels a) S 2p, b) Sn 3d, e) Cu 2p$^{3/2}$ and d) Zn 2p$^{3/2}$. The raw data (black lines) are compared with the fitting model results. All the spectra seem to be described by the presence of one single phase (CZTS). S 2p spectra shows also the contribution of some sulfate presence.

Sample C - OLA ligands

As previously stated, the widescan of sample C (OLA-capping) shows charging behavior, as for high binding energies the count rate greatly decreases. By performing widescan on different areas of the surface, the sample resulted quite heterogeneous. An high signal for the O 1s and C 1s core level is detected. The significant signal of oxygen is justified by a likewise high signal of sulfate phase (see Figure 34, where the results for the high-resolution scans are displayed). Extremely high amounts of C are explained by the carbon content of the OLA molecules. In general, very low counts are observed for the CZTS elements compared to previous samples, due to the very high presence of C on the surface. Although Zn content is found to be less than 1/30 of the C content, it appears to be present in quite high percentages compared to the other metals, and at least in 2 phases, as shown by the asymmetry of its spectrum. As the NPs are believed to present mostly Cu at the surface, the lower binding energy peak in the Zn spectrum is hardly believed coming from CZTS. This peak might be explained by the existence of secondary phases of organometallic nature [50]. The higher binding energy peak might be originated from CZTS in case of high charging of the sample. However, such charging behavior is not seen in other peaks. CZTS signal might also be overlapping with the first peak, and therefore not resolved as singular phase. At this energy also compounds with Zn and S could be expected [50]. It is not clear which kind of Zn compounds are present on the sample and which their origin is. The S spectrum shows the usual sulfate and CZTS peaks, plus a secondary phase at energy around 164.6 eV, addressed to a possible organometallic compound. Values found in literature for Cu_xS report S 2p at lower binding energy (around 162.3 eV [50]), therefore this peak was not attributed to this possible secondary phase. Moreover, the fitting procedure for Cu 2p peak resulted quite challenging due to the low counts and the high noise. The relative abundance of the different species does not help in the visualization of which secondary phases Zn and S could be part of, or if they appear together in an impurity compound.
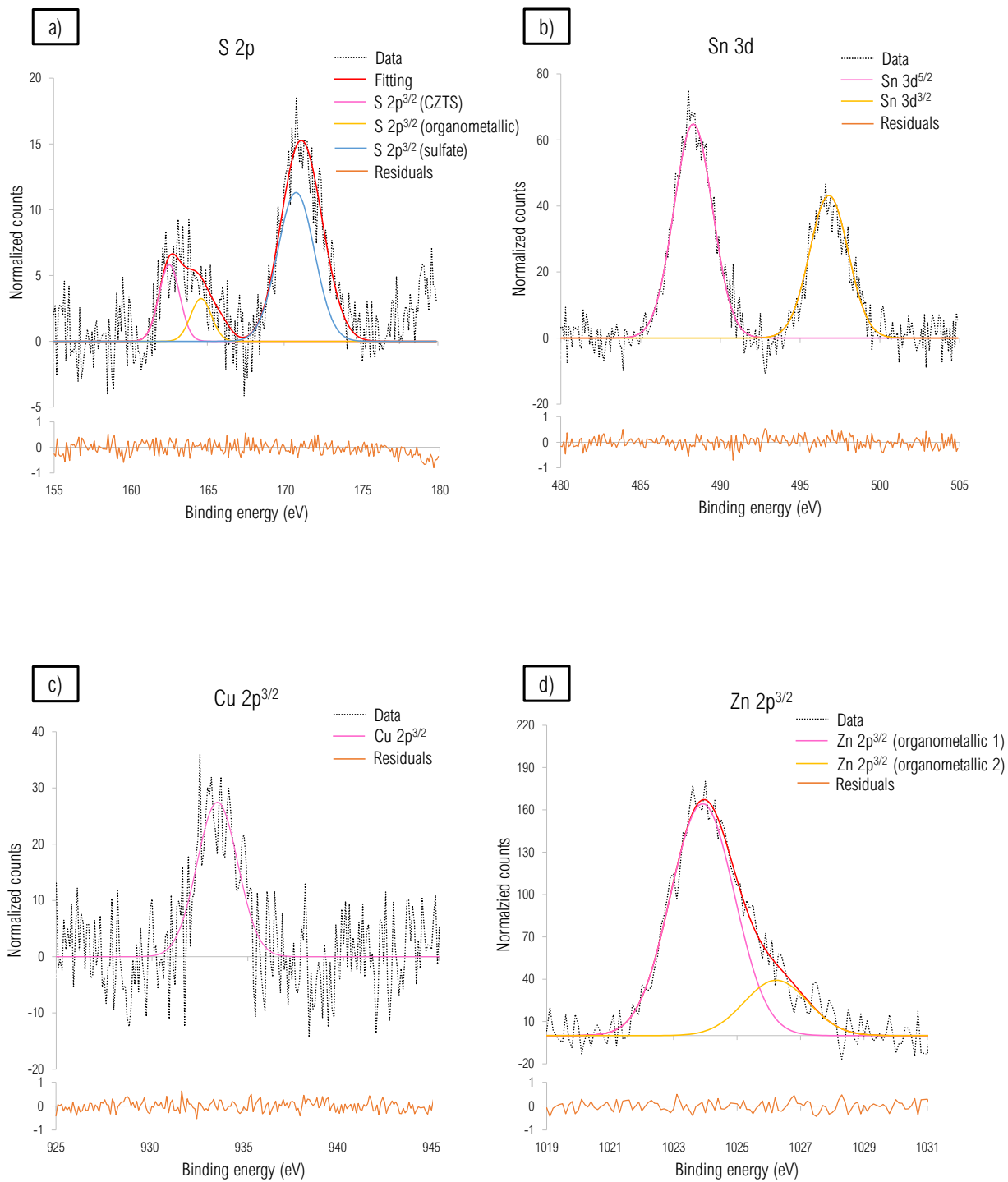
Figure 34: High resolution XPS scans for the solution processed Sample C (OLA ligands), for the core levels a) S 2p, b) Sn 3d, e) Cu $2p^{3/2}$ and d) Zn $2p^{3/2}$. The raw data (black lines) are compared with the fitting model results.

Table 5: Overview of the fitting results of the detected phases for the drop casted sample C (OLA ligands).The error on the peak energies resulted to be < 0.01 eV for all the peaks, and < 0.03 % on therelative abundance values.

Element	Phase	Orbital	Energy (eV)	Relative abundance (%)
S	CZTS	$2p^{3/2}$	162.5	8.38
		$2p^{1/2}$	163.7	
	organometallic	$2p^{3/2}$	164.6	4.67
		$2p^{1/2}$	165.8	
	sulfate	$2p^{3/2}$	170.8	28.88
		$2p^{1/2}$	172.0	
Sn	CZTS	$3d^{5/2}$	488.3	13.24
		$3d^{3/2}$	496.8	
Cu	CZTS	$2p^{3/2}$	933.4	6.18
Zn	organometallic 1	$2p^{3/2}$	1023.9	31.20
	organometallic 2	$2p^{3/2}$	1026.2	7.45

6.2.2 Band Gap

The band gaps of the NPs were determined from combined UPS and IPES spectra. However, for sample A (S^{2-} ligands) only a VB study was performed, due to the absence of an IPES system at the synchrotron beamline. For all the samples, the analysis were performed before and after thermal treatment in order to estimate the effect of ligand-induced dipoles over the energy states of the material.

Sample A - S^{2-} ligands

Figure 35 shows the VB for sample A before and after the thermal treatment, recorded at photon energy of 140 eV. The VB maximum was determined by the intersection of the linear fitting of the data and the x-axis (same procedure was applied to CB minimum in IPES data). The main noticeable feature in the spectra is the broad peak at around -3 eV. From RPES results, such peculiarity can be attributed to the transition from Cu 3p orbital. The peak moves from -3.1 to -3.4 eV after the thermal treatment. The same behavior is shown by the VB maximum, that shifts to more negative binding energies. This behavior can be explained by the loss of S^{2-} anions from the surface. The VB max shift has electrostatic origins, as the surface atom-to-ligand molecule generates and electric dipole, as previously explained in Chapter 3.4. S^{2-} anions around the NP surface are presumed to create a dipole pointing outwards, and by losing a fraction of ligands due to evaporation, the total VB moves at lower binding energies. The VB max E_V is seen to change from -1.808 ± 0.001 eV to -1.994 ± 0.001 eV after annealing (the E_V and E_C values for all the samples are reported in Table 6). Furthermore, the VB spectra show a slow rise from the Fermi level, instead of a sharp one starting at the VB maximum: this effect might be caused by the non-complete passivation of the surface, which introduces

allowed states in the band gap. It is also important to notice that the photon energy at which the VB was recorded is below the transition energy for the S 2p core level, supposed to be the one responsible for the VB maximum from RPES results.
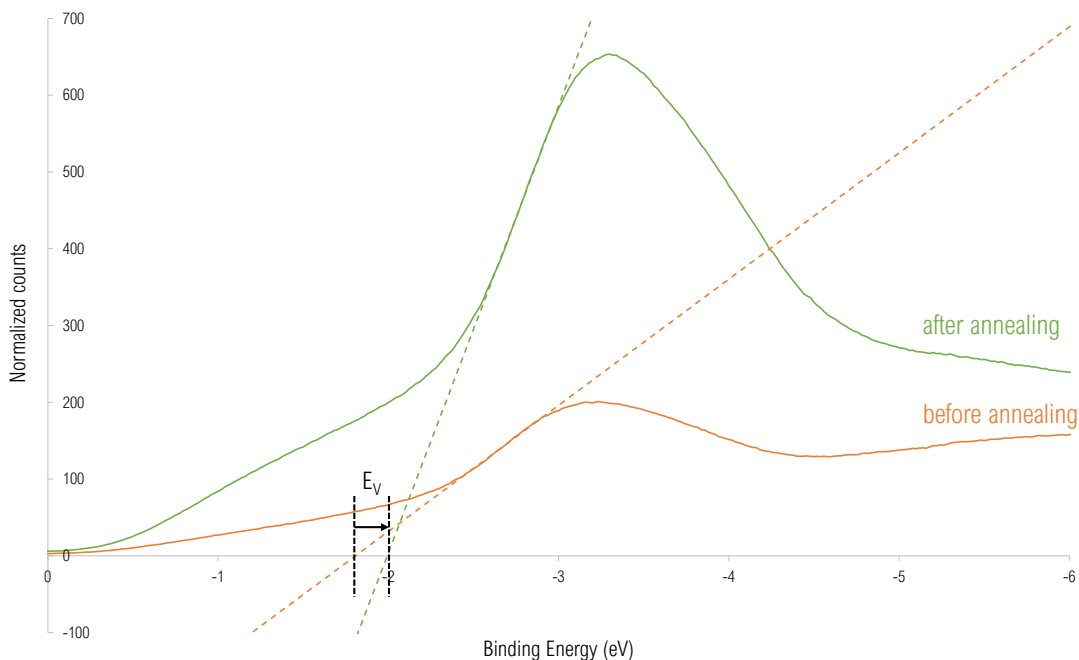

Figure 35: UPS spectra of the solution processed sample A (S^{2-} ligands), before and after annealing procedure, and linear fitting for the estimation of VB maximum E_V. The broad peaks at around 3 eV are attributed to transition from Cu 3p. The increase of counts could be explained by evaporation of S ligands from the surface, uncovering CTS underneath. Another effect of the evaporation of ligands is the shift of E_V to lower binding energy, due to the presence of less dipoles around the NPs surfaces: E_V moves from -1.808 $\pm$ 0.001 eV to -1.994 $\pm$ 0.001 eV after annealing.

Sample B - Sn_2S_6 $^{4-}$ ligands

UPS analysis for samples B (Sn_2S_6 $^{4-}$ ligands) and C (OLA-capping) was performed in the NTNU Surface Lab, together with IPES study. It is important to inform that both these analysis resulted quite difficult to perform due to the insulating behavior of the samples. UPS and IPES happened to be extremely challenging, as it was not possible to collect more than 1-3 scans at a time before the sample would charge. Therefore, the experiments occurred to be very time consuming, as the samples needed to be let discharge after every collection.

Figure 36 shows the CB and VB spectra for sample B before and and after the thermal treatment. Sn_2S_6 $^{4-}$ capping displays the same dipole behavior as the case of S^{2-} ligands: after annealing the band gap shifts entirely to lower binding energies. The absolute value of the energy gap, given by the difference between the CB minimum E_C and E_V (2.463 $\pm$ 0.002 eV

before annealing and 2.654 ± 0.002 eV after annealing), changes after the treatment. Such change is driven by E_V shifting of around -0.5 eV, combined with E_C shifting of -0.25 eV. It is interesting however to see a change in the value of the band gap, as the effect of the dipoles around the NP should shift all the energy states at the same time. It could be possible that, due to the presence of the ligands at the surface, UPS and IPES also give signal from empty states of the ligands, closer to the Fermi level, that "disappear" as ligands are evaporated. In general, the measured band gap is higher than the theoretical CZTS single crystal (around 1.5 eV) and higher than the measured band gap on the same NPs through UV-vis (1.73-1.83 eV): this outcomes can be justified by the structural defects of the NPs and the insulating effect of the ligands.
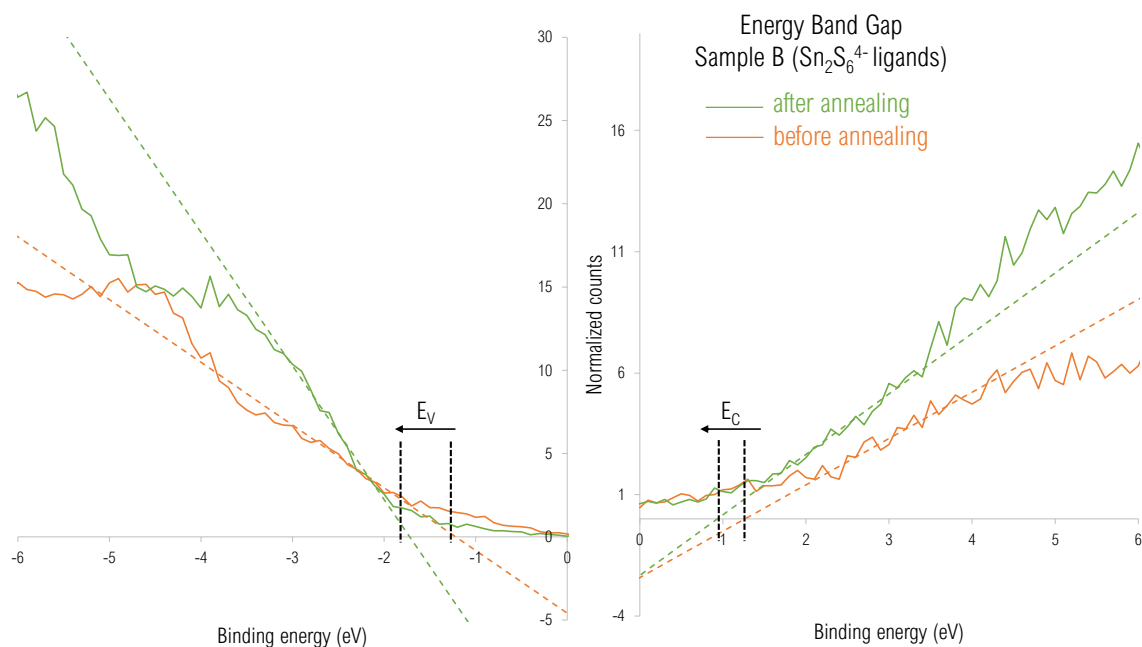

Figure 36: UPS and IPES spectra of the solution processed sample B (Sn_2S_6 $^{4-}$ ligands), before and after annealing procedure, and linear fitting for the estimation of VB maximum E_V and CB minimum E_C. The effect of ligand evaporation results in a shift of band edges to lower binding energies.

Sample C - OLA ligands

Figure 37 shows the CB and VB spectra for sample C before and and after the thermal treatment. OLA capping seems to show the opposite dipole behavior with respect to the case of S^{2-} ligands: after annealing the band gap shifts entirely to higher binding energies. However, this behavior might not be addressed to the dipole effect, as much as to the presence of insulating C-chains that thanks to thermal annealing are partially removed and let some signal to come from the actual NPs. This hypothesis can be confirmed by the absence in the UPS spectra of any common feature related to Cu 3p transition. For this same reason, E_V is at very low

binding energy and the sample behaves like an insulator. As annealing is performed, more states between -2 and -5 eV are detected, showing partial removal of the ligands. E_C does not seem to change significantly.
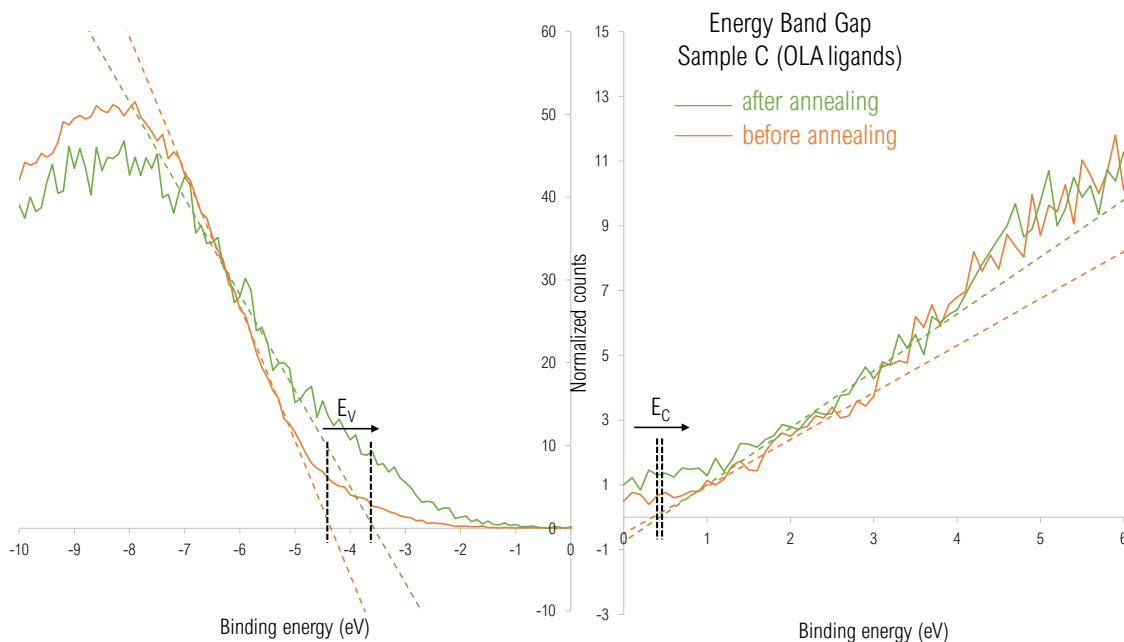

Figure 37: UPS and IPES spectra of the solution processed sample B (OLA ligands), before and after annealing procedure, and linear fitting for the estimation of VB maximum E_V and CB minimum E_C. The effect of ligand evaporation results in a shift of band edges to higher binding energies.

Table 6: Overview of the measured VB maximum E_V, CB minimum E_C and bandgap for the three solution processed samples, before and after the annealing step. E_V and E_C are given with an error $\pm$ 0.001 eV.

Sample	Annealing	E_V (eV)	E_C (eV)	Band gap (eV)
A (S^{2-})	before	- 1.808	-	-
	after	-1.994	-	-
B ($Sn_2S_6^{\ 4-}$)	before	-1.197	1.266	2.463
	after	-1.721	0.933	2.654
C (OLA)	before	-4.348	0.346	4.694
	after	-3.569	0.430	3.999

7   Conclusion

The aim of the presented work concerned the study of the feasibility of PES techniques in the analysis of the composition, chemical environments and energy band gap of solution-processed NPs CZTS thin films. The samples were prepared by drop-casting on Si-doped substrates. The same synthetized NPs were stabilized in different solutions by various ligands. Three samples were compared (S^{2-}, Sn_2S_6 $^{4-}$, and OLA ligands) through the results of XPS, UPS and IPES analysis. An high-crystallinity sample of CZTS was also provided. Its composition and VB were investigated at the MATline beamline. RPES was performed in order to provide a benchmark for the understanding of the VB features in the drop-casted samples.

RPES study helped in the understanding of the different contributions at the edge of the VB. The states at the VB edge seem to be related to the transitions from Cu 3p and S 2p orbitals. For photon energies between 40 and 162 eV, the VB maximum shifted from around 2.5 to 1.2 eV from the Fermi level. For energies greater than 162 eV (S 2p transition), the VB maximum seemed to keep a constant value at around 1.2 eV. The elemental composition of the crystalline sample revealed high presence of S at the surface, existing also in sulfate and sulfoxide phases. The ratios Cu/(Zn+Sn) and Zn/Sn appeared much lower (0.49 ± 0.01 and 0.14 ± 0.01) than the experimental optimal for bulk CZTS (0.8 and 1.25), due to the high presence of Sn compared to Cu and Zn at the surface. The sample was however sputtered, and subsequently annealed, to remove surface contaminants: the procedure might have altered the surface conformation, letting different atomic layers to be visible, and might also have been responsible for the formation of sulfoxide and sulfate phases. Nevertheless, longer sputtering times (> 10 min at 500 eV with Ar) are suggested for this type of sample, for a more efficient impurity removal. The peak positions for the kesterite phase in the crystalline sample were also used as reference for the thin film XPS results.

Chemical composition analysis on the thin film with S^{2-} ligands allowed to understand that the NPs are probably characterized by CTS phase at the surface, and Zn diffusing into the bulk. This result is confirmed by the absence of signal from Zn, the presence of two chemical shifts in the Sn peak (attributed to the two oxidation states, IV for Sn atoms bonding to ligand molecules, and V for Sn in CTS phase), the description of Cu 3p by one phase only, the asymmetric shape of the S spectrum and its change after annealing: the S 2p peak shows the clear presence of two phases, one addressed to ligands, as after annealing is abruptly decreased, and one to CTS phase. The element composition of sample B and C gave also further details on the length scale of the ligands: for sample B, the Sn_2S_6 $^{4-}$ ligands are considered short enough so that the detected signal originates from beneath the CTS surface (as Zn is also detected), and the only identified impurity is addressed to sulfate compounds, while OLA-ligands (sample C) produce an extremely high C signal covering completely the NPs surface from which the detected signal is much lower. Due to the low counts and high signal-to-noise ratio in the case

of OLA ligands, it was not possible to determine whether there was presence of the secondary phase Cu_xS on the surface. However, Zn seemed to appear abundantly in organometallic compounds.

UPS and IPES investigations resulted challenging due to sample charging. This effect was attributed to the insulating behavior of the ligands, confirmed also by the shift in peak energy in XPS spectra. Having a conductive substrate seemed not enough to avoid accumulation of charge. Nevertheless, using glass or insulating substrates is highly discouraged for this type of technique. UPS results seemed also be affected by the size of the ligands: in the case of short molecules, the same VB peak attributed to Cu 3p transition was visible, while for longer carbon chains the VB maximum was found at very low binding energies, suggesting that the detected signal was caused by the ligand molecules and not by the NPs. Thermal treatment was also performed on the films to understand the dipole behavior at the ligand-surface interface. For S^{2-} and $Sn_2S_6{}^{4-}$ ligands, the dipole is supposed to be pointing outwards: the effect should be a shift of all the energy states of the NP towards higher binding energies. By letting evaporate a fraction of the ligands, the VB maximum shifts and its direction can be addressed to the loss of dipoles at the surface. For the case of OLA-capping, however, such dipole-induced behavior cannot be confirmed, as the spectra are thought of being representative of the energy states of the ligand molecules and not of the NPs. In all cases, the measured band gaps (around 2.5 eV for $Sn_2S_6{}^{4-}$ ligands, and > 4 eV for OLA-capped NPs) resulted higher than the previously estimated values through UV-vis (1.73-1.83 eV), confirming the insulating effect of the ligands at the surface of the NPs.

PES techniques showed interesting applications in the study of CZTS ligand-capped NPs. Due to high surface sensitivity, the interface between ligand and NP was studied in its chemical environment and electronic properties. Moreover, as the ligand molecule size can be in the same order as the electron mean free path, one can probe the capping agent, the NPs deeper under the surface or the real interface. For future work, a more comprehensive study on CZTS NPs thin films could combine the interface results of PES techniques with complementary information from other methods, to exploit the structure of the ligands as well as the geometry of the NPs and the arrangement patterns of the capping layer on the surface. Moreover, PES techniques resulted effective in providing information about the effect of ligands on the NPs band gap, and such knowledge and methods could be used in the tailoring of CZTS NPs band gap by trying other commonly used stabilizers.

References

[1] A. Luque, S. Hegedus *Handbook of Photovoltaic Science and Engineering*, John Wiley & Sons, (2011)

[2] W. Shockley, H.J. Queisser *Detailed Balance Limit of Efficiency of p-n Junction Solar Cells*, Journal of Applied Physics, (1961), pp. 510-519

[3] A. Polman, M. Knight, E.C. Garnett, B. Ehrler, and W.C. Sinke *Photovoltaic materials: present efficiencies and future challenges*, Science, (15 April 2016)

[4] A. Crovetto *Cu_2ZnSnS_4 solar cells: physics and technology by alternative tracks*, PhD Thesis, Technical University of Denmark, (31 August 2016)

[5] H. Zhou et al. *CZTS nanocrystals: a promising approach for next generation thin film photovoltaics*, Energy and Environmental Science, (25 July 2013)

[6] X. Liu et al. *The current status and future prospects of kesterite solar cells: a brief review*, Progress in Photovoltaics: Research and Applications, (28 January 2016)

[7] C. Platzer-Björkman et al. *Reduced interface recombination in Cu_2ZnSnS_4 solar cells with atomic layer deposition $Zn_{1-x}Sn_xO_y$ buffer layers*, Applied Physics Letters, (14 December 2015)

[8] L. Korala et al. *Ligand-Exchanged CZTS Nanocrystal Thin Films: Does Nanocrystal Surface Passivation Effectively Improve Photovoltaic Performance?*, Chemistry of Materials, Vol. 29, pp. 6621-6629 (27 June 2017)

[9] M. A. Boles, D. Ling, T. Hyeon, D. W. Talapin *The surface science of nanocrystals*, Nature Materials, (22 January 2016)

[10] S. Schorr *The crystal structure of kesterite type compounds: a neutron and X-ray diffraction study*, Solar Energy Materials & Solar Cells, (15 February 2011)

[11] S.R. Hall, J.T. Szymański, J.M. Stewart *Kesterite, $Cu_2(Zn,Fe)SnS_4$, and stannite, $Cu_2(Fe,Zn)SnS_4$, structurally similar but different minerals*, Canadian Mineralogist, Vol. 16, pp. 131-137 (1978)

[12] S. Chen, A. Walsh, X. Gong, S. Wei *Classification of Lattice Defects in the Kesterite Earth-Abundant Solar Cells Absorber*, Advanced Materials, Vol. 25, pp. 1522-1539 (2013)

[13] C. Persson, R. Chen, H. Zhao, M. Kumar, D. Huang *Electronic Structure and Optical Properties from First-Principles Modeling*, In. *Copper Zinc Tin Sulfide-Based Thin-Film Solar Cells*, John Wiley & Sons, (2015)

[14] W. Li et al. *Recent Progress in Solution-Processed Copper-Chalcogenide Thin Film Solar Cells*, Energy Technology, Vol. 6, pp. 46-59 (2018)

[15] H. Katagiri et al. *Development of CZTS-based thin film solar cells*, Thin Solid Films, (8 November 2008)

[16] M. T. Winkler et al. *Optical designs that improve the efficiency of $Cu_2ZnSn(S,Se)_4$ solar cells*, Enegy & Environmental Science, Vol. 7, pp. 1029-1036 (2014)

[17] A. Polizzotti, I. L. Repins, R. Nou, S-H. Wei, D. B. Mitzi *The state and future prospects of kesterite photovoltaics*, Energy & Environmental Science, (22 August 2013)

[18] K. Ramasamy, M. A. Malik, P. O'Brien *Routes to copper zinc tin sulde Cu_2ZnSnS_4 a potential material for solar cells*, Chemical Communications, (30 March 2012)

[19] Y.Yin, A. P. Alivisatos *Colloidal nanocrystal synthesis and the organic-inorganic interface*, Nature, (29 September 2005)

[20] N. Mirbagheri et al. *Synthesis of ligand-free CZTS nanoparticles via a facile hot injection route*, Nanotechnology, (23 March 2016)

[21] J. Owen *The coordination chemistry of nanocrystal surfaces*, Science, (6 February 2015)

[22] M.V. Kovalenko, M. Scheele, D.V. Talapin *Colloidal Nanocrystals with Molecular Metal Chalcogenide Surface Ligands*, Science, (12 June 2009)

[23] A. Nag et al. *Metal-free Inorganic Ligands for Colloidal Nanocrystals: S^{2-}, HS^-, Se^{2-}, HSe^-, Te^{2-}, HTe^-, TeS_3^{2-}, OH^-, and NH_2^- as Surface Ligands*, Journal of the American Chemical Society, (17 June 2011)

[24] A.H. Ip et al. *Hybrid passivated colloidal quantum dot solids*, Nature Nanotechnology, (29 July 2012)

[25] P.R. Brown et al. *Energy Level Modification in Lead Sulfide Quantum Dot Thin Films through Ligand Exchange*, ACS Nano, (13 May 2014)

[26] D.J. Milliron *The surface plays a core role*, Nature Materials, Vol. 13, p. 772-773 (2014)

[27] M.T. Frederick et al. *Surface-Amplified Ligand Disorder in CdSe Quantum Dots Determined by Electron and Coherent Vibrational Spectroscopies*, Journal of the American Chemical Society, (12 April 2011)

[28] A.J. Morris-Cohen *Chemical, Structural, and Quantitative Analysis of the Ligand Shells of Colloidal Quantum Dots*, Chemistry of Materials, (30 August 2012)

[29] J. Kumar *Photoelectron Spectroscopy: Fundamental Principles and Applications*, In. *Handbook of Materials Characterization*, Springer Nature, (2018)

[30] S. Suga, A. Sekiyama *Photoelectron Spectroscopy: Bulk and Surface Electronic Structures*, Springer Series in Optical Sciences, Vol. 176, pp. 1-396 (2014)

[31] S. Hüfner *Photoelectron Spectroscopy: Principles And Applications*, Springer Verlag, (2003)

[32] A. Jablonski, C. J. Powell *Information depth and the mean escape depth in Auger electron spectroscopy and X-ray photoelectron spectroscopy*, Journal of Vacuum Science & Technology A, Vol. 1, pp. 274-283 (2003)

[33] A. Zangwill *"Clean Surfaces"*. In *Physics at Surfaces*, Cambridge University Press, pp. 5-6 (1998)

[34] P. D. Johnson *Chapter 13 - Inverse Photoemission*, Studies in Surface Science and Catalysis, Vol. 74, pp. 509-552 (1992)

[35] F. Mazzola, M. Nematollahi, Z.S. Li, S. Cooil, X. Yang, T.W. Reenaas, J.W. Wells *Resonant photoemission spectroscopy for intermediate band materials*, Applied Physics Letters, (11 November 2015)

[36] J. Als-Nielsen, D. McMorrow *Elements of Modern X-ray Physics, Second Edition*, John Wiley & Sons, (18 March 2011)

[37] A. Madsen, H. Sinn *Europe enters the extreme X-ray era*, CernCourier, (10 July 2017)

[38] P. Willmott *An introduction to synchrotron radiation: Techniques and applications*, John Wiley & Sons, (13 June 2011), pp. 39-86

[39] C. Rein, S. Engberg, J.W. Andreasen *Stable, carbon-free inks of Cu_2ZnSnS_4 nanoparticles synthesized at room temperature designed fro roll-to-roll fabrication of solar cell absorber layers*, Journal of Alloys and Compounds, (7 February 2019)

[40] D. Hoffman, B. Singh, J. H. Thomas *Handbook of Vacuum Science and Technology*, Academic Press, (1998)

[41] M. Jorge *User Guide - NyNalos*

[42] PSP Vacuum Technology *IPES Electron System: Instruction Manual*

[43] V. Jain, M. C. Biesinger, M. R. Linford *The Gaussian-Lorentzian Sum, Product, and Convolution (Voigt) functions in the context of peak fitting X-ray photoelectron spectroscopy (XPS) narrow scans*, Applied Surface Science, (29 March 2018)

[44] R. Hesse, P. Streubel, R. Szargan *Product or sum: comparative tests of Voigt, and product or sum of Gaussian and Lorentzian functions in the fitting of synthetic Voigt-based X-ray photoelectron spectra*, Surface and Interface analysis, (9 January 2007)

[45] J. Vegh *On analyzing the intrinsic processes through the Shirley background correction procedure*, Surface Science, (25 January 2005)

[46] J. Vegh *The Shirley background revised*, Journal of Electron Spectroscopy, (18 January 2006)

[47] J. Vegh *The Analytical Form of the Shirley-type Background*, Journal of Electron Spectroscopy and Related Phenomena, (27 May 1988)

[48] WebCrossSections - ELETTRA *Atomic Calculation of Photoionization Cross-Sections and Asymmetry Parameters*
url: https://vuo.elettra.eu/services/elements/WebElements.html

[49] J. F. Moulder, W. F. Stickle, P. E. Sobol, K. D. Bomben *Handbook of X-ray Photoelectron Spectroscopy*, Perkin-Elmer Corporation, (1992)

[50] National Institute of Standards and Technology *NIST X-ray Photoelectron Spectroscopy Database*
url: https://srdata.nist.gov/xps/Default.aspx

[51] ISA, Centre for Storage Ring Facilities, Aarhus *ASTRID2 – The Ultimate Synchrotron Radiation Source*
url: http://www.isa.au.dk/facilities/astrid2/astrid2.asp

[52] ISA, Centre for Storage Ring Facilities, Aarhus *AU-MATLINE on ASTRID2*
url: http://www.isa.au.dk/facilities/astrid2/beamlines/AU-matline.asp

[53] L. Qiu, K. Zou, G. Xu *Investigation on the sulfur state and phase transformation of spent and regenerated S-zorb sorbents using XPS and XRD*, Applied Surface Science, (20 December 2012)

[54] D. Tang, K. Sun, F. Liu, Y. Lai *An alternative route towards low-cost Cu_2ZnSnS_4 thin film solar cells*, Surface & Coatings Technology, (30 April 2013)

[55] R. Bruhn, B. Sonntag, H.W. Wolff *3p excitations of atomic and metallic Fe, Co, Ni and Cu*, Journal of Physics B - Atomic, Molecular and Optical Physics, (20 June 1978)